5G Scenarios and Evolutions in the New Millimeter-Wave Bands

Hamidou Dembele

THESE DE DOCTORAT DE

L'ÉCOLE NATIONALE SUPERIEURE MINES-TELECOM ATLANTIQUE BRETAGNE PAYS DE LA LOIRE - IMT ATLANTIQUE

ECOLE DOCTORALE N° 601
Mathématiques et Sciences et Technologies de l'Information et de la Communication
Spécialité : *Télécommunications*

Par

Hamidou DEMBELE

5G Scenarios and Evolutions in the New Millimeter-Wave Bands

Thèse présentée et soutenue à IMT-Atlantique, Campus de Rennes, le 03 décembre 2021
Unité de recherche : Département MO, Lab-STICC/DIM
Thèse N° : 2021IMTA0273

Rapporteurs avant soutenance :

Marion BERBINEAU, Directrice de Recherche, Université Gustave Eiffel
Didier LE RUYET, Professeur, CNAM

Composition du Jury :

Président : Frédéric GUILLOUD, Professeur, IMT-Atlantique

Examinateurs : Rodolphe VAUZELLE, Professeur, Université de Poitiers
Marion BERBINEAU, Directrice de Recherche, Université Gustave Eiffel
Didier LE RUYET, Professeur, CNAM
Marie LE BOT, Ingénieure, Orange, Encadrante

Dir. de thèse : François GALLEE, Maitre de Conférences, IMT-Atlantique

Invité :
Patrice PAJUSCO, Directeur de département, IMT-Atlantique, Encadrant

Acknowledgement

I would like to express my sincere gratitude to all the people without their guidance, their help and their humanity, this PhD thesis would not have been possible.

First of all, I would sincerely like to thank my Orange supervisor Marie Le Bot, without whom this dissertation would not have been successful. The topic she proposed was precisely prepared with interesting objectives for my career. Then, she proposed several ways to understand and highlight it. I am deeply grateful for the maximum of her time spent with me by answering my many endless questions and discussing about the mathematical demonstrations and the accuracy of certain results with a calm, kind and nice attitude. It was very enjoyable to work with someone like her, caring, lovable, exceptional and full of ideas in the field of digital communications. I really wish her all the best for the future. Thank you Marie for everything!!!

I would particularly like to thank François Gallée, my thesis Director at IMT-Atlantique, from whom I learned a lot about antennas and propagation. Thank you for your advice, your vision and your ideas, especially for the end of the thesis. You are a wonderful and pleasant person, and it was a real pleasure for me to meet you. Thank you!!!

I would also thank Patrice Pajusco, my academic supervisor, for his advice, his comments and his reactions in order to make me even better. It was a real pleasure to share with me your knowledge about the wireless propagation channel. I really appreciated it!!!

A sincere acknowledgement to the committee members—the referees Marion Berbineau, Research Director at Université Gustave Eiffel and Didier Le Ruyet, Professor at CNAM, for their acceptance to review this work in detail. In the same way, my thanks are for Rodolphe Vauzelle, Professor at University of Poitiers and Frédéric Guilloud, Professor at IMT-Atlantique, for their participation in the defence committee.

My most deep thanks are also for my colleague Rediet (*Samba* or *Sambiiish*, Hahahaha) for his intensive help in C/C++ and his fantastic ideas during this thesis. Your *Yuri* says thank you very much for your good humour and your jokes. You are a nice and lovable person. I wish you the best for all that life has in store for you. I would also like to thank Bruno, my friend from the virtual pool with whom I had a great time with discussions around LDPC and digital communications in general, sometimes despite our weekends. Too bad I didn't make you eat raw cocoa. Thank you to Corentin (*Full Professor*), my doctoral colleague with whom I spent three wonderful years in pain and laughter with discussions concerning our various research works. All this allowed me to grow sincerely and to have recoil in the face of my MBA approach. I would also like to quote Philippe, the former manager of the team and my football team mate, who has always motivated

and reassured me in private when I had doubts. Thank you Philippe!!! A thank to our new team manager Rodolphe for his teasing. Thank you also to Kaoutar who really helped me in my beginnings for all that is administrative process in the management of the thesis, particularly my first year.

To my closest and best friend César, thank you for your daily support, your kindness and your sympathy. You are one of the best people in my life. You were always there when I needed you, especially during difficult times despite the distance. Thank you my brother. I also thank my other friend Moumouni (*Docteur*) for his prayers, help and advice. To my latest friends, Lassina (*Chairman*), Siriki (*Méitos-Le Vieux*), thank you for your support.

I am really grateful to all my family for their support, particularly, my loving father and role model *Sidiki Dembélé*. So true that you passed away since the start of my engineering circuit, but I wanted to show my gratitude for everything you have done for me. You are an extraordinary and very intelligent person. Today, all of this is the result of many years of upbringing and of life sure values such as a job well done, rigour, love and respect for others which you kept instilling in me. I am eternally grateful to you. Thank you Dad!!! I am also thankful to my adorable mother *Mummy Traoré*. Thank you so much for your daily prayers and blessings. I love you so much!!!

I also thank my Aunt Fatou and his husband Ibrahim (*Bravo*) for everything they did for me since my first days at IMT-Atlantique. To my cousins, i.e Habib (*La dormangne*, Hahahaha), Mohamed and Demba (*Expired Maraka*), Little Demba (*Superman*) and Bintou (*Mrs De La Roche*).

Finally, of course, a deep gratitude to Kady (*Himiab*) for her continued moral support and her concern for my daily life. You are one of the most wonderful things that I have encountered in my life. This thesis is also the result of the sacrifice and so much effort that you have made. Thank you very much for your listening and your attention, especially in the very complicated moments of the thesis. Your understanding and love had always dominated. You are one of the few people who showed me every time, I can cope better face a difficulty. I love you so much!!!

Contents

List of Figures

List of Tables

Acronyms

2D	Two-Dimensional
3D	Three-Dimensional
3GPP	3rd Generation Partnership Project
4G	4th Generation
5G	5th Generation
16QAM	Quadrature amplitude modulation with 16 symbols
64QAM	Quadrature amplitude modulation with 64 symbols
256QAM	Quadrature amplitude modulation with 256 symbols
ACK	Acknowledgement
ADC	Analog to Digital Converter
AF	Array Factor
AoA	Azimuth Angle of Arrival
AoD	Azimuth Angle of Departure
AP	Access Point
AR	Augmented Reality
AWGN	Additive White Gaussian Noise
BER	Bit Error Rate
BLER	Block Error Rate
BP	Belief Propagation
BS	Base Station
CDL	Clustered Delay Line
CIR	Channel Impulse Response
COST	Cooperation in Science and Technology
CP	Cyclic Prefix

CRC	Cyclic Redundancy Check
CSI	Channel Sate Information
D2D	Device-to-Device
DFT	Discrete Fourier Transform
DKED	Double Knife-Edge Diffraction
DL-SCH	Downlink Shared Channel
EG	Equal Gain
EIRP	Effective Isotropic Radiated Power
eMBB	enhanced Mobile BroadBand
FDD	Frequency Division Multiplex
FFT	Fast Fourier Transform
FSPL	Free Space Propagation Loss
Galacsy	Graphical application for system simulation
GCS	Global Coordinate System
GI	Guard Interval
GSCM	Geometry-based Stochastic Channel Model
GSM	Global System for Mobile communication
GTD	Geometrical Theory of Diffraction
HARQ	Hybrid Automatic Repeat reQuest
Hetnet	Heterogeneous Network
HPBW	Half-Power Beamwidth
I2O	Indoor-to-Outdoor
IDFT	Inverse Discrete Fourier Transform
IEEE	Institute of Electrical and Electronics Engineers
IFFT	Inverse Fast Fourier Transform
InH	Indoor Office
IoT	Internet of Things
ITU-R	International Telecommunication Union-Radiocommunication sector
KED	Knife-Edge Diffraction
LCS	Local Coordinate System

LDPC	Low Density Parity Check Coding
LLR	Log-Likelihood Ratio
LOS	Line of Sight
LTE	Long Term Evolution
LTE-A	Long Term Evolution-Advanced
M2M	Machine-to-Machine
MAP	Maximum A Posteriori
MBA	Multibeam Antenna
METIS	Mobile and wireless communications Enablers for the Twenty-twenty Information Society
MCS	Modulation and Coding Scheme
MIMO	Multiple-Input Multiple-Output
MiWEBA	Millimeter–Wave Evolution for Backhaul and Access
ML	Maximum Likelihood
mMIMO	Massive MIMO
mmMAGIC	mmWave based Mobile Radio Access Network for 5G Integrated Communications
MMSE	Minimum Mean Square Error
mMTC	Massive Machine Type Communications
mmWave	Millimeter-Wave
MPC	Multipath Component
MS	Min-Sum
MU-MIMO	Multi-User MIMO
NACK	Negative Acknowledgement
NLOS	Non-Line of Sight
NMS	Normalized Min-Sum
NR	New Radio
NSB	Non-Self-Blocking
O2I	Outdoor-to-Indoor
OFDM	Orthogonal Frequency-Division Multiplexing
PCM	Parity Channel Matrix

PDCCH	Physical Downlink Control Channel
pdf	probability density function
PDP	Power Delay Profile
PDSCH	Physical Downlink Shared Channel
PB-LDPC	Protograph-Based LDPC
PHY	Physical
PSS	Phase-Shifting Surface
QPSK	Quadrature Phase Shift Keying
RA	Reflectarray
RF	Radio Frequency
RMa	Rural Macro-cell
RMS	Root Mean Square
Rx	Receiver
SB	Self-Blocking
SBA	Single Beam Antenna
SCM	Spatial Channel Model
SCM-E	Spatial Channel Model-Extended
SF	Shadowing Fading
SINR	Signal-to-Interference-plus-Noise-Ratio
SISO	Single-Input Single-Output
SLL	Sidelobe Level
SMa	Suburban Macro-cell
SNR	Signal-to-Noise Ratio
SP	Sum-Product
SU-MIMO	Single-User MIMO
SV	Saleh-Valenzuela
SVD	Single Value Decomposition
TDD	Time Division Multiplex
TA	Transmitarray
Tx	Transmitter

UE	User Equipment
UHD	Ultra-High Definition
UL-SCH	Uplink Shared Channel
ULA	Uniform Linear Array
UMa	Urban Macro-cell
UMi	Urban Micro-cell
uRLLC	ultra-Reliable Low Latency Communications
UTD	Uniform Theory of Diffraction
V2V	Vehicle-to-Vehicle
VR	Virtual Reality
vs	Versus
WINNER	Wireless World Initiative New Radio
WLAN	Wireless Local Area Network
ZF	Zero Forcing
ZoA	Zenith Angle of Arrival
ZoD	Zenith Angle of Departure

Introduction

General Context

Mobile communication systems have been one of the most successful technology innovations in our modern existence. This can be justified by the combination of technological advances and attractive proposals which make cellular communication an indispensable part of our life. From analog to long-term evolution (LTE), each generation of mobile cellular technology has been inspired by the need to achieve new challenges. This is how the 5th generation (5G) was generally proposed to meet the strong demands for network accessibility, data rates and improved safety and health.

Referring to the aspect of increasing data rates, one of the major innovations envisaged, is the use of millimeter waves (mmWave) bands which are mainly characterized by the frequency spectrum above 6 GHz. Although the propagation loss is significant in mmWave frequency bands, huge amount of bandwidths are available in these regions of frequencies. Therefore, their use becomes indispensable for 5G use cases.

In this context, several investigations have been carried out by researchers in the wireless community concerning future mobile communications systems in these high frequency bands. To this purpose, according to measurements conducted at 28 and 38 GHz in the cities of New York and Austin, Rappaport *et al.* [1] showed that mmWave mobile communications for 5G can be effective if steerable directional antennas are used at base stations and mobile devices. Likewise, the studies carried out by Ghosh [2] at Nokia in the 73 GHz frequency band show that the use of a large array of antennas makes it possible to overcome the signal attenuations at mmWave frequencies. The European WORTECS (Wireless Optical/Radio TErabit Communications) project, which was focused on the objective of ultra-high speeds for a wireless virtual reality application, aimed at offering communication demonstrators in the 60 and 240 GHz frequency bands [3]. Simulation results showed that 8 Gbps of data rates using a 2 GHz channel bandwidth are achieved in a real wireless channel and with real wireless transceivers.

These first indications are invaluable for understanding and evaluating the potential of mmWave frequency bands. However, there are still many questions about the deployment of mmWave systems. In fact, due to the fact that mmWave frequencies are exposed to heavy attenuations and cannot penetrate through several materials, the robustness of reflected propagation paths has been studied in the context of non-line of sight environment [4]-[5].

Furthermore, since the mmWave communication system is expected to operate at a regime with a large number of antennas to extend the communication range, the beam training

process is required. The beam training consists in aligning the Tx and Rx beam pointing directions in order to establish the communication. The speed and complexity of the algorithm for such a process represent a challenge for the use of mmWave systems in mobile environments [6]-[7].

Another major limiting factor of communications in the mmWave frequency bands is the blockage due to moving persons or vehicles located in the beam direction in the propagation environment. Such a phenomenon could lead to abrupt communication interruptions when using narrow beams [8].

Thesis Objectives

The proposed thesis work is generally part of 5G communication in mmWave frequency bands. In the context of the significant attenuation and high sensitivity to obstacles, the main challenge of this PhD thesis is to find innovative techniques allowing the best transmission of 5G services in these frequency bands.

To this end, a state-of-the-art of propagation channels in mmWave frequency bands should be provided. In addition, an in-depth and well-developed study on the sensitivity of mmWave frequency bands to obstacles surrounding the propagation environment could be highlighted. Under these conditions, the thesis should therefore address the evaluation and analysis of radio performance concerning 5G communication. The performance can be evaluated in terms of block error rate, bit error rate, throughputs, communication range and quality of service.

Furthermore, innovative signal processing algorithms could be considered in order to better exploit the availability of frequency resources in mmWaves. It may be to optimize certain physical layer blocks, such as the radio link adaptation algorithm.

And finally, since multi-antenna techniques are also particularly promising because they provide excellent performance, and their size is very small for high frequencies, an exploration of this approach could be attractive. However, other antenna solutions suitable for signal transmission in mmWave frequency bands are also to be considered.

Thesis Contributions

In accordance with the objectives mentioned in the previous section, the following contributions have been addressed in this PhD thesis.

The first contribution is related to the study and analysis of the propagation channels in mmWave frequency bands. Channel characteristics such as the multipath propagation aspect and the blocking phenomenon were highlighted. The state-of-the-art regarding multipath propagation channels and blockage models as well as some existing solutions to combat this drawback is reviewed.

The second contribution and not the least is the study and implementation of the entire 5G physical communication chain in a simulation tool according to the specifications defined by 3rd Generation Partnership Project (3GPP). This communication chain includes the

processing blocks at the Tx and Rx as well as the multipath propagation channel. Simulations are carried out in this context in order to evaluate and analyze the performance of 5G.

The third contribution achieved in this thesis work is the deep analysis of the impact of human (or vehicle) blockage on 5G communication system in mmWave frequency bands. In fact, the analysis of communication performance in terms of block error rate with and without the influence of human blockage is proposed. Based on the block error rate performance, a link budget is also established in order to evaluate the impact of blockage on the cell coverage.

The fourth and last contribution consists in proposing a multibeam antenna modelling in the context of blockage impact mitigation. Using the proposed antenna model, the advantage of multibeam antenna to alleviate the impact of human blockage in millimeter-wave bands is highlighted. The proposed model is generic and can also be used for performance prediction in the design and realization of multibeam antenna systems.

List of Publications:

- **H. Dembélé**, M. Le Bot, F. Gallée, P. Pajusco, "Impact of Human Blockage on 5G Communication System in the 26 GHz Band", in *15th European Conference on Antennas and Propagation (EuCAP)*, Dusseldorf, Germany, March, 2021.
- **H. Dembélé**, M. Le Bot, F. Gallée, P. Pajusco, "Multibeam Antenna Modelling and Blockage Impact Mitigation in 5G Millimeter-wave Band", in *17th International Symposium on Wireless Communication Systems (ISWCS)*, Berlin, Germany, September, 2021.

Thesis Outline

This dissertation draws up the aforementioned contributions through different chapters which are organized as follows.

Chapter 1 briefly presents the 5G technology and its ambitions for the 2020 decade. In this chapter, an overview of use cases and performance requirements are given. Then, the enabling key technologies to meet these requirements are also reviewed.

In **Chapter 2**, a thorough description of the entire 5G physical communication chain is given. To this purpose, a presentation of each of the physical layer transmission steps is performed according to the 3GPP specification. Regarding the reception processing blocks, they are described with reference to other open literature.

Chapter 3 is dedicated to the study and analysis of the channel components such as pathloss, shadowing and multipath propagation in the context of 5G. Different multipath propagation models, in particular resulting from European collaborative projects, are reviewed. The procedure of generating the channel coefficients according to the 3GPP channel model is deeply explained.

Chapter 4 is devoted to the modelling of dynamic blockage phenomenon caused by human or vehicle in mmWave communication systems. A state-of-the-art of various models and solutions proposed in the literature is presented. The statistical model proposed by

3GPP which is based on a random draw of the path angles is presented in details.

In **Chapter 5**, some link-level simulation results in terms of block error rate or bit error rate are presented. Based on these results, our simulation chain is first validated. Then, simulations are also run in order to assess and analyze the impact of human blockage on 5G communication performance.

And finally, **Chapter 6** deals with the multibeam antenna modelling proposed in this PhD work. In fact, multibeam antenna system can be considered as one of the promising solutions to mitigate the blocking phenomenon in the context of mmWave communications. To this end, the proposed antenna model is integrated in the simulation tool in order to show that performance can be improved when the main propagation path is blocked.

Chapter 1

On the 5th Generation of Mobile Communication Systems

1.1 Introduction

Since 2019, mobile phone companies have already started several trial deployments of 5G technology in the world. The number of subscribers to this generation of mobile phone will exceed 2 billion in the coming years. In this context, it is obvious that the proposed network must be flexible and support a lot of data traffic while offering a good quality in terms of connectivity compared to its predecessors. To this purpose, the 3GPP consortium and the International Telecommunications Union-Radiocommunication (ITU-R) have defined several use cases, key technologies and required performance. As this thesis project has been carried out within the framework of 5G communication, a brief description of this technology becomes essential. It is from this perspective that in this first chapter of the thesis manuscript, the vision of 5G technology is reviewed. To do this, the chapter is organized as follows. A general view of 5G including the use cases and performance requirements is given in section 1.2. Section 1.3 is devoted to the analysis of some key technologies that need to be taken into account in the design and deployment of 5G communication systems. And finally, section 1.4 concludes the chapter.

1.2 5G Network Technology

In the following, a brief description of 5G services is given. The targeted applications and some performance requirements in terms of throughputs, latency and network capacity are also reviewed.

1.2.1 Overview of 5G Services

5G or the 5th generation of mobile cellular telephony represents the successor technology to the 4G networks in telecommunications. Compared to its predecessors, 5G communication systems are expected to offer an exceptional range of services or use cases, which are subject to very diverse constraints. Based on the roadmap established by the ITU-R [9] for 2020 and beyond, the 5G use cases are summarized in three main categories as illustrated in Fig. 1.1.

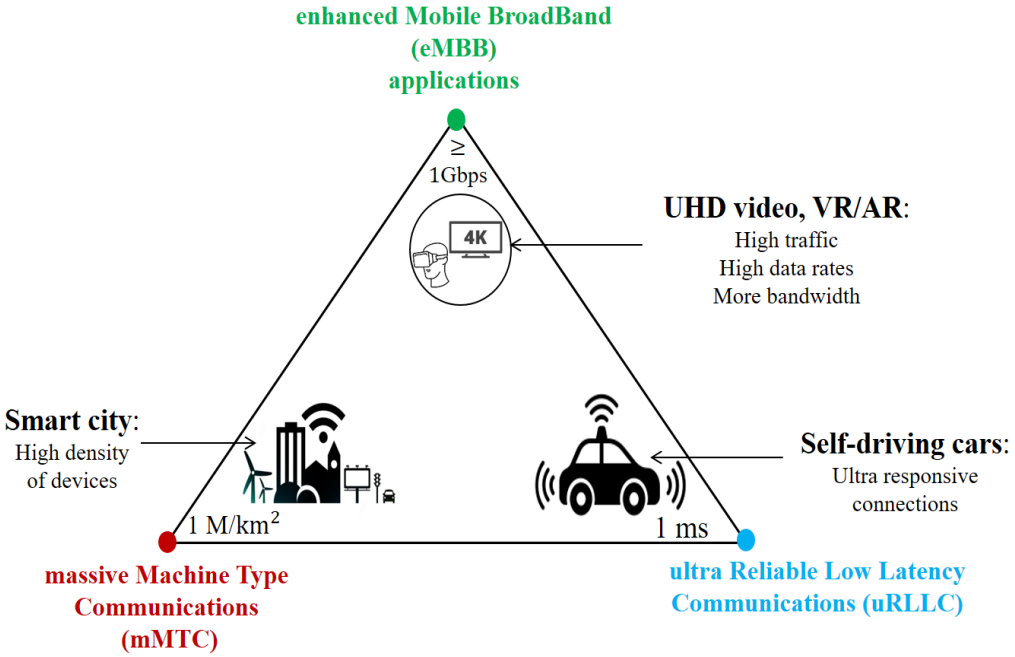

Figure 1.1: 5G ambitions for 2020 and beyond.

In the enhanced mobile broadband (eMBB) category, new applications requiring high data rates such as virtual reality (VR), augmented reality (AR) and ultra–high definition (UHD) video streaming must be accessible, especially in mobility scenarios. This category of use cases can be seen as the extension of classic 4G mobile broadband with significant improvements. The eMBB use case should cover a range of scenarios, from sparsely populated areas, i.e wide-area coverage in rural environments to dense areas such as indoor hotspot connectivity, stadiums, shopping malls, etc., where a higher user density and extremely high throughputs are required.

Regarding the ultra-reliable low latency communications (uRLLC), they represent a set of services that require low latency and strong responsiveness, such as interactive games, drone piloting, remote medical surgery, autonomous or self-driving cars and factory automation. Since these applications involve human safety, extremely stringent reliability and very high security of data are expected.

And finally, due to the proliferation of wireless connected devices since the development of the Internet of Things (IoT) for applications such as smart home, smart cities, etc., the 5G network must support mMTC traffic. In fact, the aim with mMTC services is to provide connectivity to a large number of devices. In this sense, 5G technology should make it possible to develop networks of energy-efficient communicating devices capable of operating for very long periods of time.

1.2.2 5G Performance Requirements

Since the range of multimedia applications and use cases is extremely wide, resulting in very various constraints, efficient and flexible 5G networks must be deployed in order to meet them. These requirements include high capacity of the network, high data rates, very low latency and reliability.

Very High Troughputs

The increase in data rates or throughputs still remains the main and most essential incentive in the evolution of mobile cellular networks. 5G mobile systems are expected to deliver very high data rates greater than 1 Gbps. This means that 5G is ten or even a hundred times faster than current 4G technology.

According to W. Tong and P. Zhu at Huawei [10], 5G technology will need to be able to deliver fiber-like 10 Gbps in terms of throughputs in order to enable eMBB applications which depend on ultra-wide bandwidth and very-low latency. In [11], S. Parkvall *et al.* at Ericsson reviewed the performance requirements in the context of eMBB communications. In fact, they mentioned that for 5G systems, a peak data rate of 20 Gbps is required in downlink while 9.4 Gbps is defined in uplink using a single bandwidth of 400 MHz. Nonetheless, by aggregating two of these carriers which leads to a total bandwidth of 800 MHz, a peak data rate greater than 35 Gbps can be obtained in downlink and more than 10 Gbps in uplink.

In the context of feasibility, in 2016, Korean mobile operator Korea Telecom (KT) with the cooperation of Ericsson demonstrated the world's first 5G with 25.3 Gbps data rates, which is eighty times faster than the current 4G LTE-A [12]. Studies and experiments have been conducted using mmWave frequency bands. In the same year, Ericsson and the telecommunication company Telstra conducted the first live 5G trial on Australian soil in an outdoor real world environment [13]. During the trial, a spectrum of 800 MHz was used, and a throughput greater than 20 Gbps was achieved.

Ultra-Low Latency and Reliability

Due to the targeted applications such as drone piloting, remote surgery or even autonomous cars, 5G mobile technology should also focus on reducing the latency of communication systems in this context. For this purpose, a latency of less than 1 ms has been required by the ITU-R. Andrews *et al.* [14] demonstrated that the 5G technology will need to be able to support a round trip latency of about 1 ms for applications such as interactive gaming, tactile internet and VR/AR. According to the ITU, the tactile internet is an internet where people and objects are connected. In the same way, Nokia mentioned that a round trip time should be lower than 1 ms due to the fact that people are moving towards the era of uRLLC application [15].

As mentioned before, some uRLLC applications involve the management of personal data, high reliability is required. Indeed, reliability highlights the fact that the system is able to provide a service with high level of availability. This means that the error during the communication should be as small as possible. In this sense, Ericsson argues that an availability of 99.999999% must be guaranteed for some industrial applications.

1.2.3 Other Requirements

5G technology is also expected to support mMTC traffic. Indeed, according to the ITU, the connection density in 5G is defined to provide a minimum QoS for 1,000,000 devices per square kilometer. As a lot of objects will be connected, an improvement of network energy efficiency should be ensured by reducing radio frequency (RF) transmit power and saving circuit power. In addition, very low cost devices with long battery life are also claimed. Ericsson estimates the battery life around 10 years.

1.3 5G Enabling Key Features

In order to meet the various requirements, it is naturally obvious that several disruptive technologies must be designed and taken into account in 5G systems.

In fact, 5G can be considered as one of the most innovative technologies for which several solid researches have been carried out in the wireless community by academic and industrial partners. Since 2010, intensive works have been conducted for the development of 5G mobile systems through various European collaborative projects such as One5G [16], mmMAGIC [17], METIS [18], MiWEBA [19], etc. Multiple research studies and experiments have been realized in order to identify some key features required in 5G technology to finally accommodate the performance requirements.

In this section, the goal is to discuss some of these enabling key features for radio access network with a primary focus on eMBB applications.

1.3.1 5G and Massive MIMO Concept

Massive multiple-input multiple-output (mMIMO) is an emerging wireless technology that uses a large number of antennas, in particular at the base station (BS) level. This technology received much attention in recent years in the wireless community. Compared to the 4th generation (4G) standard where up to eight antennas are used, mMIMO has been adopted as one of the key technologies of 5G with the use of over tens (up to hundreds) of antennas [20]. In this way, it has been shown that the performance of MIMO applications can potentially be improved. In fact, thanks to the implementation of multiple antennas at the BS level, multiple users in the same time-frequency resource can be served as illustrated in Fig. 1.2, which improves the system capacity and spectral efficiency. In addition, if the rank of the channel matrix is higher, very good reliability of the communication link through MIMO diversity can be ensured.

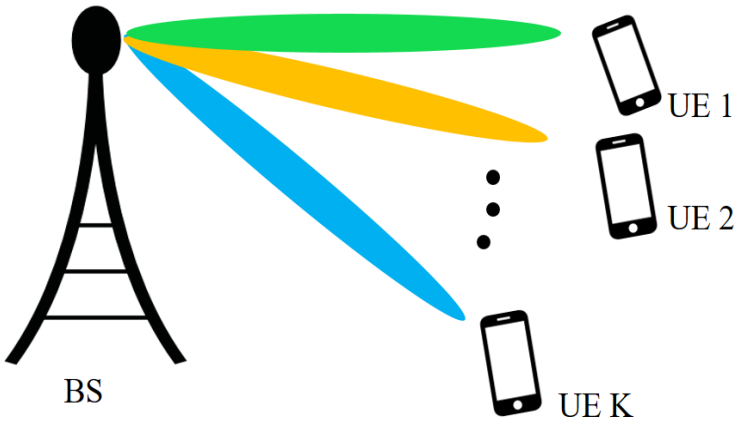

Figure 1.2: Illustration of mMIMO in multi-user MIMO (MU-MIMO) context.

Another and not the least of the advantages of mMIMO is the high gain of beamforming. To this purpose, let's consider the following linear antenna array with N equally spaced isotropic radiating elements as represented in Fig. 1.3 reproduced from [21].

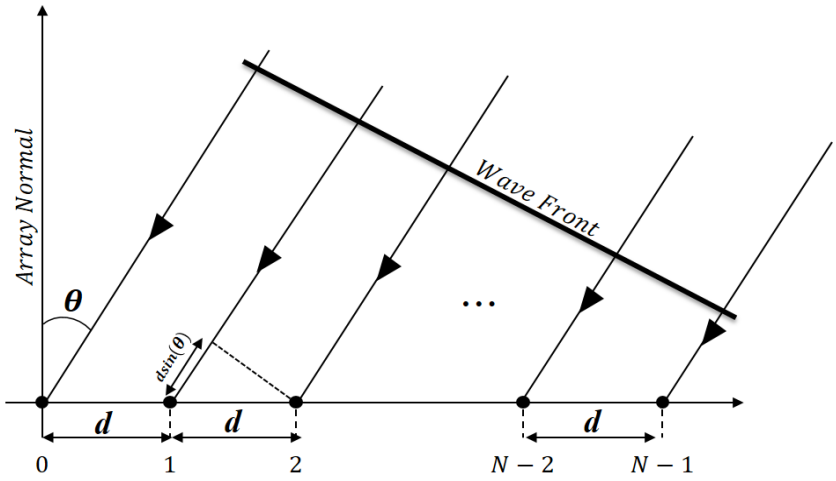

Figure 1.3: Illustration of uniform linear array.

Each radiating element n is weighted by a complex value $V_n = A_n e^{j\alpha_n}$ with $n = 0, ..., N-1$, and the interelement spacing is denoted by d. Assuming that a plane wave impinges the whole array in direction θ with respect to the normal axis, we notice that the wave front arrives at element $n+1$ sooner than at element n. In this way, the radiation pattern of the linear array U_{array} can be approximated by the product of the element radiation pattern $U(\theta)$ by the array factor $AF(\theta)$ as given through,

$$U_{array}(\theta) = U(\theta) AF(\theta), \tag{1.1}$$

with $AF(\theta)$ defined by,

$$AF(\theta) = \left| \sum_{n=0}^{N-1} A_n e^{jn(\alpha+\beta dsin(\theta))} \right|, \tag{1.2}$$

if the phase of the signal at the origin is arbitrarily set to zero and the weight is $V_n = A_n e^{jn\alpha}$. By replacing $\psi = \alpha + \beta dsin(\theta)$ and assuming that $A_n = 1$, (1.2) can be rewritten as,

$$\begin{aligned} AF(\theta) &= \left| \frac{sin\left(\frac{N\psi}{2}\right)}{sin\left(\frac{\psi}{2}\right)} \right| \\ &= N \left| \frac{sinc\left(\frac{N\psi}{2}\right)}{sinc\left(\frac{\psi}{2}\right)} \right|. \end{aligned} \tag{1.3}$$

From (1.3), we can deduce that if the linear phase $\alpha = -\beta dsin(\theta)$, the maximum response of $AF(\theta)$ is achieved in the beam pointing direction, and the antenna array improves the communication range with a beamforming gain of $10\log_{10}(N)$.

As illustrated in Fig. 1.4, the higher the number of antenna elements, the higher the beamfoming gain.

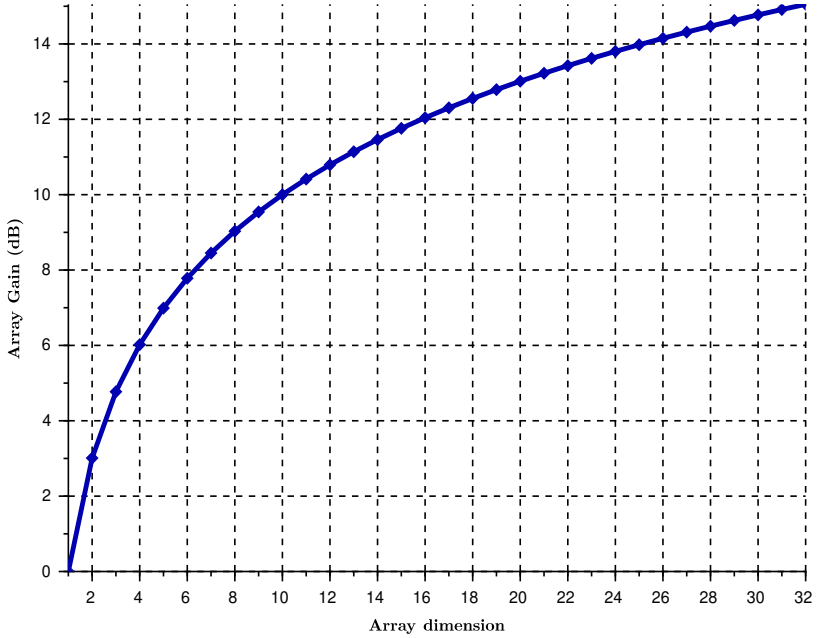

Figure 1.4: ULA gain vs Array dimension.

In Fig. 1.5, the impact of increasing the number of elements while keeping the equidistant spacing constant $d = \frac{\lambda}{2}$ and the beam pointing at $\theta = 0$ is highlighted. We notice that, the main lobe decreases and narrow beam is created for a larger number of antenna elements. Based on these two observations, we can note that the more elements an array consists of, the more directivity will be observed. Then, the effect of increasing the number of antennas results in a larger number of side lobes with an overall decrease in amplitude. Therefore, user-to-user interference in the MU-MIMO context can be mitigated.

Although several advantages make mMIMO a promising candidate for 5G communication systems, there are many challenges that need to be considered in designing such technology.

One of the conventional limitations of mMIMO systems is the hardware impairment as discussed below. In fact, due to the large number of antennas, and in order to reduce the system cost, all or most of the building blocks for a phased array are integrated on a single silicon chip which is cheaper. This results in higher noise in the communication system according to Kim *et al.* [23]. They also showed that the larger the antenna array, the higher the phase noise. In fact, the phase noise can be considered as a set of random fluctuations in the phase of the signal due to the frequency offset of the oscillator. In the same way, Gustavsson *et al.* [24] claimed that the low cost RF components or chains significant limits the system performance due to several hardware impairments.

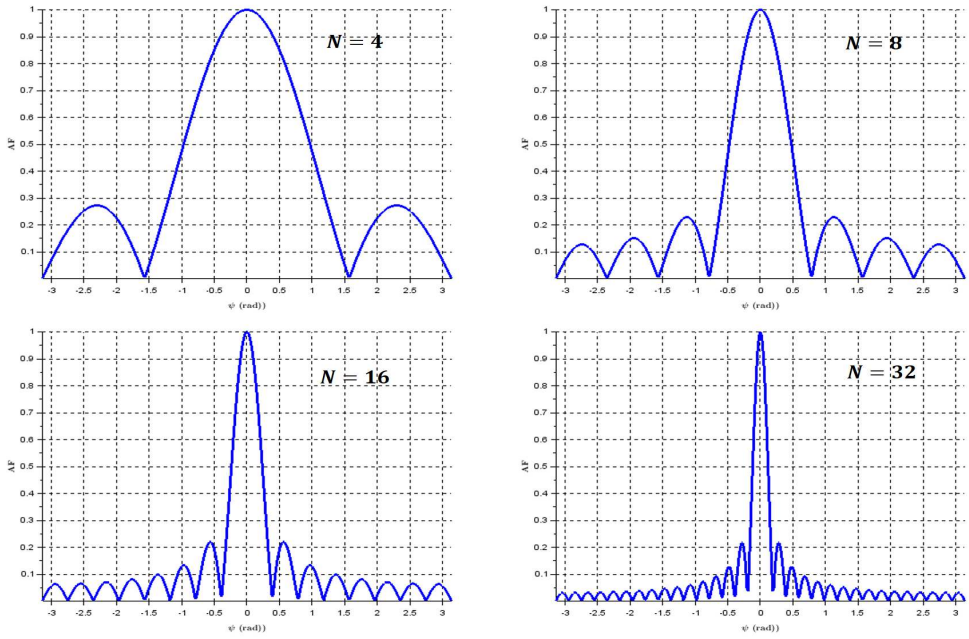

Figure 1.5: Normalized AF for $N = 4, 8, 16, 32$.

Furthermore, as mMIMO technology for 5G systems is expected to be deployed more in time division multiplex (TDD) than frequency division multiplex (FDD), the channel reciprocity for the channel state information (CSI) at the BS is not ensured. In fact, the CSI represents a set of information on the state of radio communication link between the Tx and Rx. And in TDD mode, the CSI is acquired by the Tx via channel reciprocity. Actually, as mentioned in [25], the disadvantage of the reciprocity is the components of RF chain at the BS and the user equipment (UE) which have different frequency transfer characteristics as the channel is in practice measured from the RF chains. Thus, both uplink and downlink chains must be equalized by a calibration method, which is expensive.

In addition, the large number of antennas requires high complexity in terms of signal processing algorithms at the Rx. Then, there is an expensive system due to the spacing between antenna elements which is very low, in particular at high frequencies. All this makes the design of this technology more complex and costly in time and effort.

1.3.2 Small Cells for Network Densification

According to the ITU ambitions in the context of 5G, the network densification represents one of the key technologies for enabling higher data rates. In fact, densifying the network involves adding a large number of small cells in the existing macro cells as illustrated in Fig. 1.6.

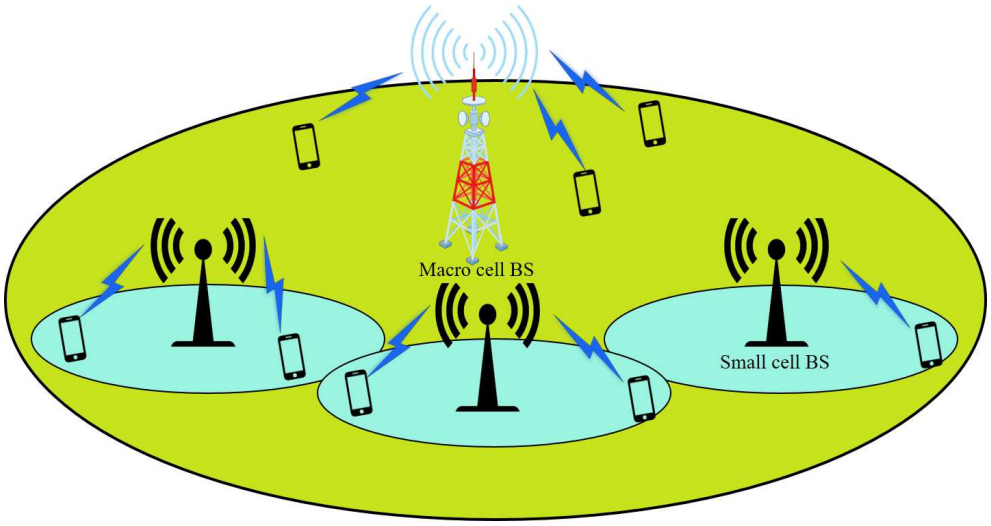

Figure 1.6: Illustration of network densification.

The deployment of small cells, ranging from micro cells to femto cells, is advantageous in that it will increase the rate of spectrum reuse as the cell size becomes smaller. In this context, we talk about a heterogeneous network (HetNet) due to the fact that the network incorporates several cells with different sizes. HetNets have become important for telecommunications operators due to the number of subscribers which increases over the years with high demand for data.

Nonetheless, the deployment of high number of cells in Hetnets faces many challenges that need to be addressed in order to meet with the aforementioned benefits.

According to Romanous *et al.* [26], the sheer number of BS can be source of interference. Actually, the Hetnet is composed of macro cell BS and different small cell BSs which are generally deployed for indoor scenarios (home users or enterprises) for which the signal from macro cell BS is weak.

Due to the fact that the small cell BSs are connected to the macro cell BS, two types of interference are highlighted: interference between small cell BSs and macro cell UEs, and interference with neighbouring small cell UEs.

In addition, one of the most challenging limitations facing network densification is the issue of energy efficiency management. In fact, while network densification is an effective method of increasing system capacity and coverage, such improvement comes primarily at the expense of increasing power consumption as also discussed in [26].

Finally, to the challenges mentioned above, we can also note that a large number of small cells could result in the high frequency of handovers and the mobility management of the UEs in the HetNet.

1.3.3 mmWave Frequency Bands for 5G eMBB

As mentioned in the introduction of the chapter, the world of wireless telecommunications has undergone considerable technological development for several years. However, the allocation of spectrum for cellular networks has not kept pace with these tremendous technological breakthroughs. In fact, almost all mobile communication systems are deployed in the frequency bands below 6 GHz which are becoming increasingly crowded due to the exponential growth of the mobile data traffic. To address this problem, the use of millimeter-wave (mmWave) frequency bands where a large amount of bandwidths remains underutilized, becomes inevitable.

Theoretically, mmWaves represent electromagnetic waves typically defined for frequencies ranging from 30 to 300 GHz, which corresponds to wavelengths in the range between 1 and 10 mm as explained in Fig. 1.7.

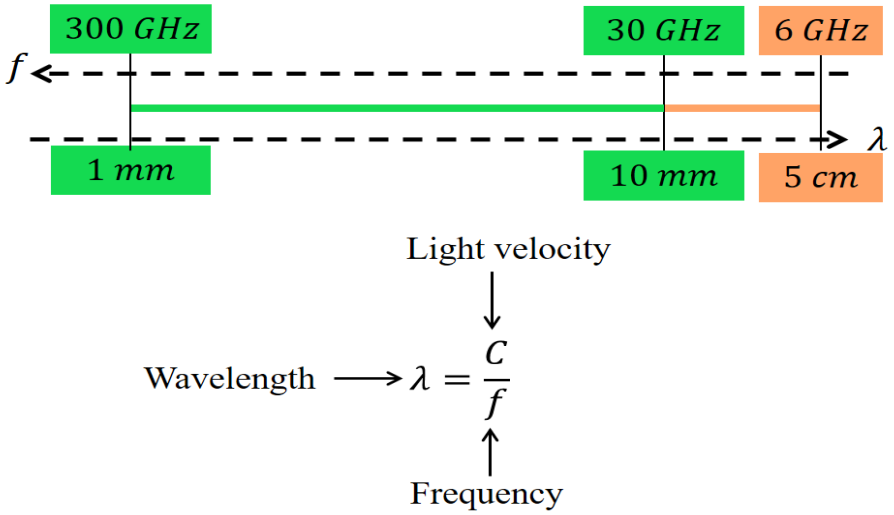

Figure 1.7: Properties of millimeter waves.

Nonetheless, in the wireless community, mmWave communication systems mostly refer to systems that operate in frequency bands above 6 GHz. In [27], Pi and Khan claim that mmWave frequency bands refer to 3−300 GHz spectrum with wavelengths ranging from 1 to 100 mm due to the fact that this spectrum shares similar propagation characteristics with the 30−300 GHz frequency band. In this context, regarding the 5G ambitions, several mmWave frequency bands have been identified by the ITU at the World Radiocommunication Conference in 2015 (WRC-15).

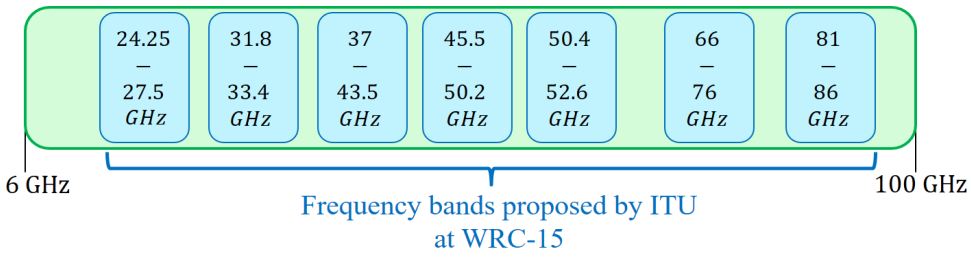

Figure 1.8: mmWave frequencies for 5G [28].

These frequencies are highlighted in Fig. 1.8 and include 4.25−27.5 GHz, 31.8−33.4 GHz, 37−43.5 GHz, 45.5−50.2 GHz, 50.4−52.6 GHz, 66−76 GHz and 81−86 GHz.

The availability of a huge amount of spectrum makes mmWave bands a real opportunity for 5G eMBB in the sense that multigigabit data rates can be achieved. However, compared to wireless systems below 6 GHz, communicating in this region of frequencies presents many challenges that must be taken into account.

In fact, electromagnetic waves suffer from high propagation loss in mmWave frequency bands, in particular free-space pathloss which is given by Friis' formula for isotropic antennas. As illustrated in Fig. 1.9, we notice that the higher the frequency, the higher the propagation loss for a distance of 200 m. To this end, the common way in the mmWave communication context is to use multiple antennas in order to make communication directional through the beamforming technique as explained in section 1.3.1. The advantage with mmWave frequencies is the fact that with shorter wavelengths, more antennas can be packed into an area, compared to lower frequencies if the antenna area is kept constant.

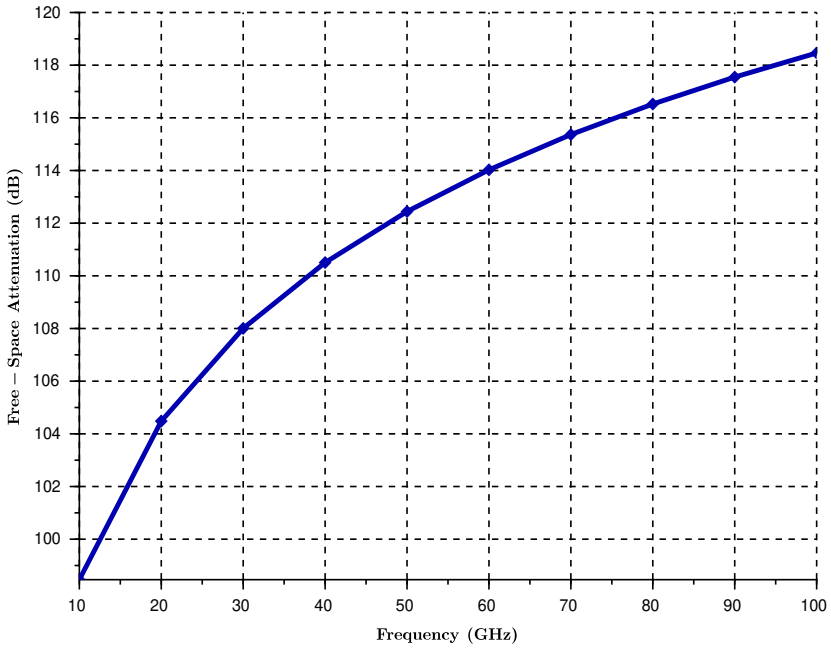

Figure 1.9: Free-space attenuation vs Frequency.

In addition to the propagation loss, the communication in mmWave bands faces other challenges such as oxygen absorption, rain attenuation, foliage loss and the sensitivity to the blockage effect. As this PhD thesis focuses on 5G communication in mmWave frequency bands, some of these challenges mentioned are detailed in the next chapters.

1.4 Conclusion

This first chapter of the manuscript was mainly about an introduction to 5G technology. To this end, the 5G ambitions for 2020 and beyond, particularly in terms of data rates

and latency for services such as eMBB and uRLLC applications, have been reviewed. In this context, more details on key performance regarding these use cases have also been given. In addition, in order to meet the performance requirements, 5G relies on some core technologies such as massive MIMO, network densification and mmWave frequency bands. The advantages and challenges associated with these 5G technologies have been pointed out. In the next chapters, the 5G NR physical layer and the mmWave propagation channel modelling are deeply highlighted.

Chapter 2

Physical Layer Processing Blocks for 5G Technology

2.1 Introduction

This chapter aims at highlighting in details the 5G physical (PHY) layer designed for the transmission of physical downlink shared channel (PDSCH), which is used for all the simulations carried out in my thesis project for data transmission. The processing blocks of this PHY layer described here generally specify the multiplexing, channel coding, and modulation of the binary data in the downlink transmission. In the communication chain, the processing blocks on the transmitter (Tx) side are basically described according to the standardization proposed by 3GPP in release 15. However, on the receiver (Rx) side, the corresponding processing blocks are studied and implemented according to other open literature. The implementation of all the transmission and reception chains of PDSCH PHY layer has been achieved in Galacsy that represents a C++ simulation environment used in the thesis project. For the rest, the chapter is organized as follows. Section 2.2 gives an overview of the PHY transmission chain as proposed by 3GPP for PDSCH channel. From section 2.3 to section 2.11, the different blocks are explained in more details regarding the transmission processing and reverse processing at the Rx level. And finally, section 2.12 summarizes the chapter.

2.2 Overview of PDSCH PHY Layer

The goal of this section is to give an overview of the downlink transmission chain in which the processing blocks are represented in sequential way, one after the other as depicted in Fig. 2.1. The figure shows that, after the generation of downlink shared channel (DL-SCH) transport block by the bit generator, a sequence of cyclic redundancy check (CRC) bits is computed and attached to this one before low-density parity check (LDPC) encoding and rate matching processing. Due to the size of LDPC encoding matrix which is fixed, some operations of segmentation can be performed if the DL-SCH transport block is greater than a certain size or zero padding is realized in case DL-SCH is smaller. Before the MIMO precoding, binary data are scrambled and modulated in complex-value symbols. After MIMO precoding, complex symbols are mapped on the resources grid and frequency-division multiplexing (OFDM) modulation is achieved.

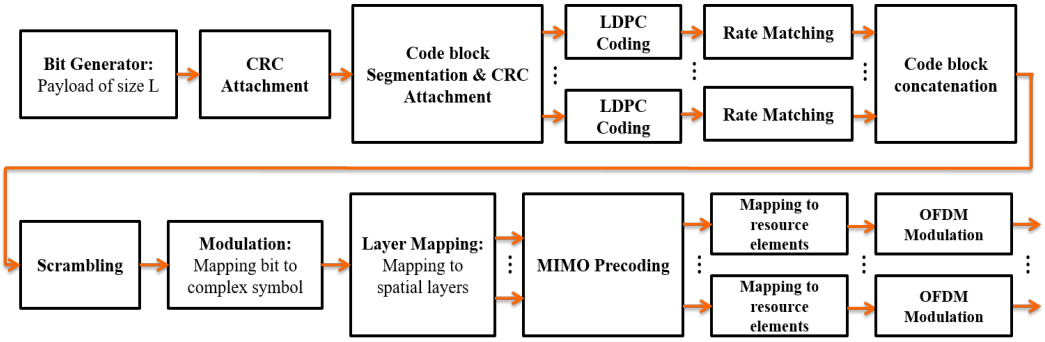

Figure 2.1: Overall transmission chain.

2.3 Cyclic Redundancy Check

2.3.1 Description

The CRC is an error-detection technique invented by W. Wesley Peterson in 1961, which is widely used in digital communication systems. The CRC is a sequence of fixed-length check bits often called a *checksum* computed from the message that needs to be transmitted (*transport block*) and appended to the transport block to ensure data integrity on reception. When the CRC computed from the received transport block is different from the one attached to the transport block at the Tx level, the block is rejected by the PHY layer and a retransmission is requested through a negative acknowledgement (NACK). Otherwise, the block is transmitted to the upper layers and an acknowledgement (ACK) is sent to the Tx. The following figure gives an overview of the attachment of M redundant bits to the message bits of size L in systematic CRC mechanism.

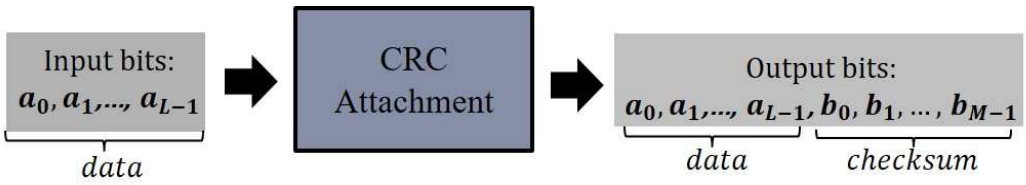

Figure 2.2: Systematic CRC attachment.

2.3.2 Theory of CRC Computation

The idea behind the CRC calculation algorithm is to consider the message as a binary number and divide this number by another binary number called *generator polynomial*. The rest of this division represents the checksum to append to the message for the transmission as depicted in Fig. 2.2. In the same way, data integrity is checked by the Rx through the division of the decoded binary message including the CRC redundant bits by the same generator polynomial. If the rest is zero, the transmission is successful, in other words a NACK is fed back. The division between the binary numbers to find the checksum is simply illustrated by using equivalent polynomials $m(x)$ and $G(x)$ representing the message and CRC generator, respectively. The algorithm of calculation is given in Fig. 2.3, where M is both the degree of generator polynomial G and the length of the checksum to append to the message as mentioned before.

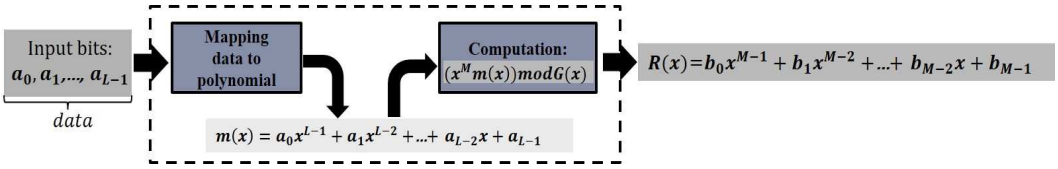

Figure 2.3: CRC computation.

The CRC redundant bits are the coefficients of polynomial $R(x)$, which represents the rest of the euclidian division of $x^M m(x)$ by $G(x)$. An example of CRC bits computation is highlighted in Fig. 2.4. $m = 111 \Rightarrow m(x) = x^2+x+1$ and $G = 1011 \Rightarrow G(x) = x^3+x+1$ whose degree is $M = 3$. From m and G, $x^3 m(x) = x^5 + x^4 + x^3$, which is equivalent to the binary sequence 111000.

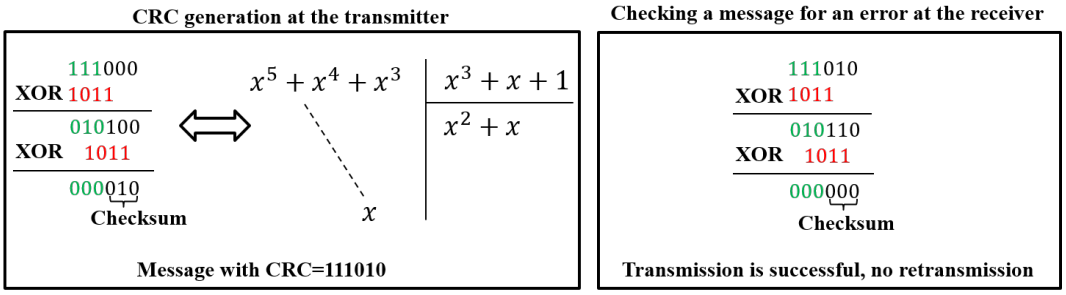

Figure 2.4: Example of CRC attachment and message checking.

The rest of the euclidian division of $x^M m(x)$ by $G(x)$ is realized by XOR operation between 101000 and 1011 as follows by aligning the leading "1" of the divisor with the first "1" of the dividend in each step of the division.

2.3.3 DL-SCH CRC Attachment

The CRC attachment to the DL-SCH transport block follows the the procedure described in sections 2.3.1 and 2.3.2 of [31]. $M = 24$ CRC redundant bits are computed and attached with the generator polynomial $G(x) = x^{24} + x^{23} + x^{18} + x^{17} + x^{14} + x^{11} + x^{10} + x^7 + x^6 + x^5 + x^4 + x^3 + x + 1$ if the size of the transport block $L > 3824$, and $M = 16$ CRC redundant bits are attached with $G(x) = x^{16} + x^{12} + x^5 + 1$ if $L \leq 3824$.

2.4 Code Block Segmentation and Concatenation

2.4.1 Definition

The segmentation of the transport block after the CRC attachment depends on the channel coding. The purpose of this processing is to ensure the appropriate size of the block for the channel coding based on the use of a pre-proposed matrix with known dimensions [33]. In fact, the idea of segmentation is simple: when the size of transport block exceeds the size required by the channel coding matrix, the transport block is divided into a minimum number of blocks whose sizes are consistent with the encoding matrix through the procedures of zero padding and attachment of additional CRC. Each block resulting from the segmentation is individually encoded by the channel coding algorithm. However, when the size of the transport block is smaller than that required for channel coding, no

segmentation occurs, only the zero padding mechanism is proposed.

Likewise, as Low density parity check (LDPC) is proposed as channel coding technique for the DL-SCH, the approach of code block segmentation is illustrated in section 2.4.2. The additional CRC in this processing is justified by the fact that if the mechanism of retransmission is ideally implemented in the communication chain and the Rx after decoding rejects one of blocks by focusing on the CRC procedure described in section 2.3, it is unnecessary to decode the remaining blocks and a NACK is immediately sent to the Tx for all the transport block DL-SCH. After channel coding and rate matching processing completed individually for all the blocks resulting from the segmentation operation, these are sequentially concatenated one after the other to form a single codeword transmitted on the physical channel PDSCH.

2.4.2 Segmentation for LDPC

For the LDPC encoding for the DL-SCH, two parity check matrix (PCM) are proposed: LDPC based graph 1 for which the maximum code block size required for the segmentation is $K_{CB} = 8448$ and LDPC based graph 2 with $K_{CB} = 3840$. For both matrices, and in case of segmentation, the additional CRC of $M = 24$ bits must be attached to each block. The number of blocks resulting from the segmentation is given by $N_{CB} = \left\lceil \frac{B}{K_{CB}-M} \right\rceil$, with B the size of the transport block after the CRC attachment processing described in section 2.3. The size of each block after the segmentation is $22Z_c$ for LDPC based graph 1 and $10Z_c$ for LDPC based graph 2. The parameter Z_c called *lifting* or *expansion parameter* is chosen from Table 2.1 such that $22Z_c \geq B_{single}$ for LDPC based graph 1 and such that $K_b Z_c \geq B_{single}$ for LDPC based graph 2 where $K_b = 10$ for $B > 640$, $K_b = 9$ for $B > 560$, $K_b = 8$ for $B > 192$ and $K_b = 6$ for $B < 192$. $B_{single} = \frac{B+N_{CB}M}{N_{CB}}$ represents the number of bits in each block, without zero padding bits.

Table 2.1: Sets of LDPC lifting size Z_c [31].

Set index I_{LS}	Set of lifting sizes Z_c
0	$\{2, 4, 8, 16, 32, 64, 128, 256\}$
1	$\{3, 6, 12, 24, 48, 96, 192, 384\}$
2	$\{5, 10, 20, 40, 80, 160, 320\}$
3	$\{7, 14, 28, 56, 112, 224\}$
4	$\{9, 18, 36, 72, 144, 288\}$
5	$\{11, 22, 44, 88, 176, 352\}$
6	$\{13, 26, 52, 104, 208\}$
7	$\{15, 30, 60, 120, 240\}$

2.5 5G LDPC Codes for DL-SCH

2.5.1 Introduction

LDPC codes have been introduced by Robert G. Gallager in the 1960's [35] and used in recent years in several standards such as DVB (Digital Video Broadcasting), IEEE 802.11n, IEEE 802.16e [36]. And today it is standardised by 3GPP as channel coding technique for the transport blocks DL-SCH and UL-SCH in 5G NR downlink and uplink, respectively. As any block linear code, the LPDC code is fully characterized by its PCM $\underline{\mathbf{H}}$, i.e for any codeword $\mathbf{C}$, the parity-check equations defined by $\mathbf{C}\underline{\mathbf{H}}^T = \mathbf{0}$ must be satisfied. In other words, the PCM $\underline{\mathbf{H}}$ can be seen as the set of constraints that must be

fulfilled the bits encoded with each other to form a codeword. The PCM of LDPC codes has the particularity to be sparse, which is justified by the fact that only a small fraction of entries of $\underline{\mathbf{H}}$ is nonzero. Like the encoding, the LDPC decoding algorithms are also based on the PCM and naturally described using a bipartite graph called *Tanner graph*. In fact, Tanner graph contains two sets of nodes, *bit* or *variable* nodes corresponding to the columns of the PCM $\underline{\mathbf{H}}$ and *constraint* or *parity* nodes which represent the rows of $\underline{\mathbf{H}}$. An illustration of such graph is depicted in Fig. 2.5.

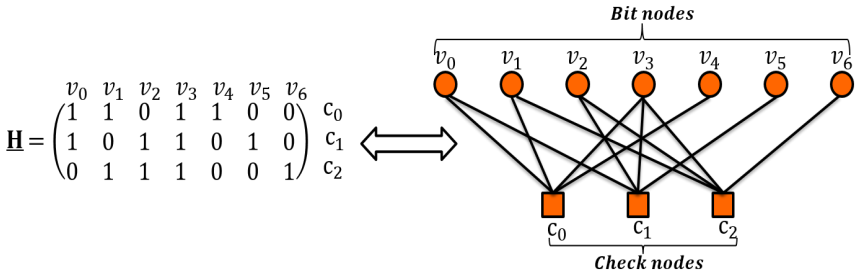

Figure 2.5: Illustration of Tanner graph.

A "1" in $\underline{\mathbf{H}}$ located at position (i, j) represents an edge between check node i and bit node j. The number of edges connected to a node is called *degree*. Fig. 2.5 shows that for example at the check node c_0 with degree 4, the parity is satisfied through $v_0 \oplus v_1 \oplus v_3 \oplus v_4 = 0$. For the rest of this section, the construction of LDPC codes for the transport block DL-SCH and the decoding algorithm used at the receiver level are detailed.

2.5.2 LDPC Codes for 5G NR

LDPC codes have been selected for 5G NR data communication as the channel coding scheme especially for enhanced mobile broadband (eMBB) applications. 5G NR LDPC codes use quasi-cyclic (QC) structure with a low-complexity in terms of hardware implementation and the sparseness of the PCM [37]. They are designed to support several lifting values Z_c [38] whose values are indicted in Table 2.1. The encoding system is systematic and focused on protograph-based LDPC (PB-LDPC) codes [39] defined by a smaller base matrix **BG** with each entry corresponding to either a $Z_c \times Z_c$ zero matrix or a shifted $Z_c \times Z_c$ identity matrix, where a cyclic shift given by a shift coefficient to the right of each row is applied. For 5G communication, two types of PB-LDPC codes matrices have been constructed, LDPC base matrix 1 **BG1** and LDPC base matrix 2 **BG2** as mentioned in section 2.4.1 whose parameters are given in Table 2.2.

Table 2.2: 5G NR PB-LDPC codes matrix parameters.

Parameters	Base matrix 1	Base matrix 2
Mother code rate	1/3	1/5
Matrix size	46×68	42×52
Number of systematic columns K_b	22	10
Maximum information block size K	8448	3840

The maximum information block size K for each **BG** corresponds to $K_b Z_{c_{max}}$, with $Z_{c_{max}} = 384$ the maximum lifting size. By referring to Table 2.1, 51 PCMs are defined for each base matrix resulting in 102 for 5G NR data communication. In fact, **BG1** is used for large systematic block sizes and high code rates, up to 8/9, while **BG2** is rather optimized for small systematic blocks and low code rates, up to 2/3 [37].

The procedure of LDPC base matrix selection among both **BG1** and **BG2** is depicted in Fig. 2.6 for DL-SCH transport block.

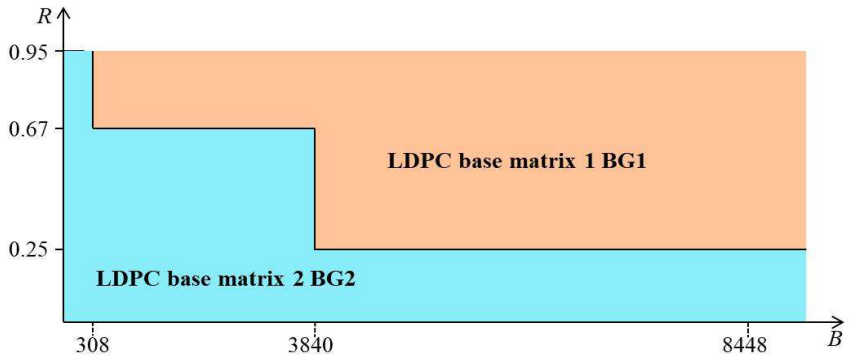

Figure 2.6: LDPC base matrix selection.

The figure shows the regions for selecting **BG1** and **BG2** as LPDC base matrix for 5G data channel coding. These regions are defined from code rate R and transport block size B after initial CRC attachment. On the one hand, for $B \leq 308$ and whatever the value of code rate, LDPC base matrix 2 is used due to its performance in this range. On the other hand, for $R \leq 0.25$ LDPC base matrix 2 still performs better than LDPC base matrix 1 for any size of transport block B. For $308 < B \leq 3840$ and $R \geq 2/3$ or $3840 < B \leq 8448$ and $R > 0.25$ LDPC base matrix 1 is preferred instead of LDPC base 2 for channel coding. Nonetheless, both base matrices have the same general structure composed of 5 submatrices $\underline{\mathbf{A}}$, $\underline{\mathbf{B}}$, $\underline{\mathbf{C}}$, $\underline{\mathbf{0}}$ and $\underline{\mathbf{I}}$ as given in Fig. 2.7. The columns of 5G NR **BG1** or **BG2** are organized into 3 parts: the transport block after the CRC attachement and code block segmentation corresponding to systematic columns, core parity columns and extension parity columns. The rows are divided into main parts: core checks and extension checks.

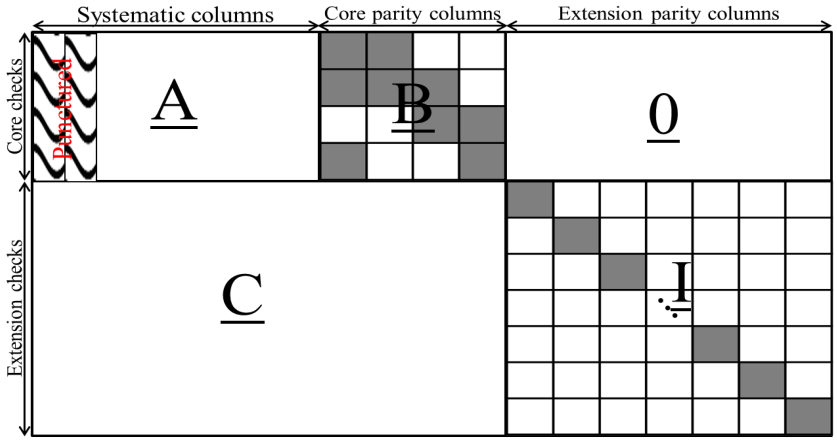

Figure 2.7: LDPC base matrix 1 structure.

Submatrix $\underline{\mathbf{A}}$ in which the first 2 columns are punctured, fully represents the portion of systematic bits. 2 sets of parity bits are derived. The set represented by the square submatrix $\underline{\mathbf{B}}$ with the upper double-diagonal structure except the first column, which is defined for core columns of parity bits. $\underline{\mathbf{0}}$ is the submatrix whose all entries are zero, which corresponds to the columns of extension parity bits. The difference with the LDPC

base matrix 2 structure is due to gray square 2 in the first column of $\underline{\mathbf{B}}$, located at position row 2 instead of 1 as illustrated in Fig. 2.7. The concatenation of submatrices $\underline{\mathbf{A}}$ and $\underline{\mathbf{B}}$ corresponds to the encoding process kernel, especially for higher code rates. $\underline{\mathbf{C}}$ corresponds to the extension rows of LDPC base matrix used when lower code rates are used [38]. $\underline{\mathbf{I}}$ is a block identity matrix. Gray squares in the figure represent a shifted $Z_c \times Z_c$ identity matrix in the PCM with shifted values defined by $mod\,(V_{i,j}, Z_c)$ and white squares represent $Z_c \times Z_c$ zero matrix. $V_{i,j}$ is the value at position (i, j) in the LDPC base matrix. 8 LDPC base matrices are proposed, each corresponding to the set index I_{LS} selected from Z_c focusing on Table 2.1.

2.5.3 Decoding of LDPC Codes

LDPC decoding algorithms are iterative and only based on message passing between bit nodes and check nodes through the edges in the Tanner graph whose an example is given in Fig. 2.5. As in conventional way, an iterative LDPC decoding algorithm starts with initial messages which are observations at bit nodes received from the output of demodulator, and these observed values are then passed to check nodes. Furthermore, at each iteration two events take places: 1-the check nodes process information received for updating their initial beliefs (or values) and send the processed messages back to the bit nodes. 2-the bit nodes in their turn, update their previous values (or beliefs) and send the updated information back to the check nodes. The values returned to the check nodes ensure the reliability of the bit nodes [44]. During each iteration, a decision on the value of each bit node can be made to decide if it is bit "0" or "1" and the decoding algorithm stops if a codeword is found or the the maximum number of iterations is reached.

In the open literature, two sets of LDPC decoding exist: *hard decision decoding* and *soft decision decoding*. In the hard decision decoding, the messages exchanged between nodes are "0" and "1" and one of the best algorithms is *bit flipping algorithm* as illustrated in [42]-[43]. For the soft decision decoding, the messages propagated through the edges in the graph are soft (not binary) and they represent probabilities, also called *beliefs*. In the rest of this section on decoding of LDPC codes, the soft decision decoding and the derived algorithms will be highlighted.

Initial LLR Messages

Constellation symbols received y_v after the equalization operation are demapped by the soft demodulator by using *maximum a posteriori (MAP)* probability to produce initial beliefs regarding the received bit node "$v = 0$" or "$v = 1$", which are expressed in *Log-Likelihood Ratio (LLR)* defined by,

$$v^0 = ln\left(\frac{Pr\,(y_v|v=0)}{Pr\,(y_v|v=1)}\right). \tag{2.1}$$

By using the Bayes rule, (2.1) is rewritten as,

$$v^0 = ln\left(\frac{Pr\,(v=0|y_v)}{Pr\,(v=1|y_v)}\right). \tag{2.2}$$

Let s be the transmitted constellation symbol, the equalized symbol x at the receiver is expressed such as $x = s + n$ where n represents the noise sample of probability density function (pdf) f_n. Let S_0^j and S_1^j be the sets of constellation symbols corresponding to

bits "0" and "1" respectively, in the j^{th} bit position in the symbol. As intuitively and naturally proposed by Viterbi in [47] and Ayyar *et al.* in [48], the LLR of the j^{th} coded bit node is defined from (2.2) by,

$$v_j^0 = ln\left(\frac{\sum_{s_0 \in S_0^j} f_n\left(x - s_0\right)}{\sum_{s_1 \in S_1^j} f_n\left(x - s_1\right)}\right). \tag{2.3}$$

As proposed in [49], the expression of v_j^0 in (2.3) can be naturally approximated by,

$$v_j^0 \approx ln\left(\frac{f_n\left(\underset{s_0 \in S_0^j}{\operatorname{argmin}}\left(x - s_0\right)\right)}{f_n\left(\underset{s_1 \in S_1^j}{\operatorname{argmin}}\left(x - s_1\right)\right)}\right). \tag{2.4}$$

In this study, by considering that noise samples are Gaussian and complex with mean 0 and variance σ^2, i.e $f_n\left(b\right) = \frac{1}{\pi\sigma^2} e^{-\frac{|b|^2}{2\sigma^2}}$, the final expression of initial belief or LLR of bit nodes can be readily justified by,

$$v^0 = -\frac{1}{\sigma^2}\left(\underset{s_0 \in S_0}{\operatorname{argmin}}|x - s_0|^2 - \underset{s_1 \in S_1}{\operatorname{argmin}}|x - s_1|^2\right). \tag{2.5}$$

Sum-Product (SP) Algorithm

In the case of a Tanner graph without a cycle, the messages propagated through the edges are independent and the demodulator uses MAP probability to compute the initial messages that represent the beliefs. Actually, the Tanner graph of the LDPC codes contains a cycle and the *independence assumption* cannot be applied. However, more the PCM is sparse (that is the case with 5G NR LDPC codes), more the assumption of a graph without a cycle becomes true, and the MAP probability can be used to produce the beliefs [46]. Considering a parity check equation c including a set of bit nodes V_c, the Bayes rule applied at bit node v gives the following probabilities conditional on the received sequence $\{y\}$,

$$Pr\left\{v = 0|y\right\} = Pr\left\{\left(\sum_{v' \in V_c \backslash v} v'\right) = 0 \mid \left\{y'\right\}\right\}, \tag{2.6}$$

and,

$$Pr\left\{v = 1|y\right\} = Pr\left\{\left(\sum_{v' \in V_c \backslash v} v'\right) = 1 \mid \left\{y'\right\}\right\}, \tag{2.7}$$

with the sum operation applied in modulo 2 and $\{y'\}$ the received sequence except the observed value at bit node v. Under the independence assumption, from [45] we show that,

$$2Pr\left\{\left(\sum_{v' \in V_c \backslash v} v'\right) = 0|\left\{y'\right\}\right\} - 1 = \prod_{v' \in V_c \backslash v}\left(2Pr\left(v' = 0|y'\right) - 1\right), \tag{2.8}$$

$$2Pr\left\{\left(\sum_{v'\in V_c\backslash v} v'\right) = 1|\left\{y'\right\}\right\} - 1 = -\prod_{v'\in V_c\backslash v}\left(2Pr\left(v'=1|y'\right)-1\right), \tag{2.9}$$

with y' the observed value at bit node v'. By defining,

$$L_{v'} = \frac{Pr\left(v'=0|y'\right)}{Pr\left(v'=1|y'\right)} = \frac{Pr\left(v'=0|y'\right)}{1-Pr\left(v'=0|y'\right)}, \tag{2.10}$$

the conditional likelihood of v', we also show that,

$$\begin{aligned} 2Pr\left(v'=0|y'\right)-1 &= \frac{L_{v'}-1}{L_{v'}+1} \\ &= \frac{e^{ln(L_{v'})}-1}{e^{ln(L_{v'})}+1} \\ &= tanh\left(\frac{ln\left(L_{v'}\right)}{2}\right). \end{aligned} \tag{2.11}$$

From (2.8), (2.9) and (2.11), the likelihood of v at the parity equation c is hereby defined,

$$L_v = \frac{1+\prod_{v'\in V_c\backslash v} tanh\left(\frac{L'}{2}\right)}{1-\prod_{v'\in V_c\backslash v} tanh\left(\frac{L'}{2}\right)}, \tag{2.12}$$

with $L' = ln\left(L_{v'}\right)$, which defines the LLR at bit node v'. This result given in (2.12) will represent the base for the description of the Belief Propagation (BP) or Sum-Product (SP) algorithm, which is considered as the best performing algorithm and proposed by Gallager in the LDPC soft decision decoding context. As previously mentioned, the SP algorithm is composed of two steps at each iteration: 1-propagation of messages from bit nodes to check nodes and 2-propagation of beliefs from check nodes to bit nodes.

Messages from bit nodes to check nodes

Let m_{vc} be the message passed from the bit node v to the check node c. The update of m_{vc} during the iteration i is highlighted through,

$$m_{vc}^{i} = \begin{cases} m_{vc}^{0} & if\ i=0 \\ m_{vc}^{0} + \sum_{c'\in C_v\backslash c} m_{c'v}^{i-1} & if\ i\geq 1 \end{cases}. \tag{2.13}$$

and described by Fig. 2.8 from the corresponding Tanner graph.

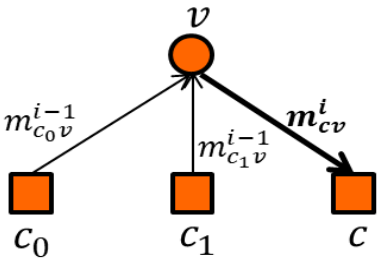

Figure 2.8: Belief propagation from bit node to check node.

In (2.13), $m_{vc}^{0} = v^0$ is the initial LLR from the output of the demodulator as detailed in subsection 2.5.3 and given by (2.5). C_v represents the set of check nodes connected to the bit node v and $m_{c'v}^{i-1}$ is the message passed from the check node c' to the bit node v as depicted in the next paragraph at round $i-1$.

Messages from check nodes to bit nodes

The message passed from the check node c to the bit node v is denoted by m_{cv} whose value at the iteration i is defined in SP algorithm from (2.12) by the following,

$$m_{cv}^{i} = ln\left(\frac{1+\prod_{v'\in V_c\setminus v} tanh\left(\frac{m_{v'c}^{i-1}}{2}\right)}{1-\prod_{v'\in V_c\setminus v} tanh\left(\frac{m_{v'c}^{i-1}}{2}\right)}\right), \tag{2.14}$$

where $m_{v'c}^{i-1}$ is the message passed from the check node v' to the bit node c during the iteration $i-1$, and V_c the set of bit nodes incident to the check node c. An illustration of message passing from check node to bit node is described in Fig. 2.9.

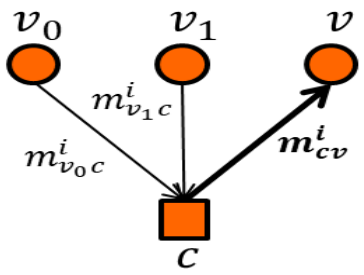

Figure 2.9: Belief propagation from check node to bit node.

Decoding attempt of bit nodes

During the iteration, the decoding of bit (or information) nodes could be performed, and this mechanism is essentially based on the computation of *a posteriori information* expressed by A_v if the decoding is performed for the bit node v. The value of A_v at round i is hereby defined,

$$A_v^i = m_{vc}^0 + \sum_{c'\in C_v} m_{c'v}^i. \tag{2.15}$$

The decision on the bit node v is defined by (2.16) in most literatures [43] from a posteriori information A_v.

$$v = \begin{cases} 0 & if\ A_v \geq 0 \\ 1 & if\ A_v < 0 \end{cases}. \tag{2.16}$$

However, Shokrollahi proposes in [45] a decision after several iterations based on a certainty defined by, (2.17),

$$v = \begin{cases} 0 & if\ A_v \to +\infty \\ 1 & if\ A_v \to -\infty \end{cases}. \tag{2.17}$$

Generally, in the context of LDPC soft decoding, the expression given by (2.16) is applied after a maximum number of iterations to finally decode the values "0" or "1" of the bit nodes.

Min-Sum Algorithm

Although SP algorithm remains the optimum in terms of error performance, the decoding complexity is high. The Min-Sum (MS) or BP-Based [46] algorithm is considered as an approximation of SP in order to reduce the implementation complexity of decoder at

the expense of performance degradation. The approximation of SP for its derivative MS algorithm by altering the expression of messages passed from check nodes to bit nodes as given in (2.14) is described as follows. Using the relationship,

$$2tanh^{-1}(x) = ln\left(\frac{1+x}{1-x}\right), \tag{2.18}$$

the message from check node c to bit node v at round i can be rewritten from (2.14) as,

$$\begin{aligned} m_{cv}^{i} &= 2tanh^{-1}\left(\prod_{v'\in V_c\backslash v} tanh\left(\frac{m_{v'c}^{i-1}}{2}\right)\right) \\ &= 2tanh^{-1}\left(\prod_{v'\in V_c\backslash v} sng\left(m_{v'c}^{i-1}\right) \prod_{v'\in V_c\backslash v} tanh\left(\frac{|m_{v'c}^{i-1}|}{2}\right)\right) \\ &= \prod_{v'\in V_c\backslash v} sng\left(m_{v'c}^{i-1}\right) 2tanh^{-1}\left(\prod_{v'\in V_c\backslash v} tanh\left(\frac{|m_{v'c}^{i-1}|}{2}\right)\right), \end{aligned} \tag{2.19}$$

with $sng\left(m_{v'c}^{i-1}\right)$ the sign of message propagated from the bit node v' to the check node c during the previous iteration $i-1$. As justified in [43], the approximation criterion of SP is due to the fact that the product $\prod_{v'\in V_c\backslash v} tanh\left(\frac{|m_{v'c}^{i-1}|}{2}\right)$ in (2.19) can be maximized for the smallest value of $|m_{v'c}^{i-1}|$. Hence, other name for MS algorithm is "max-product" and the expression m_{cv}^{i} becomes,

$$m_{cv}^{i} = \prod_{v'\in V_c\backslash v} sng\left(m_{v'c}^{i-1}\right)\ min\left\{|m_{v'c}^{i-1}|, v'\in V_c\backslash v\right\}. \tag{2.20}$$

Except the modification of the update of the check nodes in (2.20), which is the particularity of MS, the rest of steps including (2.13) and (2.15) during the iteration remains the same as previously described for the SP algorithm.

Normalized Min-Sum Algorithm

Normalized Min-Sum (NMS) or even *Normalized BP-Based* algorithm is a variant of MS with a slight modification expressed by multiplying the expression of messages passed from the check nodes to the bit nodes in (2.20) by a normalization factor α as given in (2.21), with $0 < \alpha \leq 1$. Otherwise, all the operations are similar with MS algorithm previously described.

$$m_{cv}^{i} = \alpha \prod_{v'\in V_c\backslash v} sng\left(m_{v'c}^{i-1}\right)\ min\left\{|m_{v'c}^{i-1}|, v'\in V_c\backslash v\right\}. \tag{2.21}$$

As all the LDPC decoding algorithms, the goal sought by the authors [50] is to define NMS as an algorithm with low complexity that can achieve error performance closer to the optimum SP. According to the authors, the definition of the normalization factor α is to compensate the difference that can be found between the values of check node update

given by SP algorithm in (2.9) and those defined by MS approach in (2.20) hereby,

$$\alpha = \frac{E\left\{\left|ln\left(\frac{1+\prod_{v'\in V_c\backslash v} tanh\left(\frac{m_{v'c}^{i-1}}{2}\right)}{1-\prod_{v'\in V_c\backslash v} tanh\left(\frac{m_{v'c}^{i-1}}{2}\right)}\right)\right|\right\}}{E\left\{min\left\{|m_{v'c}^{i-1}|, v'\in V_c\backslash v\right\}\right\}}, \tag{2.22}$$

where $m_{v'c}^{i-1}$ is the message passed from the check node v' to the bit node c during the iteration $i-1$, and V_c the set of bit nodes incident to the check node c. Some approximations have been derived for the computation of α from (2.22) in [50] for the first iteration and it is kept for the rest of iterations. Otherwise, as mentioned by authors in [51], the optimum performance is reached for α varying from one iteration to another and really depends on the signal-to-noise ratio (SNR) values [43], i.e for each value of SNR, a new value of α that maximizes the error performance must be selected in experiment way or theoretically. And to be rigorous, performance are become better if the selection of α value is also based on the code length. However, for the sake of simplicity, and in most of the literature, in the context of our study, we choose a single value of α for all iterations and SNR values.

Summary of LDPC Decoding

In the open literature, several LDPC decoding algorithms are proposed, and among these, the most known to achieve the optimum error performance is Belief Propagation (BP) or Sum-Product (SP), but with higher computational complexity. To significantly reduce this complexity, Min-Sum (MS) which is a BP alternative has been proposed with the only and main modification in the expression of messages passed from the check nodes to the bit nodes. Nonetheless, reducing the BP complexity with the MS algorithm degrades decoding performance. It is in this way, modified MS decoding algorithms have been preferred such as Normalized Min-Sum (NMS) which uses additional correction factor to improve error performance.

2.5.4 Conclusion on LDPC Encoding and Decoding

5G NR LDPC codes use quasi-cyclic (QC) structure and they are designed to support multiple expansion or lifting values Z_c. The encoding technique is systematic and based on two photograph-based LDPC (PB-LDPC) code matrices BG1 adapted for large systematic blocks with maximum size $K = 8448$ and high code rate and BG2 used for low code rates and small blocks with maximum size $K = 3840$. For 5G eMBB applications, whether BG1 or BG2, the first two vectors, each of size $2Z_c$ are punctured by default in order to maximize the transmit throughput, and these systematic bits must be restored during the decoding step at the receiver. For the decoding of these 5G LDPC codes in the context of our study, NMS algorithm has been chosen as a tradeoff between BP or SP with optimum error performance, but with a high decoding complexity and MS with low implementation complexity at the expense of decoding performance degradation. The value of normalizing factor α for NMS algorithm depends on the type of application implemented in the communication system and it can change from one simulation to another.

2.6 5G LDPC Codes Rate Matching for DL-SCH

2.6.1 Introduction

In the cellular system communication, as the amount of available physical resources and especially the channel state dynamically vary, several types of modulation and coding scheme (MCS) have been proposed, each with a particular code rate and spectral efficiency for data channel PDSCH. It is in this way, the goal of rate matching block in the communication chain is to dynamically adapt the number of bits on LDPC encoder output to the amount of bits expected for a given MCS, essentially based on the selected code rate. For the DL-SCH transport block, two main stages are processed in the rate matching operation: 1-bit selection (or *rate-matching*) and 2-bit interleaving as given in the following figure.

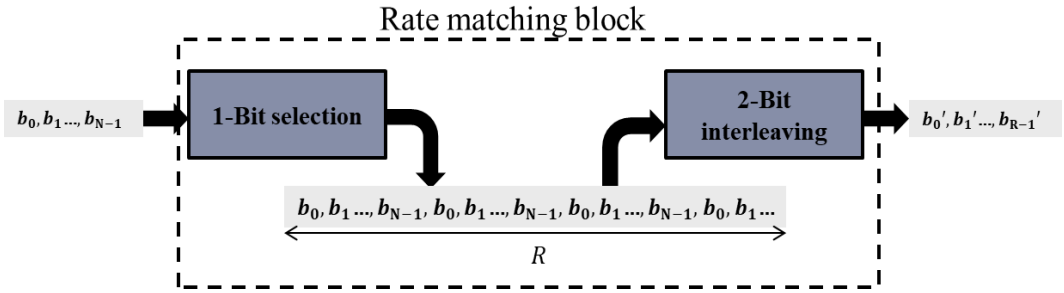

Figure 2.10: Overview of rate matching bloc.

In Fig. 2.10, N is the size of bits after LDPC encoding whose value is $66Z_c$ for LDPC base graph 1 **BG1** and $50Z_c$ for LDPC base graph 2 BG2. R represents the amount of bits required by the MCS chosen for the transmission and defined by $R = \frac{K}{r}$, with K the code block size before LDPC encoding as mentioned in section 2.5.2 and r the code rate given by the selected MCS.

2.6.2 Bit Selection or Rate Matching

Bit selection or even rate matching for 5G NR LDPC codes involves storing bits in a circular buffer of size $N = D_c K_b Z_c$, with $D_c = 3$ for LDPC BG1 and $D_c = 5$ for LDPC BG2 and K_b the number of systematic columns given in Table 2.2. Bits including systematic and parity parts from the LDPC encoding are read by packet of Z_c bits with packet starting index rv (redundancy version) given by higher layers [31], varying from rv_0 to rv_3 as indicated in Table 2.3. When the amount of bits for the transmission is not reached and the bit counter is at the end of the circular buffer, bit reading resumes by the starting packet.

The principle of bits reading for the storage in the buffer is depicted in Fig. 2.11. Parameters rv give an indication to the receiver on the starting position of the received packet in the circular buffer and they have been designed for the hybrid automatic repeat request(HARQ) performance in case of the retransmission mechanism. This study has been conducted by Hamidi-Sepehr and Nimbalker in [55].

In bit selection for 5G LDPC codes, one of the following operations can occurs depending of the code length N and the rate matching output size R.

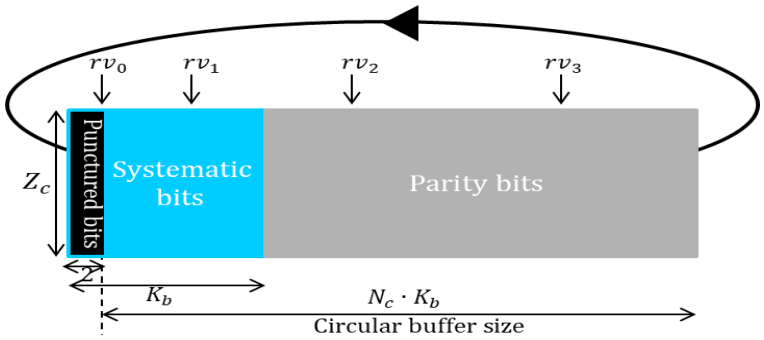

Figure 2.11: Circular buffer and rv positions.

Puncturing: Puncturing is an operation that consists in not transmitting some of bits after LDPC encoding in order to meet the rate matching output size R. This means that the mother code length N is greater than R, consequently $N - R$ bits are punctured. Nonetheless, puncturing can be performed on systematic or parity bits. Regarding the 5G NR PHY communication chain implemented in the Galacsy simulation tool, apart from puncturing of first two systematic packets of size Z_c each [31], the puncturing in the rate matching operation is performed on parity bits. However, if systematic bits are punctured on transmit side, the Rx must restore them.

Repetition: Unlike puncturing, repetition is a bit selection mode for which the rate matching output size R is greater than the mother code length N. To adapt N to R, it is obvious that in repetition the N bits of mother codeword are selected and $R - N$ additional bits are sent on the transmission channel. Clearly, in our communication chain, this mode of bit selection is not considered, but more details are given in [56].

Table 2.3: Redundancy version values [31].

Redundancy version (rv)	LDPC Base matrix 1 BG1	LDPC Base matrix 2 BG2
rv_0	0	0
rv_1	17	13
rv_2	33	25
rv_3	56	43

2.6.3 Bit Interleaving

Bit interleaving is the post-processing of bit selection whose purpose is to avoid burst of errors due to the transmission channel, especially for fading channel models. For the DL-SCH transport block, a row-column interleaving is applied. Bits from the bit selection are arranged as in a matrix by row-wise writing with a number of rows equal to the modulation order (number of bits per modulation symbol) and the number of columns is equal to the amount of complex symbols available for the transmission. The output bits from the bit interleaving are obtained by column-wise reading. An example of this process is shown in Fig. 2.12 for 16QAM as modulation scheme with the number of symbols equal to 4.

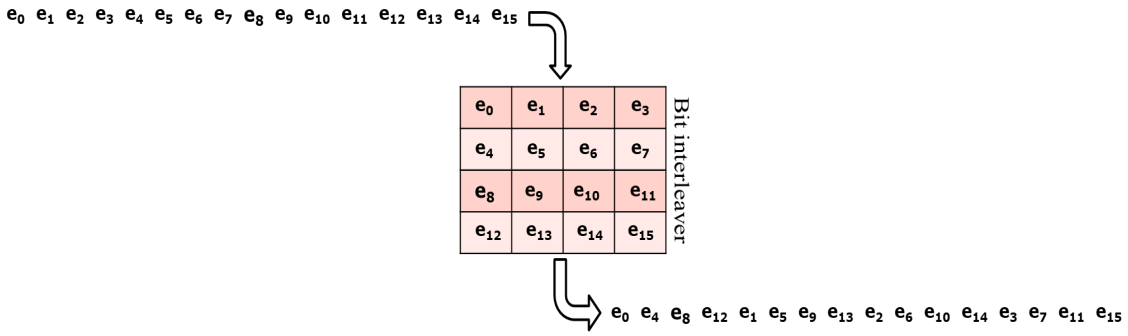

Figure 2.12: DL-SCH bit interleaving.

2.6.4 Summary of Rate Matching

The rate matching for the downlink transport block DL-SCH consists of bit selection and bit interleaving. The bit selection operation also called rate matching enables the Tx to adapt the mother code length from LDPC encoding to the number of bits required for the transmission depending on the channel state and the amount of available physical resources. In addition to this operation as the post-processing, bit interleaving is performed to avoid bursts of errors during the transmission. And finally, for the punctured bits, they are replaced by zeros in the demodulator before LDPC decoding step on the receiver side.

2.7 Scrambling

2.7.1 Definition and Advantages

All the blocks of bits from the LDPC encoding and the rate matching are concatenated to make a single stream which undergoes the scrambling operation. Scrambling or *randomization* is a signal processing technique which is used to distinguish at the reception the codewords from several sources [33]. Indeed, in downlink communication, the scrambling operation makes the UE to separate information received from a BS to another one, or probably in MIMO context, the UE could only decode the codeword sent to it and ignore those sent to others UEs in order to avoid any interference. Other advantage of scrambling is to add randomness to binary data, which ensures the security in the communication between the BS and the UE, especially when the transmitted sequence is only composed of zeros ("0") or ones ("1").

2.7.2 Description

The scrambling operation is fundamentally based on the use of a pseudo-random sequence $\boldsymbol{c(k) = x_1\,(k + K_c) \oplus x_2\,(k + K_c)}$ of length R, where $k = 0, 1, ..., R-1$. $x_1(k)$ and $x_2(k)$ represent two length-31 Gold sequences defined in [32] by,

$$x_1(k+31) = x_1(k+3) \oplus x_1(k), \tag{2.23}$$

and

$$x_2(k+31) = x_2(k+3) \oplus x_2(k+2) \oplus x_2(k+1) \oplus x_2(k), \tag{2.24}$$

, and $K_c = 1600$. In terms of initialization, the sequence x_1 is initialized with $x_1(0) = 1$ and $x_1(k) = 0$ for $k = 1, 2, ..., 30$. The sequence x_2 is initialized so that $C_{init} = \sum_{i=0}^{30} x_2(i) \cdot 2^i$, where $C_{init} = N_{RNTI} \cdot 2^{15} + N_{ID}$, with N_{RNTI} and N_{ID} defined in [32] with more details.

An example of scrambling process is illustrated in Fig. 2.13 in which bits $c_0, c_1, ..., c_{R-1}$ represent the scrambling sequence generated by $c(k)$, $z_0, z_1, ..., z_{R-1}$ are the input bits and $\tilde{z}_0, \tilde{z}_1, ..., \tilde{z}_{R-1}$ is the scrambled sequence available for the modulation.

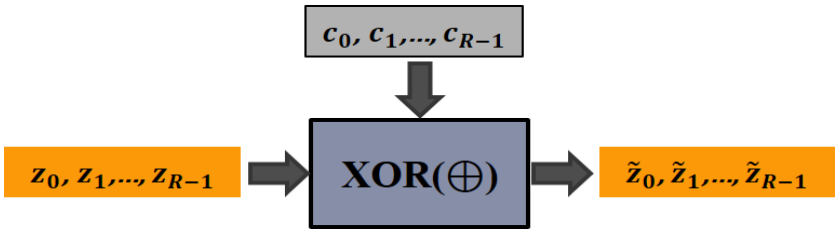

Figure 2.13: Scrambling operation.

2.8 Modulation and Coding Scheme of PDSCH

2.8.1 Modulation Schemes

For the PDSCH channel, four modulation schemes have been defined by the 3GPP consortium in [32] as summarised in Table 2.4. For each given modulation scheme, the

Table 2.4: Modulation schemes for PDSCH [32].

Modulation scheme	Modulation order Q_m
QPSK	2
16QAM	4
64QAM	6
256QAM	8

scrambled bits are grouped into small blocks of Q_m, and to each small block of Q_m bits, a complex value is associated according to a certain strategy of mapping as described as follows.

QPSK

The set of possible symbols that can be generated by using (2.25) in case of QPSK modulation is given Fig. 2.14. For the QPSK modulation, the mapping is based on the use of pair of bits $b(2i)$, $b(2i+1)$ to generate ith complex-value symbol $d(i)$ according to,

$$d(i) = \frac{1}{\sqrt{2}} \left[(1 - 2b(2i)) + j(1 - 2b(2i+1)) \right]. \tag{2.25}$$

16QAM

The mapping in 16QAM modulation is defined from quadruplet of bits $b(4i)$, $b(4i+1)$, $b(4i+2)$ and $b(4i+3)$ to generate ith complex-value symbol $d(i)$ according to,

$$\begin{aligned} d(i) = & \frac{1}{\sqrt{10}} \{(1 - 2b(4i)) [2 - (1 - 2b(4i+2))]\} \\ & + \frac{1}{\sqrt{10}} \{j(1 - 2b(4i+1)) [2 - (1 - 2b(4i+3))]\}, \end{aligned} \tag{2.26}$$

and the constellation representing all plausible symbols is given in Fig. 2.15.

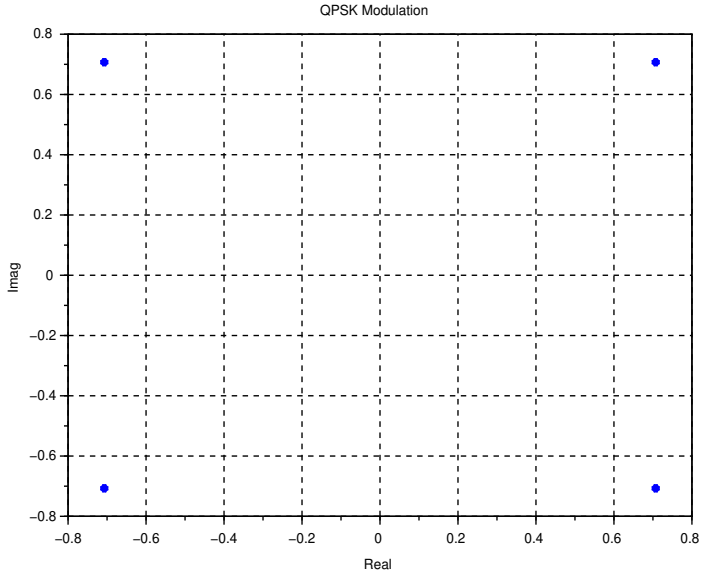

Figure 2.14: QPSK constellation.

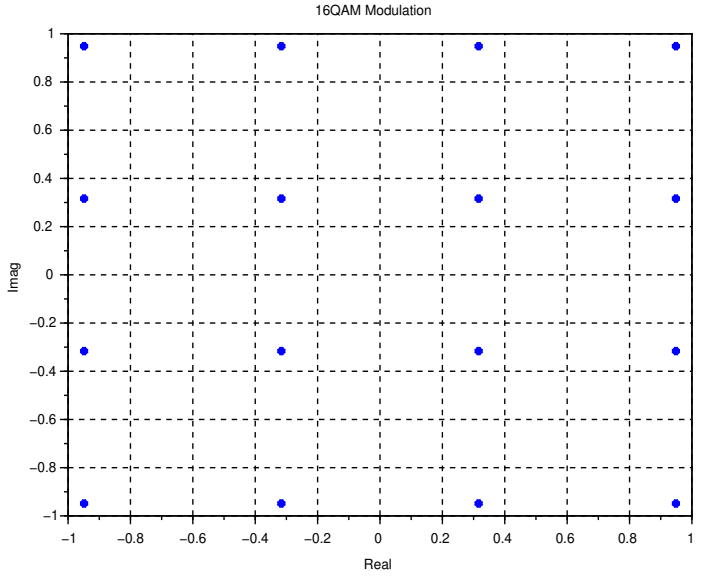

Figure 2.15: 16QAM constellation.

64QAM

In case of 64QAM modulation, the generation of ith complex-value symbol $d(i)$ is defined from sextuplets of bits $b(6i)$, $b(6i+1)$, $b(6i+2)$, $b(6i+3)$, $b(6i+4)$ and $b(6i+5)$ by,

$$d(i) = \frac{1}{\sqrt{42}} \{(1-2b(6i))\,[4-(1-2b(6i+2))\,[2-(1-2b(6i+4))]]\} + \frac{1}{\sqrt{42}} \{(1-2b(6i+1))\,[4-(1-2b(6i+3))\,[2-(1-2b(6i+5))]]\}. \quad (2.27)$$

The set of all symbols of 64QAM modulation is highlighted in Fig. 2.16.

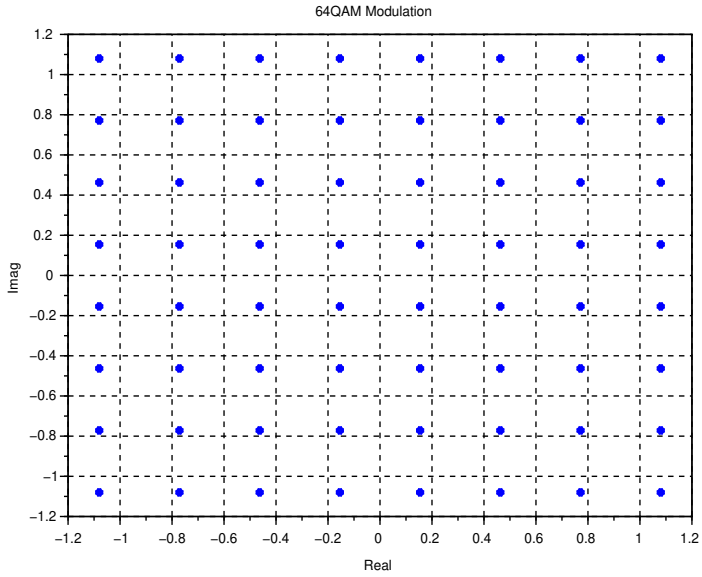

Figure 2.16: 64QAM constellation.

256QAM

The constellation of this modulation scheme is depicted in Fig. 2.17.

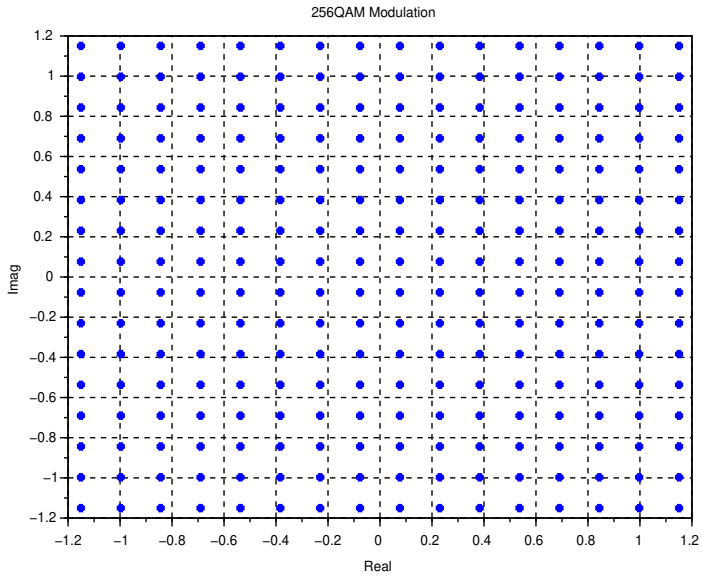

Figure 2.17: 256QAM constellation.

In 256QAM modulation, ith complex-value symbol $d(i)$ is generated by,

$$\begin{aligned} d(i) = \alpha \cdot \{[8 - (1 - 2b(8i+2))\,[4 - (1 - 2b(8i+4))\,[2 - (1 - 2b(8i+6))]]]\} \\ + \beta \cdot \{[8 - (1 - 2b(8i+3))\,[4 - (1 - 2b(8i+5))\,[2 - (1 - 2b(8i+7))]]]\}, \end{aligned} \quad (2.28)$$

using octuplet of bits $b(8i)$, $b(8i+1)$, $b(8i+2)$, $b(8i+3)$, $b(8i+4)$, $b(8i+5)$, $b(8i+6)$ and $b(8i+7)$, with $\alpha = \frac{1}{\sqrt{170}}(1 - 2b(8i))$ and $\beta = \frac{1}{\sqrt{170}}(1 - 2b(8i+1))$.

2.9 OFDM Modulation

This section briefly gives some details on the theory of orthogonal frequency-division multiplexing (OFDM) modulation and its implementation in the simulation tools.

2.9.1 Introduction

OFDM, selected by 3GPP for 5G standard in downlink communication, is a multi-carrier modulation technique whose principle consists in using orthogonal frequencies (subcarriers,or tones), each conveying a part of the information to be transmitted. In fact, the technique is to divide the initial data stream into several parallel substreams modulated each by a subcarrier with a narrowband. In this way, the fast fading channel effect can be combated due to the transmission channel that can be considered flat over each tone. And then, the equalization in this context can simply be performed using a linear method such as zero forcing (ZF) or minimum mean square error (MMSE). In the remainder of this section, a general theory on multi-carrier modulation is given, as well as its particular case OFDM.

2.9.2 Multi-carrier Modulation

The approach of multi-carrier modulation like OFDM is illustrated in Fig. 2.18. The arriving data symbols $\{X_l\}_{l=0,1,2,\cdots}$ are grouped into blocks of N_{SCs} using the serial to parallel converter. The N_{SCs} complex symbols are simultaneously modulated by a filter $g(t)$ of duration T_S, before transmitted over the N_{SCs} subcarrier frequencies $\{f_n\}_{n=-\frac{N_{SCs}}{2},-\frac{N_{SCs}}{2}+1,\cdots,\frac{N_{SCs}}{2}-1}$, respectively. From Fig. 2.18, we notice that by increasing N_{SCs} with the reduction of the subchannel width Δf, the spectral efficiency can be improved by keeping the same signal bandwidth compared to the single carrier modulation.

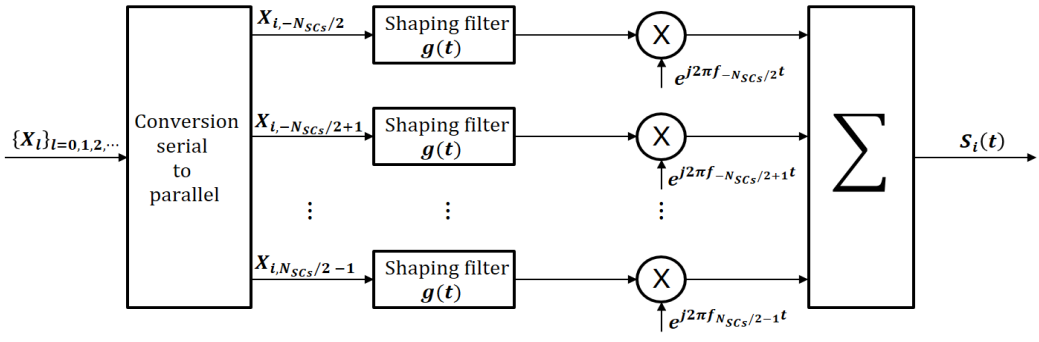

Figure 2.18: Baseband OFDM modulator.

During the transmission delay $[i \cdot T_S, (i+1) \cdot T_S], i = 0, 1, 2, \cdots$ $S_i(t)$ is the i^{th} OFDM symbol generated by the modulator and it is defined hereby,

$$S_i(t) = \sum_{n=-\frac{N_{SCs}}{2}}^{\frac{N_{SCs}}{2}-1} X_{i,n} g\left(t - iT_S - \frac{T_S}{2}\right) e^{j2\pi f_n t}. \tag{2.29}$$

2.9.3 Orthogonality in OFDM

The optimal spectral efficiency cannot be guaranteed with high transmission quality if Δf is very low. In fact, inter-symbol interference (ISI) appears at the Rx if the following conditions are not satisfied [59]:

- In the time domain, subcarriers defined by $\psi_{i,n} = g\left(t - iT_S - \frac{T_S}{2}\right) e^{j2\pi f_n t}$ are not orthogonal.
- In the frequency domain if the spectrum of each subcarrier $\psi_{i,n}$ is not zero at the frequencies of the other subcarriers.

As mentioned in [59], one way to complete both previous orthogonality conditions is to simply define the shaping filter $g(t) = Rect_{[i \cdot T_S, (i+1) \cdot T_S[}(t)$ in subacarrier functions $\psi_{i,n}$. To remember, $Rect_{[a,b[}$ function is defined by,

$$Rect_{[a,b]} = \begin{cases} 1 & if\ t \in [a, b[\\ 0 & if\ otherwise \end{cases}. \tag{2.30}$$

Assuming that the transmitted data symbols $\{X_l\}_{l=0,1,2,\cdots}$ are Gaussian with zero mean and variance σ_X^2, the spectrum of symbol modulated over the subcarrier n is given by,

$$S_n(f) = \frac{\sigma_X^2}{T_S} sinc^2(\pi(f - f_n)). \tag{2.31}$$

From (2.31), it is obvious that the spectrum $S_n(f)$ is zero for frequencies $f = f_n + \frac{k}{T_S}$, $k = \cdots, -2, -1, 1, 2, \cdots$, and the minimum subcarrier spacing can be equal to $\Delta f = \frac{1}{T_S}$ for high spectral efficiency without ISI. The spectrum of these subcarriers are represented in Fig. 2.19.

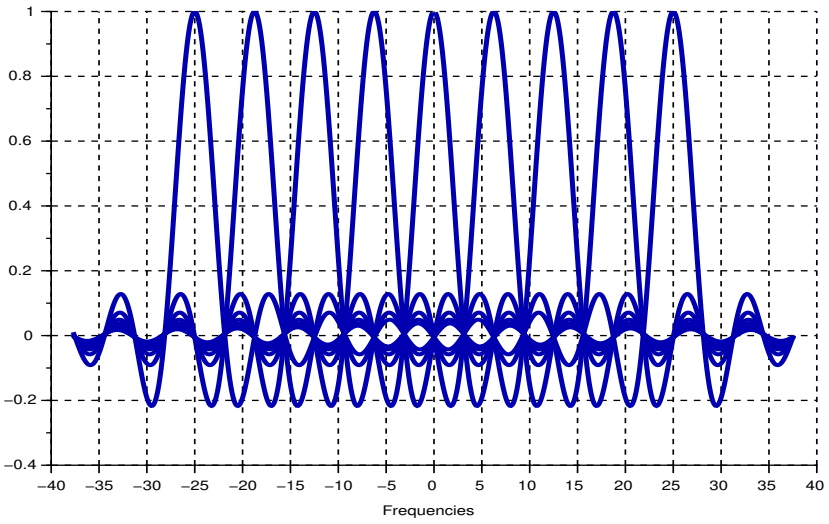

Figure 2.19: Subcarriers in OFDM modulation.

2.9.4 Implementation of OFDM Transceiver

Based on Fig. 2.18, the OFDM transceiver is very complex and costly in terms hardware implementation. A simple and very inexpensive way to implement the OFDM modulation in the simulation tool or a hardware system consists in using the discrete Fourier transform (DFT) and its inverse (IDFT). Considering $f_n = \dfrac{n}{T_S}$, the generation of the ith OFDM symbol during the delay interval $[i \cdot T_S, (i+1) \cdot T_S]$ given in (2.29) can be rewritten through,

$$S_i(t) = \sum_{n=-\frac{N_{SCs}}{2}}^{\frac{N_{SCs}}{2}-1} X_{i,n} e^{j2\pi \frac{nt}{T_S}}. \tag{2.32}$$

As mentioned above, the OFDM symbol includes N_{SCs} samples during the transmission delay T_S, and the discrete signal corresponding to (2.32) is defined by,

$$S_{i,k} = \sum_{n=-\frac{N_{SCs}}{2}}^{\frac{N_{SCs}}{2}-1} X_{i,n} e^{j2\pi \frac{nk}{N_{SCs}}}, \tag{2.33}$$

with $k = -\frac{N_{SCs}}{2}, -\frac{N_{SCs}}{2}+1, \cdots, \frac{N_{SCs}}{2}-1$. From (2.33), we notice that the OFDM symbol represents the IDFT of initial arriving data symbols $\{X_l\}_{l=0,1,2,\cdots}$. In the most common approach, the fast Fourier transform (FFT) is the fast algorithm used for the DFT computation with $N_{SCs} = 2^m$, with $m = 0, 1, 2, \cdots$. Fig. 2.20 summarizes the digital block diagram of the OFDM modulator.

At the Rx, the DFT of received symbols $\{y_l\}_{l=0,1,2,\cdots}$ is computed after a conversion serial to parallel of the stream as given in Fig. 2.21. The sequence of symbols $\{Y_l\}_{l=0,1,2,\cdots}$ corresponds to the initial one $\{X_l\}_{l=0,1,2,\cdots}$ at the Tx. In this context all processing in terms equalization is mainly performed in the frequency domain to restore the transmitted symbols.

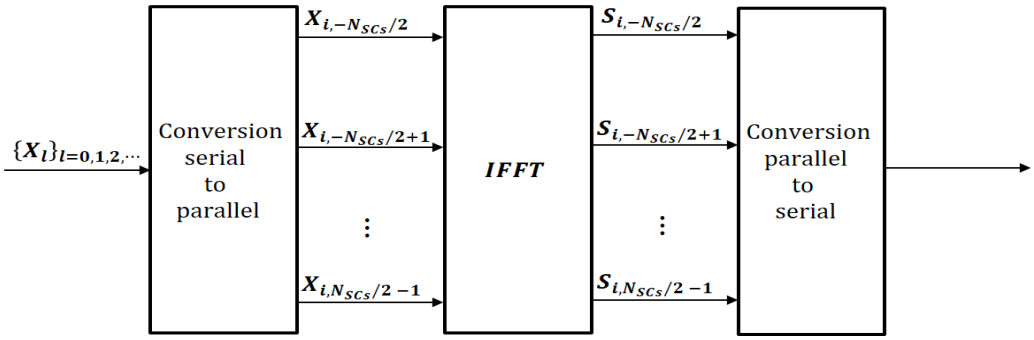

Figure 2.20: Digital OFDM modulator.

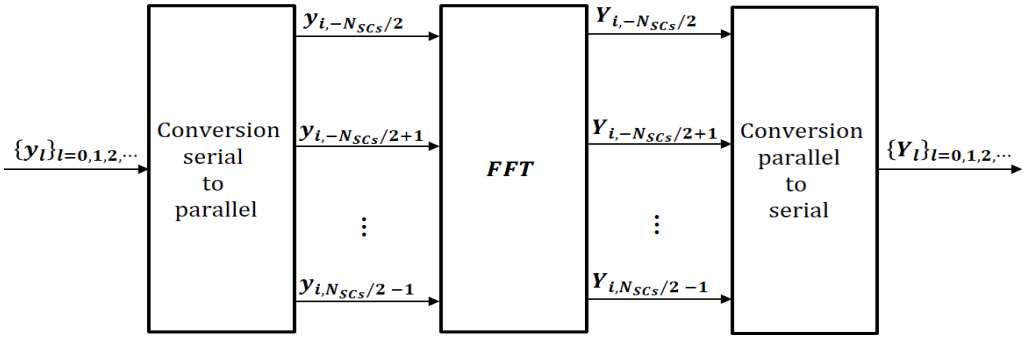

Figure 2.21: Digital OFDM demodulator.

2.9.5 Cyclic Prefix and Guard Interval

In order to protect the quality of the transmission from the ISI, a guard interval (GI) is defined between consecutive OFDM symbols as given in Fig. 2.22. The guard interval time should be equal or longer than the delay spread of the propagation channel to avoid the ISI. In fact, the cyclic prefix (CP) is the way to copy the end of the OFDM symbol

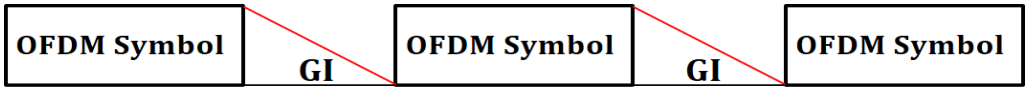

Figure 2.22: Illustration of guard interval.

and insert it at the beginning of the symbol. In other words, the approach of CP is to replace the GI by the end of the OFDM symbol. An illustration is given in Fig. 2.23.

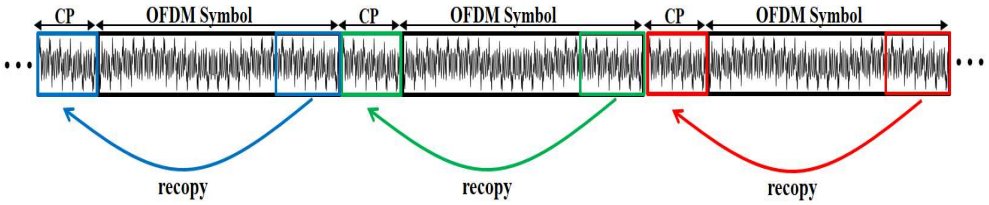

Figure 2.23: Cyclic prefix insertion.

Although the CP insertion avoids the ISI between OFDM symbols, it also introduces the good property of circular convolution in the OFDM system. In fact, the circular convolution in the time domain can be replaced by a simple product in the frequency domain, and processing such as channel estimation and equalization could be simply and linearly performed.

2.10 5G NR Numerology

Numerology basically corresponds to the subcarrier spacing used in the frequency domain in the context of OFDM modulation. Different numerologies are supported by 5G NR, from 15 kHz to 240 kHz. In this way, the subcarrier spacing Δf is defined as follows,

$$\Delta f = 2^{\mu} \times \Delta f_{min}, \tag{2.34}$$

with Δf_{min} =15 kHz and $\mu \in \{0, 1, 2, 3, 4\}$ for synchronization signals and $\mu \in \{0, 1, 2, 3\}$ for other channels. This means that, in the PDSCH channel which is used in the thesis project for data transmission in downlink, the maximum subcarrier spacing is 120 kHz.

Nonetheless, each numerology depends on the carrier frequency to be used in the communication system. In fact, two ranges of frequency are defined for 5G NR technology as given in Table 2.5. Frequency range 1 (FR1) corresponds to sub-6 GHz frequency bands

Table 2.5: 5G NR Frequency ranges [60].

Designation	**Frequency range**
FR1	450 MHz – 6000 MHz
FR2	24250 MHz – 52600 MHz

with a maximum single bandwidth of 100 MHz without aggregation, whereas frequency range 2 (FR2) includes mmWave frequency bands from 24 GHz with a maximum bandwidth of 400 MHz. In Table 2.6, 5G NR numerologies are summarized according to the frequency range and the slot duration, where a slot can be defined as a set of fourteen contiguous OFDM symbols.

Table 2.6: 5G NR Numerology.

Subcarrier spacing (kHz)	**Slot duration (ms)**	**Frequency range**
15	1	FR1
30	0.5	FR1
60	0.25	FR1 and FR2
120	0.125	FR2

2.11 MIMO Technology

MIMO technique consists in exploiting multiple antennas at the Tx, Rx or both in a wireless communication system.

MIMO communication systems are mainly characterized by their transmission channel matrix that has multiple inputs (MI) from Tx antennas and multiple outputs (MO) from Rx antennas as shown in Fig. 2.24, which helps to explain the origin of MIMO expression.

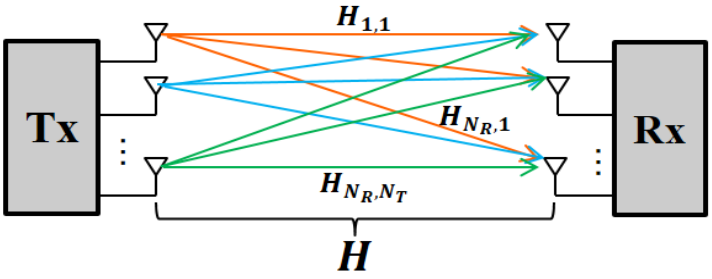

Figure 2.24: MIMO channel illustration

$H = (H_{i,j})_{1 \leq i \leq N_R, 1 \leq j \leq N_T} \in M_{N_R,N_T}(\mathbb{C})$ represents the channel matrix such that $H_{i,j}$ is the channel fading coefficient between the Rx antenna i and the Tx antenna j. N_T and N_R are the number of antennas at the Tx and Rx, respectively.

MIMO channel can be seen as a set of sub-channels between the Tx and the Rx where the sub-channel of fading coefficient $H_{i,j}$ is the transmission channel between the Rx antenna i and the Tx antenna j. The number of sub-channels in a N_TxN_R MIMO system is $m \leq min(N_T, N_R)$, which corresponds to MIMO channel matrix rank. Therefore, the capacity of the channel is the sum of capacities of independent sub-channels that one can distinguish between the Tx and Rx. This means that certain applications of MIMO system, i.e spatial diversity and multiplexing are relevant if the fades $H_{i,j}$ of sub-channels are decorrelated. This decorrelation makes processing like channel estimation and equalization simple at the Rx level for the restitution of symbols simultaneously transmitted.

The advent of such technology has led to the proposal of three main applications defined as follows. The first one is the spatial multiplexing which can be seen as a technique to improve communication data rates. The second application is the diversity technique which is relevant for the reliability of the transmission. And finally, the beamforming approach is defined in order to improve the communication range between the Tx and Rx, and the limitation of interference between users. This latter application is highlighted in Chapter 1. Only a brief description of the first two is given in the remainder of the section.

2.11.1 Spatial Multiplexing

Spatial multiplexing consists of the transmission of multiple data symbols from several spatial layers (or data streams) at the same time and in the same frequency band with the same total power needed for sending only one symbol from one spatial layer. The goal of this MIMO application is to improve spectral efficiency by increasing the transmission rate with the same signal bandwidth, resulting in increased channel capacity.

General Approach

An example for describing the general principle of spatial multiplexing is given in Fig. 2.25 with the transmission of M independent data symbols. In fact, the information is divided into M streams before being transmitted by the antennas. The maximum number of streams that one can transmit corresponds to the MIMO channel matrix rank as previously mentioned.

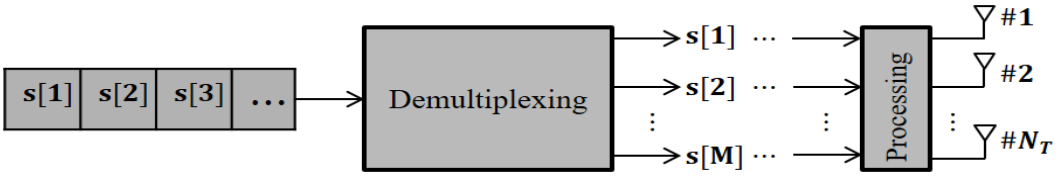

Figure 2.25: Illustration of multiplexing

V-BLAST Architecture

Spatial multiplexing was initially described by Foschini at Bell Labs by spatio-temporal layered architectures. This is why spatial multiplexing is known under the name of BLAST technique (for Bell Labs Layered Space-time). The fundamental approach is to divide the data stream into substreams called "spatial layers", where each layer is mapped to one antenna element.

Indeed, there are several types of BLAST, but here we focused on the V-BLAST architecture (V for "vertical"), since this principle is included in the specification defined by 3GPP for the transmission of the 5G physical layer. In this way, the Tx block-diagram is given in Fig. 2.26 according to [61].

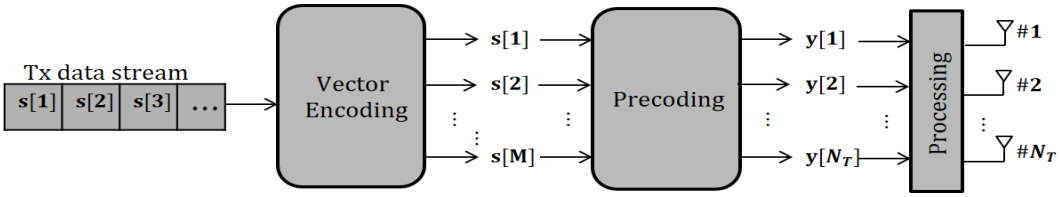

Figure 2.26: The BLAST Tx architecture

The particularity of this architecture, unlike other versions of BLAST, is the fact that vector encoding is a simple demultiplexing operation like the example of Fig. 2.25.

Detection of Symbols

Detection of transmitted symbols at the Rx is more difficult since the data symbol from each Tx antenna element is received by all the Rx antenna elements, which introduces an interference between symbols. Fortunately, there are several signal processing methods for separating the simultaneous transmitted data symbols at as illustrated in Fig. 2.27.

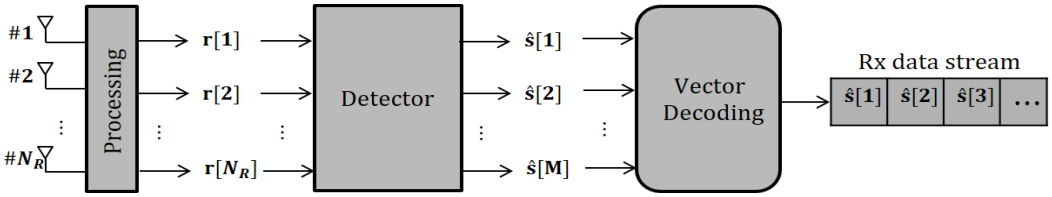

Figure 2.27: The Rx architecture for spatial multiplexing

In fact, the received vector r can be written as $r = Hs + n$, with H the N_RxN_T MIMO channel matrix and $s = (s[1], ..., s[M])^T$ the transmitted vector of symbols by assuming that $M = N_T$. n represents the noise vector of size N_Rx1. Vector decoding is the inverse operation of vector coding described in Fig. 2.26.

Although several techniques have been proposed in the open literature to detect the vector s emitted from the received vector r, we will focus here on the ZF and MMSE receivers since they are used in the communication chain implemented in our Galacsy simulator.

Zero Forcing (ZF) algorithm

The ZF approach is to force the interference between received symbols to zero by means of least square (LS) criterion defined by minimizing the square of error $e = |Hs - r|$. Therefore, the estimated vector symbol $\hat{s}$ from this technique is given through,

$$\begin{aligned} \hat{s} &= \left(H^H H\right)^{-1} H^H r \\ &= s + \left(H^H H\right)^{-1} H^H n. \end{aligned} \tag{2.35}$$

The advantage of this method is its low complexity, which is simpler in terms of implementation. The major downside is the improvement in noise.

Minimum Mean Square Error (MMSE) receiver

The ZF Rx can be improved by using the MMSE criterion whose purpose is to mitigate the noise enhancement. The principle is to find a N_RxN_T matrix C which minimizes $E\left\{||\hat{s} - s||^2\right\}$ where $\hat{s} = C^H r$. This technique results in,

$$\hat{s} = \left(H^H H + \frac{\sigma_n^2}{\sigma_s^2} I\right)^{-1} H^H r, \tag{2.36}$$

with σ_s^2 and σ_n^2 the signal and noise variances, respectively. I is the N_RxN_R identity matrix.

2.11.2 Spatial Diversity

In general, spatial diversity consists of the transmission or reception of the same information on different antennas. Indeed, the independent and decorrelated channel coefficients associated to the same information data are called *diversity branches*.

For example, at the Rx, spatial diversity can be seen as the reception of multiple versions of transmitted signal having undergone decorrelated attenuations. The adapted combination of these observations better detects the transmitted symbols. The main goal behind this technique is to improve the SNR, which results in better transmission quality.

In this context, three main combination techniques are proposed in the literature: *maximum combination ratio (MRC)*, *equal gain combination (EGC)* and *selection combination (SC)*.

2.12 Conclusion

In this chapter, the main processing blocks of the 5G physical communication chain used in the thesis project were described. The communication chain at the Tx and Rx is summarized in Fig. 2.28. The 5G NR numerology for data communication between BS and UE was also described.

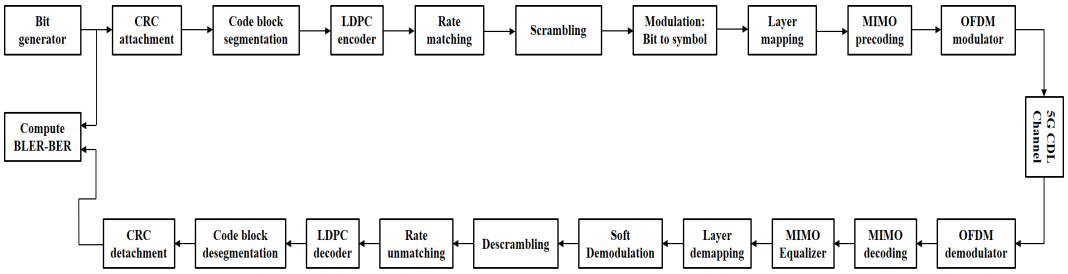

Figure 2.28: 5G PHY communication chain.

The study and the implementation of the transmission blocks rely on the 3GPP specification of release 15. The processing blocks at the Rx level are presented and implemented in the Galacsy C++ tool with reference to the open literature. The transmission performance is evaluated in terms of bit error rate (BER) or block error rate (BLER). However, certain processing blocks in the chain such as the 5G multipath clustered delay line (CDL) channel model are subject of next chapter.

Chapter 3

Millimeter-Wave Channel Modelling in 5G Communication Systems

3.1 Introduction

The propagation channel can be defined as the transmission medium in wireless communication systems. In this way, communication performance is mainly impacted by channel parameters such as frequency and type of propagation environment (indoor or outdoor scenario). Therefore, accurate characterisation and mathematical modelling of radio channel accross a multiple key parameters is indispensable for predicting performance such as signal coverage, achievable throughputs and BER/BLER. It is in this perspective that this chapter deals with certain characteristics of the propagation channel such as pathloss, shadowing, multipath component and atmospheric effects, in particular at mmWave frequencies.

In fact, several channel models are proposed in the literature from some empirical measurements and simulation data in the context of 5G. However, this chapter is fundamentally based on the 3GPP TR 38.901 specification for channel modelling for frequencies from 0.5 to 100 GHz with an emphasis on multipath propagation.

The chapter is organized as follows. In section 3.2, the pathloss and shadowing fading models are briefly reviewed. In section 3.3, more details regarding multipath propagation modelling are given with a state-of-the-art of the various contributing European collaborative projects. Atmospheric phenomena such as oxygen absorption, rain attenuation and foliage penetration are briefly summarized in section 3.4. And finally, section 3.5 concludes the chapter.

3.2 Modelling of Pathloss

Pathloss is one of the channel attenuation characteristics that can naturally be defined as the reduction in the power density of the electromagnetic wave as it propagates through space. In other words, the pathloss represents the signal attenuation caused by free space propagation, reflection, diffraction and scattering. In fact, it constitutes a major component of link budget evaluations in the communication system, and it corresponds to the

average value of signal attenuation.

The pathloss modelling really depends on the propagation environment (indoor or outdoor) and other capital parameters such as the carrier frequency, the height of antennas and the distance between the Tx and the Rx. In the literature, three main categories of pathloss models are proposed: fully empirical models, deterministic models and semi-empirical models. Empirical models are based on measured data and they include Okumura-Hata model, COST-231 Hata model [62]. These models are both simple, but not accurate in the sense that only few parameters are used [63]. Regarding deterministic models such as Ikegami model, a lot of geometry parameters are taken into account, which makes the proposed models more accurate. The models classified as semi-empirical are defined from both empirical data and deterministic aspects. One of the most popular example is the COST-231 Walfisch-Ikegami model [64].

In this section, the aim is to briefly describe the pathloss models proposed by 3GPP according to the propagation scenario, i.e indoor, outdoor and outdoor to indoor (O2I). According to Haneda *et al.* [65], the 3GPP models have been derived based on extensive measurements and ray tracing results. Therefore, the 3GPP pathloss models can be categorized as semi-empirical models extended in 3D.

3.2.1 Indoor and Outdoor Modelling

In most scenarios (indoor and outdoor), the frequency-dependent model is generally used by 3GPP [66] for computing the pathloss in dB units as follows,

$$PL\left(f, d_{3D}\right) = \alpha + 10\beta \log_{10}\left(d_{3D}\right) + 10\gamma \log_{10}\left(f\right) + \chi_{\sigma_{SF}}, \tag{3.1}$$

where f is the carrier frequency in GHz and d_{3D} defines the 3D propagation distance in m. In Fig. 3.1 reproduced from [66], the expression of d_{3D} is naturally given by,

$$d_{3D} = \sqrt{\left(h_{BS} - h_{UE}\right)^2 + d_{2D}^2}, \tag{3.2}$$

with h_{BS} and h_{UE} the BS and UE heights, respectively.

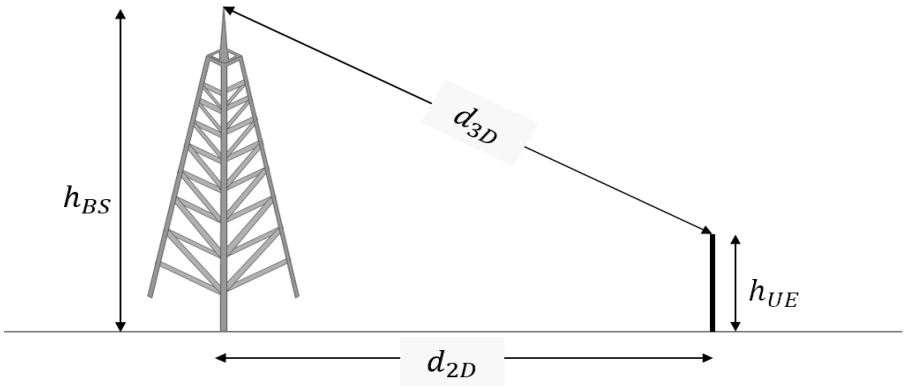

Figure 3.1: Illustration of the distance d_{3D}.

The parameter α is an optimized offset value in dB, β and γ represent slope correction factors to best match the pathloss based on empirical or simulated measurements. These parameters are given in the 3GPP TR 38.901 specification for each propagation scenario.

$\chi_{\sigma_{SF}}$ is the shadowing fading (SF) or slow fading variable following the zero-mean log-normal distribution with standard deviation σ_{SF}. It describes large-scale signal fluctuations [68]. The 3GPP pathloss model given in (3.1) is defined for a minimal horizontal distance $d_{2D_{min}} = 10\,m$ between the Tx and Rx. In addition, it is evident that the higher the frequency or the propagation distance, the higher the attenuation from the pathloss.

Nonetheless, in the modelling of the pathloss for the outdoor scenarios, the double slope is considered as follows,

$$PL_{Dual}\left(f, d_{3D}\right) = \begin{cases} PL_1 & d_{2D_{min}} \leq d_{2D} \leq d_{BP} \\ \\ PL_2 & d_{BP} \leq d_{2D} \leq d_{2D_{max}} \end{cases}, \tag{3.3}$$

with PL_1, the pathloss defined from (3.1) and PL_2 is derived from (3.1) incorporating parameters d_{BP}, h_{BS} and h_{UE}. d_{BP} is called the break point distance and defined by [66],

$$d_{BP} = \frac{4\pi h_{BS} h_{UE} f}{c}, \tag{3.4}$$

where c is the speed of light. This is common to the double slope model due to the reflection on the ground.

3.2.2 Outdoor to Indoor Modelling

The general expression of the pathloss model for the O2I scenario is described by [66],

$$PL = PL_{out} + PL_{tw} + PL_{in} + \mathcal{N}\left(0, \sigma^2_{PL}\right), \tag{3.5}$$

where PL_{out} represents the outdoor pathloss as previously described by replacing d_{3D} by $d_{3D-out} + d_{3D-in}$ illustrated in Fig. 3.2 reproduced from [66].

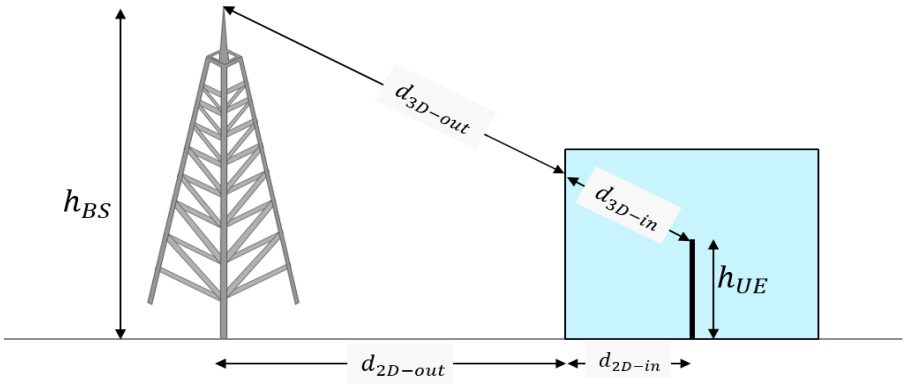

Figure 3.2: Illustration of d_{3D-out}, d_{3D-in}.

PL_{tw} is the building penetration loss through the external wall and depends on the material loss as given by [66],

$$PL_{tw} = PL_{al} - 10\log_{10}\left(\sum_{i=1}^{N_{materials}} p_i \times 10^{\frac{L_{material_i}}{10}}\right), \tag{3.6}$$

with PL_{al} an additional loss due to non-perpendicular incidence. p_i represents the proportion of i-th material so that $\sum_{i=1}^{N_{materials}} p_i = 1$, where $N_{materials}$ is the number of materials

Table 3.1: Material loss models [66]

Material	Penetration Loss (dB)
Standard multi-pane glass	$2 + 0.2f$
Infrared reflective glass	$23 + 0.3f$
Concrete	$5 + 4f$
Wood	$4.85 + 0.12f$

in the wall. $L_{material_i}$ is the loss of material i which depends on the frequency. The loss models for some materials are summarized in Table 3.1 with f in GHz. Regarding PL_{in}, it defines the inside loss whose expression is given through [66],

$$PL_{in} = 0.5d_{2D-in}. \tag{3.7}$$

and σ_{PL} is the standard deviation for the penetration loss.

3.3 Multipath Propagation Channel

Multipath propagation or fast fading is a kind of attenuation due to the destructive or constructive overlay of several delayed versions of the transmitted signal at the Rx. The signal attenuation in this context is not deterministic. In other words, unlike pathloss, no forecast can be performed in terms of signal attenuation.

3.3.1 Geometry-based Channel Models

Since the third-generation (3G), as well as the 4G, smart antenna systems have become a key technology in wireless communication systems [69]. In order to improve the signal quality at reception, smart antennas represent adaptive antenna arrays or switched beam antennas designed to exploit spatial features such as beamforming, for which the directions of departure and arrival of propagation paths have to be identified. The need for geometry-based channel models that include directions of departure and arrival of the signal are required for performance evaluation of such systems.

Introduction to Cluster-based Channel Models

Basically, the electromagnetic wave is scattered by objects in the propagation environment, and multiple copies of the transmitted signal are created. These copies arrive at the Rx with different gains and different delays. However, in some cases, it is observed that the signal copies arrive in cluster with similar delay [70]. Several investigations have been carried out in order to propose channel models to deal with this situation. The first well-known cluster-based channel model is the Saleh-Valenzuela (SV) model [71] in indoor propagation environment, which describes the channel as a set of clusters. A cluster consists of a certain number of rays or sub-paths with similar features.

The SV channel impulse response (CIR) is mathematically given by,

$$h(\tau) = \sum_{n=1}^{N} \sum_{m=1}^{L} a_{n,m} e^{j\phi_{n,m}} \delta(\tau - \tau_n - \tau_{n,m}), \tag{3.8}$$

with τ_n the cluster arrival time. $\tau_{n,m}$, $a_{n,m}$ and $\phi_{n,m}$ represent the arrival time, gain and phase of the m-th multipath component (MPC) in cluster n, respectively. N is the number of clusters and M the number of MPCs or rays in cluster n.

In the SV approach, the power delay profile (PDP) of clusters is modelled with an exponentially decaying profile as defined by,

$$\overline{|a_{n,m}|^2} = \overline{|a_{1,1}|^2} e^{-\tau_n/\Gamma} e^{-\tau_{n,m}/\gamma}, \tag{3.9}$$

where $\overline{|a_{1,1}|^2}$ is the average power gain of the first MPC in the first cluster, Γ and γ are power-delay time constants for the clusters and the rays, respectively. An illustration of such a trend is given in Fig. 3.3.

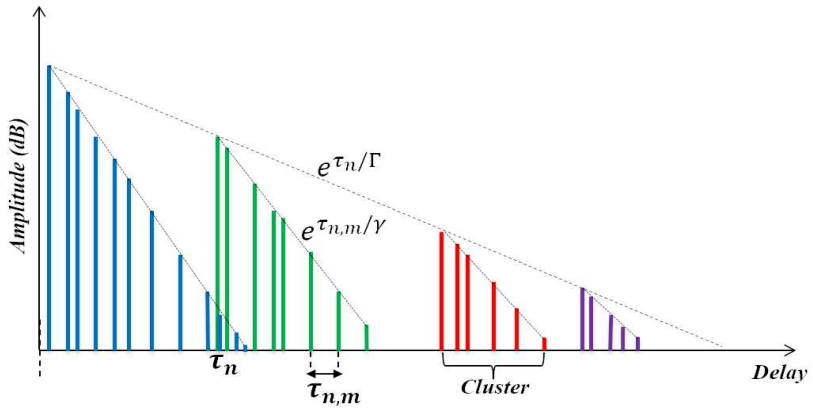

Figure 3.3: Illustration of Saleh-Valenzuela model

The delays τ_n and $\tau_{n,m}$ in the SV approach are modelled with Poisson arrival-time process defined as follows through probability density functions,

$$\rho\left(\tau_n - \tau_{n-1}\right) = \Lambda e^{-\Lambda(\tau_n - \tau_{n-1})}, \tag{3.10}$$

$$\rho\left(\tau_{n,m} - \tau_{n,m-1}\right) = \lambda e^{-\lambda(\tau_{n,m} - \tau_{n,m-1})}, \tag{3.11}$$

where Λ and λ represent Poisson arrival rate of clusters and MPCs, respectively.

Directional Channel Modelling

The principle of clustering, along with geometric descriptions, such as directional information, form the fundamental basis of geometry-based channel models. Several suggestions for directional channel models have been proposed. The common solution in this context is to associate to each cluster or path an average direction and an angular spread [72]. For the indoor propagation environment, the Saleh-Valenzuela channel model is generalized to include consideration of directions of arrival angles [69]-[73]. Nonetheless, the classic channel models characterized by several taps can be extended to the directional channel models. In this context, the ITU-R channel model [74] which presents a tapped delay line aspect is used by Buehrer *et al.* [75] to propose a spatial extension based on measurement results for outdoor environments. The COST-207 channel model has been generalized by Kim and Chung [76] with the inclusion of angle of arrival characteristics. In [77], an analytical expression of the distribution of the MPC angle of arrivals model is proposed from the measurement results in urban and rural macro-cellular environments.

3.3.2 Review of Earlier Channel Models

In this section, a state-of-the-art of earlier common channel models developed and intended for 3G and 4G systems that include directional characteristics is given. The limitations of these models regarding the 5G requirements are also mentioned. To cope with these shortcomings, a review of investigations conducted in European collaborative projects is performed.

3GPP Spatial Channel Model

The 3GPP spatial channel model (SCM) [78] was earlier introduced in 2003 in the mobile channel modelling as a set of propagation paths with angles of departure, angles of arrival, and propagation delays. The 3GPP SCM can be viewed as a geometric two-dimensional (2D) channel model with departure and arrival angles defined in the azimuth plane, based on the clustering principle of rays or sub-paths. Only 6 clusters are defined in each scenario where each cluster is made up of 20 rays. The proposed model only covers propagation scenarios such as suburban macro-cell (SMa), urban macro-cell (UMa) and urban micro-cell (UMi) for the 2 GHz frequency band with a maximum channel bandwidth of 5 MHz compared.

However, in order to improve the proposed channel model, an extension was proposed in 2005, which refers to SCM-extended (SCM-E) [79]. This improvement is justified by the increase in the channel bandwidth, up to 100 MHz and also supports the 5 GHz frequency band.

WINNER Channel Model

The Wireless World Initiative New Radio (WINNER) is an European project initiated by a consortium of forty-one partners in order to enhance the performance of mobile communication systems. More specifically, the objective of WINNER project was initially to develop a unique channel model that include diverse propagation scenarios. It is in this perspective that in WINNER I initiated in 2005 [80].

In fact, WINNER I proposed two approaches for the generation of CIR based on measurements performed using the same frequency components of 3GPP SCM-E. A generic approach that follows geometric based stochastic channel modelling (GSCM) and can be used as a basis for all scenarios in the context of system simulations, and clustered delay line (CDL) approach used for link level simulations for calibration and comparison purposes.

In 2007, WINNER II channel model [81] was developed, which is based on the pursuit of the studies initiated in WINNER I. Compared to the last one, the improvements are twofold. On the one hand, other scenarios are added, namely indoor-to-outdoor (I2O), O2I, large indoor hall, bad UMi which is the same as UMi, but with long propagation delays. On the other hand, the frequency bands were extended from 2 to 6 GHz with the same channel bandwidth of 100 MHz.

In fact, in 2010, WINNER II channel models have been updated to WINNER+ models [82]. Based on WINNER II, the WINNER+ channel models were extended to three-dimensional (3D) where in multipath propagation, rays are also characterized by elevation

angles of departure and angles of arrival. In addition, the frequency range of the channel models was extended up to 450 MHz.

COST Channel Models

The Cooperation in Science and Technology (COST) is a European funding organisation of thirty-eight members whose goal is to reinforce the scientific and technology research in Europe. Several models of COST channel with directional characteristics have been released, from COST-259 to COST-2100.

The COST-259 channel model [69]-[83] released in 2006, is the generalization of the well-known non directional COST-207 channel used in Global System for Mobile (GSM) communication standard. In the development of COST-259, the double-directional CIR characterized by elevation and azimuth angles of clusters was already included. The frequency band extends up to 2 GHz with a maximum bandwidth of 5 MHz.

In the view to cover a large number of scenarios, the COST-259 has been updated to COST-273 [84]. Other invention with COST-273 is the fact that three types of scatterers (or interacting objects) called *local cluster*, *single-interaction cluster* and *multiple-interaction cluster* are used in order to accurately model the radio mobile channel. More details are given in [85]-[86].

In 2012, an extension of COST-273 called COST-2100 [87] was developed to cover MIMO systems, including other communication techniques such as multi-user aspect unlike WINNER model.

IEEE 802.11ad Channel Model

The Institute of Electrical and Electronics Engineers (IEEE) 802.11 is a committee in charge of defining technologies and protocols for Wireless Local Area Network (WLAN) systems. The IEEE 802.11ad represents the WLAN standard that uses the unlicensed 60 GHz mmWave band with data throughput speeds of up to 8 Gbps with low latency.

The IEEE 802.11ad channel model [89] is only defined for indoor propagation environments, especially the conference, cubicle and living rooms. The proposed channel model is based on the 3D clustering approach with departure and arrival angles defined in elevation and azimuth. The characteristics of the IEEE channel model are specifically deterministic and specific for each scenario. This can constitute a limitation of the proposed model.

Limitations of Earlier Channel Models regarding 5G

A summary of these earlier channel models is proposed in Table 3.2 depending on frequency and bandwidth. Channel models like 3GPP proposals, WINNER and COST models were developed with the consideration of directional characteristics in order to simulate realistic radio channel models for 3G and 4G communication systems. However, these models as well as the IEEE 802.11ad have some limitations regarding 5G requirements.

Actually, COST Channel models and WINNER models which are fundamentally based on 3GPP SCM proposals, were developed for frequency bands below 6 GHz.

Table 3.2: Summary of earlier channel models.

References	Model Type	Frequency	Bandwidth
3GPP SCM [78]	Stochastic	2 GHz	5 MHz
3GPP SCM-E [79]	Stochastic	2, 5 GHz	100 MHz
WINNER I [80]	Quasi-deterministic, Stochastic	2, 5 GHz	100 MHz
WINNER II [81]	Quasi-deterministic, Stochastic	From 2 to 6 GHz	100 MHz
WINNER+ [82]	Quasi-deterministic, Stochastic	From 0.45 to 6 GHz	100 MHz
COST-259 [69]-[83]	Deterministic, Stochastic	2 GHz	5 MHz
IEEE 802.11ad [89]	Deterministic	60 GHz	Up to 2.16 GHz

Consequently, they cannot be applied to frequencies extended to mmWave bands, which represent one of the key technologies of 5G systems. Other 5G channel characteristics such dual-mobility required for device-to-device (D2D) link and spatial consistency are not supported by COST and WINNER developed models. In fact, spatial consistency can be considered as a slight evolution of the channel parameters due to the motion of the user. Parameters such as angles and propagation delays of clusters should be updated in this case.

Regarding the IEEE 802.11ad channel model, due to the deterministic aspect of the channel parameters depending on the given scenario, the model is poorly suited for hosting 5G requirements. Additionally, the model is only focused on the 60 GHz band, i.e other mmWave frequencies cannot be used.

3.3.3 State-of-the-Art of 5G Channel Models

The channel model on the 5G horizon should be generic and flexible, including some key requirements such as a large number of propagation scenarios, the use of mMIMO technology, and a wide frequency range up to mmWave bands with huge amount of bandwidth. In this context with a focus on mmWave technology, channel characteristics such as blockage and atmospheric components should be taken into account.

In order to develop a suitable channel model regarding the 5G use cases, studies and experiments have been carried out through several international and European collaborative projects, the best known of which are METIS, MiWEBA and mmMAGIC. In this section of the chapter, some details of the channel models developed as a result of these projects are given.

METIS Channel Model

Mobile and wireless communications Enablers for the Twenty-twenty Information Society (METIS) is a European project started by approximately thirty members in 2012 including manufacturers, operators, academics, automotive industries and research centers. The general objective of the project was to propose a solid foundation of 5G.

In this way, the METIS channel model [18] was developed to cope with the shortcomings of the earlier channel models. More specifically, the channel model was proposed including mmWave frequencies up to 100 GHz, with a bandwidth greater than 500 MHz.

The METIS project resulted in the proposal of the three channel models which are a map-based model, a stochastic model and a hybrid model. The map-based model can be seen as the IEEE 802.11ad channel model, which is deterministically defining the realistic

and accurate parameters of the 3D propagation environment based on ray-tracing simulations. Significant propagation mechanisms such as diffraction, reflection and scattering are taken into account.

Furthermore, the METIS stochastic model is the extension of the WINNER GSCM models for frequency bands up to 70 GHz. Unlike the map-model, based on the measurement results, all the propagation parameters of this channel model are stochastically determined from statistical distributions.

And finally, the hybrid channel model is a combination of the deterministic map-model and the stochastic model. In other words, the hybrid approach is the stochastic model with the pathloss and shadowing parameters obtained from the map-model. The model is also applicable for frequencies up to 70 GHz. As the map-based model is more complete than the stochastic model, but more complex, the hybrid solution can be considered as a good trade-off.

MiWEBA Channel Model

Millimeter–Wave Evolution for Backhaul and Access (MiWEBA) was a project launched in 2013 by the European commission and some Japanese partners. The goal was focused on the use of mmWave technology in order to meet the spectrum and capacity requirements of cellular networks that are limited with the increase of data traffic.

As a result of the MiWEBA project, a quasi-deterministic 3D channel model was developed at 60 GHz for outdoor and indoor environments with a bandwidth around 800 MHz, based on ray-tracing simulations [19]. It includes characteristics such as spatial consistency, dual mobility for D2D communication, and supports a large number of antennas. In the proposed channel model, backhaul wireless link was included in addition to radio access and D2D links.

In fact, the quasi-deterministic approach consists of modelling the mmWave channel model impulse response with a few quasi-deterministic strong rays and a number of weak random rays. The strong quasi-deterministic rays are propagation clusters defined according to the parameters and the geometry of the given scenario. However, weak random rays represent lower power clusters, and are generated stochastically according to statistical distributions.

mmMAGIC channel Model

mmWave based Mobile Radio Access Network for 5G Integrated Communications (mmMAGIC) is a project launched in 2015 whose specific goal was the development of channel models in the frequency range from 6 to 100 GHz with a maximum bandwidth of 2 GHz, that can be used for 5G communications. The proposed mmMAGIC channel model [17] includes deployment scenarios such as UMi street canyon and open square, indoor office (inH), indoor shopping mall and airport, O2I, stadium and metro station with very high user densities.

Similar channel characteristics as METIS and MiWEBA models are supported, with the addition of novelties such as blockage effect modelling due to pedestrians or vehicles, mMIMO with narrow beams, incorporation of O2I penetration losses. Based on a plethora

of channel measurement campaigns and ray-tracing simulations, a GSCM channel model was proposed.

The proposed mmMAGIC channel model has been developed in parallel with the latest 3GPP and ITU-R models. Consequently, there have been active contributions from mmMAGIC project to these standards.

3GPP 3D Channel Model

The development of a 3D channel model by 3GPP from WINNER models has been initiated in 2014 for 4G LTE communication systems. Since 2016, an extension of the model [66] was developed from the contributions of partners, which covers mmWave frequencies up to 100 GHz. The channel model supports large bandwidth, up to 10% of carrier frequency, but no larger than 2 GHz. mmWave propagation aspects such as blockage phenomenon and atmosphere (oxygen) attenuation are also taken into account as additional channel components. The mobility of the user has been extended to 500 km/h, especially in V2V communication context.

In general, and similar to METIS model, a hybrid channel model is proposed which is characterized by the fact that pathloss and shadowing parameters are given depending on the propagation scenario, and the fast fading is based on GSCM channel model. Nonetheless, the WINNER CDL approach is also adopted in the CIR generation.

Other Non-Collaborative Channel Models

QuaDRiGa Channel Model:

Quasi Deterministic Radio channel Generator (QuaDRiGa) [90] is the extension of WINNER channel model with the incorporation of new channel features such as time evolution in order to make it more realistic and accurate. The QuaDRiGa channel model was developed by Fraunhofer HHI in 2014 and it includes a collection of 3GPP SCM and WINNER channel features. The proposed model is constantly updated and the compatibility with the mmMAGIC channel model and the recent 3GPP is ensured. Consequently, the QuaDRiGa channel model can be used for mmWave frequency bands up to 100 GHz with 2 GHz of channel bandwidth. The model also takes into account the satellite channel model which includes parabolic multibeam antenna (MBA).

NYU Wireless Research Center 3D SSCM Model:

A 3D statistical spatial channel model (SSCM) [91] for mmWave communication has been proposed by the New York University (NYU) wireless research center based on measurement campaigns carried out at 28, 38, 60 and 73 GHz in outdoor and indoor propagation environments. As mentioned in [5], the proposed channel model is the extension to mmWave frequency bands of 3GPP 3D model [92] developed for LTE systems. The SSCM model can be used for both omnidirectional and directional antennas. mmWave channel feature like blockage effect is included with propagation scenarios such as V2V, backhaul and access link.

Summary of Channel Models

A summary of different 5G multipath channel models is given in Table 3.3.

Table 3.3: Summary of 5G multipath channel models.

References	Model Type	Frequency	Bandwidth
METIS [18]	Deterministic, Stochastic, Hybrid	Up to 100 GHz	500 MHz
MiWEBA [19]	Quasi-deterministic	60 GHz	800 MHz
mmMAGIC [17]	Deterministic, Stochastic, Hybrid	From 6 to 100 GHz	2 GHz
QuaDRiGa [90]	Quasi-deterministic	Up to 100 GHz	2 GHz
NYU SSCM [91]	Deterministic	28, 38, 60, 73 GHz	800 MHz and 1.5 GHz
3GPP [66]	Quasi-deterministic, Stochastic	From 0.5 to 100 GHz	Up to 2 GHz

Since the 3GPP model is used for simulation purposes, a description of the model, in particular for the CIR generation, is given in the following section.

3.3.4 Focus on 3GPP 5G Modelling of Multipath Channel

For the generation of the channel coefficients, two models have been proposed by 3GPP in [66]: the *generic* or *fully stochastically* model and the *CDL-based* model.

According to the first model, all the propagation channel parameters such as delay spread, angular spread, Rice factor (in LOS), cluster delays, clusters powers, angles of arrival and departure of each cluster and cross-polarization power ratio (XPR) are stochastically generated from statistical distributions. In fact, as defined in [67], XPR represents the ratio of pathloss without polarization change to pathloss when the wave is received with orthogonal polarization.

Regarding the CDL-based model, it can be seen as a quasi-deterministic method. In this context, the previously mentioned channel parameters are given in CDL tables. Only the ray angles inside the cluster are randomly coupled. As mentioned before, the CDL-based model is convenient for link level simulations which consists in using a single point-to-point link between a single BS and a single UE unlike system level simulation where multiple UEs with multiple links are used.

In fact, five different CDL profiles are proposed by 3GPP. Three profiles for NLOS state propagation which are CDL-A, CDL-B, and CDL-C. And for the environment in LOS state, two profiles CDL-D and CDL-E are used. The purpose of this section is to describe the procedure for generating channel coefficients from CDL profiles depending on the LOS or NLOS channel state.

Coordinate System and Conventions

In the definition of coordinate system, the Cartesian approach given by x, y, z axes, the spherical angles θ and ϕ, and the spherical unit vector $\hat{n}$ are used as illustrated in Fig. 3.4 reproduced from [66]. θ and ϕ represent the elevation and azimuth angles in the Cartesian coordinate system, respectively. From Fig. 3.4, it can be noted that $\theta = 0$ points towards the zenith and $\theta = 90^\circ$ points to the horizon.

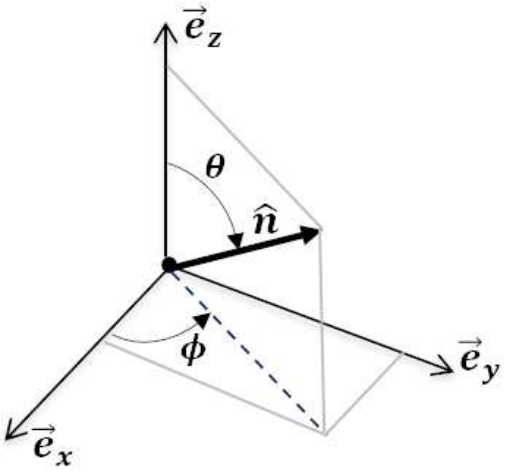

Figure 3.4: Illustration of coordinate system.

In terms of the convention defined by 3GPP for channel modeling, two types of coordinate system are defined, the global coordinate system (GCS) and the local coordinate system (LCS). The GCS is the coordinate system comprising several BSs and UEs; while an LCS is the coordinate system used depending on the orientation of the local antenna panel. It only locally defines the coordinate system for BS or UE, not for all BSs and UEs. An illustration of both coordinate systems is highlighted in Fig. 3.5 where the GCS is defined by (x, y, z) and the LCS is defined by (x', y', z') with the antenna panel given in the (y', z') plan for both BS and UE.

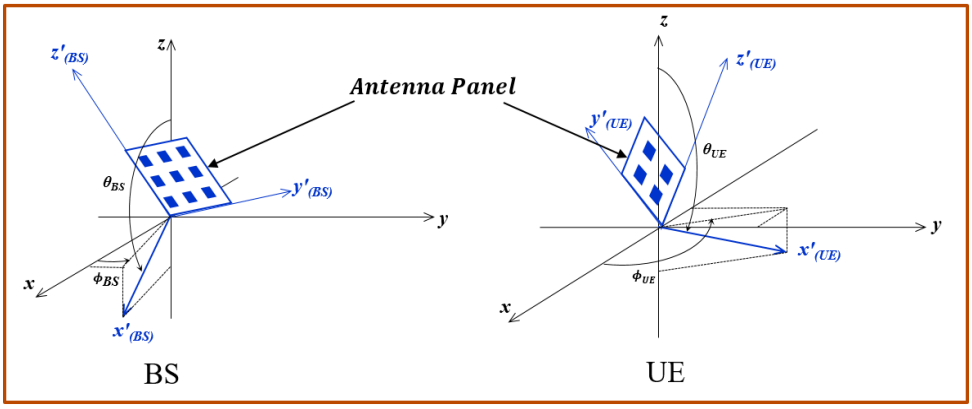

Figure 3.5: Illustration of GCS and LCS

The couples (θ_{BS}, ϕ_{BS}) and (θ_{UE}, ϕ_{UE}) define the BS and UE orientations, respectively. Nonetheless, a transformation from a LCS to a GCS exists from downtilt angles θ_{BS}, θ_{UE} and bearing angles ϕ_{BS}, ϕ_{UE}. More details on the transformation are given in [66].

CDL Channel Profile

The multipath propagation between the Tx and Rx according to the cluster approach is illustrated in Fig. 3.6. Parameters $\theta_{n,m,ZoD}$, $\theta_{n,m,ZoA}$, $\phi_{n,m,ZoD}$ and $\phi_{n,m,ZoA}$ represent the elevation (or zenith) angle of departure, the elevation angle of arrival, the azimuth angle of departure and the azimuth angle of arrival, respectively, for the ray m of cluster

n in the GCS with the BS as the Tx and the UE as the Rx. Each cluster is composed of a total number of 20 rays.

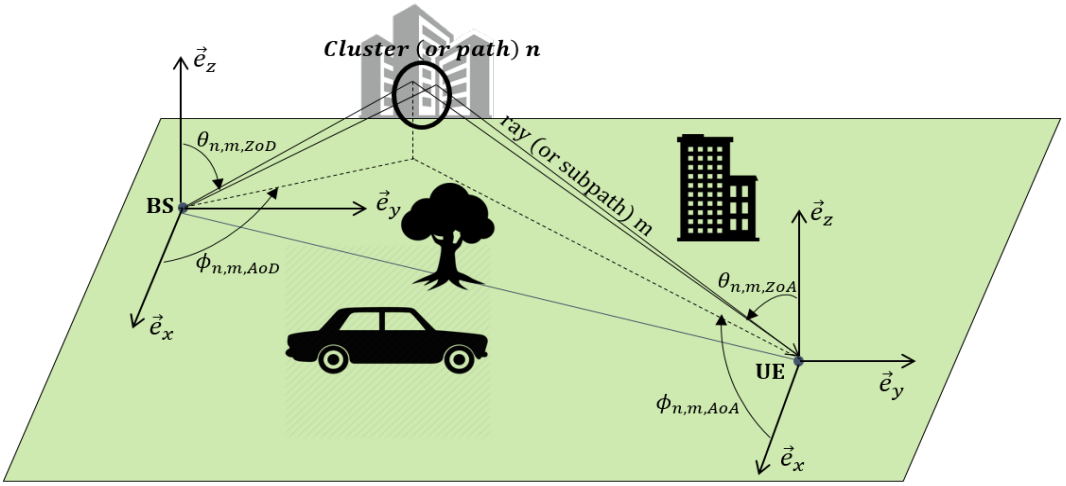

Figure 3.6: Illustration of cluster propagation.

As mentioned earlier, five channel profiles are constructed to cope with all propagation scenarios defined for the link level assessment. In this study, the description of CDL profiles is only focused on the CDL-C model for NLOS channel profile and CDL-E for LOS channel state due to the use of these models in the simulations performed during the thesis project.

The CDL-C channel parameters are given in Table 3.4 where $\phi_{n,AoD}$, $\phi_{n,AoA}$, $\theta_{n,ZoD}$ and $\theta_{n,ZoA}$ represent the azimuth angle of departure (AoD), the azimuth angle of arrival (AoA), the zenith angle of departure (ZoD), the elevation angle of arrival (ZoA), respectively, for the cluster n. $\phi_{n,AoD}$ and $\phi_{n,AoA}$ are modelled by Gaussian distribution while $\theta_{n,ZoD}$ and $\theta_{n,ZoA}$ are modelled by Laplacian Gaussian. For the channel coefficients generation, other parameters are needed for the ray angles calculation. These parameters are summarized in Table 3.5 and are common to all clusters. Parameters C_{ASD}, C_{ASA}, C_{ZSD} and C_{ZSA} stand for cluster azimuth spread of departure angle, cluster azimuth spread of arrival angle, cluster zenith spread of departure angle and cluster zenith spread of arrival angle, respectively.

As for CDL-C model, the same parameters are used with CDL-E model for LOS channel state. The channel configuration parameters are summarized in Table 3.6. The main difference with the NLOS model is the fact that there is a direct (LOS) path between the Tx and the Rx which has the same delay with the first NLOS path and its power is the maximum.

Parameters C_{ASD}, C_{ASA}, C_{ZSD} and C_{ZSA} are also used in the CDL-E model with other values. As the fading channel model follows the Rice distribution, the definition of the Rice parameter K_R is required as given in dB units by [66],

$$K_R = P_1^{LOS} - 10\log_{10}\left(\sum_{n=1}^{N} 10^{\frac{P_n}{10}}\right), \tag{3.12}$$

Table 3.4: CDL-C Table [66].

Cluster n	**Normalized Delay** $\tau_{n,model}$	**Relative Power (dB)** P_n	**AoD (°)** $\phi_{n,AoD}$	**AoA (°)** $\phi_{n,AoA}$	**ZoD (°)** $\theta_{n,ZoD}$	**ZoA (°)** $\theta_{n,ZoA}$
1	0.0000	−4.4	−46.6	−101	97.2	87.6
2	0.2099	−1.2	−22.8	120	98.6	72.1
3	0.2176	−2.5	−40.7	−127.5	100.6	70.1
4	0.2219	−3.5	−22.8	120	98.6	72.1
5	0.2329	−5.2	−22.8	120	98.6	72.1
6	0.6366	0	0.3	170.4	99.2	75.3
7	0.6448	−2.2	0.3	170.4	99.2	75.3
8	0.6560	−3.9	0.3	170.4	99.2	75.3
9	0.6584	−7.4	73.1	55.4	105.2	67.4
10	0.7935	−7.1	−64.5	66.5	95.3	63.8
11	0.8213	−10.7	80.2	−48.1	106.1	71.4
12	0.9336	−11.1	−97.1	46.9	93.5	60.5
13	1.2285	−5.1	−55.3	68.1	103.7	90.6
14	1.3083	−6.8	−64.3	−68.7	104.2	60.1
15	2.1704	−8.7	−78.5	81.5	93.0	61.0
16	2.7105	−13.2	102.7	30.7	104.2	100.7
17	4.2589	−13.9	99.2	−16.4	94.9	62.3
18	4.6003	−13.9	88.8	3.8	93.1	66.7
19	5.4902	−15.8	−101.9	−13.7	92.2	52.9
20	5.6077	−17.1	52.2	9.7	106.7	61.8
21	6.3065	−16	93.3	5.6	93.0	51.9
22	6.6374	−15.7	106.6	0.7	92.9	61.7
23	7.0427	−21.6	119.5	−21.9	105.2	58
24	8.6523	−22.8	−123.8	33.6	107.8	57

Table 3.5: CDL-C per-cluster parameters.

Parameter	C_{ASD} (°)	C_{ASA} (°)	C_{ZSD} (°)	C_{ZSA} (°)	XPR (dB)
Value	2	15	3	7	7

Table 3.6: CDL-E Table [66].

Cluster n	**Normalized Delay** $\tau_{n,model}$	**Relative Power (dB)** P_n	**AoD (°)** $\phi_{n,AoD}$	**AoA (°)** $\phi_{n,AoA}$	**ZoD (°)** $\theta_{n,ZoD}$	**ZoA (°)** $\theta_{n,ZoA}$
1	0.0000	−0.03	0	−180	99.6	80.4
	0.0000	−22.03	0	−180	99.6	80.4
2	0.5133	−15.8	57.5	18.2	104.2	80.4
3	0.5440	−18.1	57.5	18.2	104.2	80.4
4	0.5440	−22.9	−20.1	101.8	99.4	80.8
5	0.5630	−19.8	57.5	18.2	104.2	80.4
6	0.7112	−22.4	16.2	112.9	100.8	86.3
7	1.9092	−18.6	9.3	−155.5	98.8	82.7
8	1.9293	−20.8	9.3	−155.5	98.8	82.7
9	1.9589	−22.6	9.3	−155.5	98.8	82.7
10	2.6426	−22.3	19	−143.3	100.8	82.9
11	3.7136	−25.6	32.7	−94.7	96.4	88
12	5.4524	−20.2	0.5	147	98.9	81
13	12.0034	−29.8	55.9	−36.2	95.6	88.6
14	20.6419	−29.2	57.6	−26	104.6	78.3

where P_1^{LOS} is the relative power of the LOS path which is equal to −0.03 dB from Table 3.6, and P_n is the relative power of NLOS cluster n with N the total number of clusters of the CDL model.

In addition, each CDL model can be scaled in delay so that the model achieves the root mean square (RMS) delay spread according to the desired propagation scenario. This principle is similar for elevation and azimuth angles and the Rice parameter K_R according to the procedure described in the specification.

Scaling of Delays

As previously mentioned, propagation delays for CDL models are normalized, and they must be scaled in delay in order to achieve the desired RMS delay spread as follows,

$$\tau_n = \tau_{n,model} DS_{desired}, \tag{3.13}$$

with $\tau_{n,model}$ the normalized delay value of cluster n in a CDL model and $DS_{desired}$ the wanted delay spread whose certain models are given in Table 3.7.

Table 3.7: $DS_{desired}$ values [66].

Model	$DS_{desired}$
Very short delay spread	10 ns
Short delay spread	30 ns
Nominal delay spread	100 ns
Long delay spread	300 ns
Very long delay spread	1000 ns

Scaling of delays is a mandatory procedure that must be performed in the use of CDL channel profiles for the communication system for link-level assessment.

Channel Impulse Response

This section is devoted to the description of the channel coefficient generation procedure from CDL profiles for LOS and NLOS states according to sections 7.5 and 7.7 of [66].

Parameters of Rays: The determination of ray parameters is described by the three following steps:

- **Departure and arrival angles:**
  The procedure of the generation of departure and arrival angles of ray m inside cluster n is given using [66],

  $$\phi_{n,m,AoD} = \phi_{n,AoD} + \alpha_m C_{ASD}, \tag{3.14}$$

  α_m can be seen as the ray offset angle within a cluster. The values of α_m are summarized in Table 3.8.

  Table 3.8: Ray offset angles.

Ray number m	**Offset angle α_m**
1, 2	$\pm$ 0.0447
3, 4	$\pm$ 0.1413
5, 6	$\pm$ 0.2492
7, 8	$\pm$ 0.3715
9, 10	$\pm$ 0.5129
11, 12	$\pm$ 0.6797
13, 14	$\pm$ 0.8844
15, 16	$\pm$ 1.1481
17, 18	$\pm$ 1.5195
19, 20	$\pm$ 2.1551

  For the generation of angles $\phi_{n,m,AoA}$, $\theta_{n,m,AoD}$ and $\theta_{n,m,ZoA}$, the similar procedure must be applied.

- **Coupling of rays:**
  After the generation of angles of rays, a coupling procedure of rays must be performed. In other words, departure angles $\phi_{n,m,AoD}$ are randomly coupled (or associated) to arrival angles in azimuth $\phi_{n,m,AoA}$ within the cluster n. Similarly, $\theta_{n,m,AoD}$ are randomly coupled to $\theta_{n,m,ZoA}$ in elevation. The coupling principle is realized according to a desired specific distribution, e.g uniform or Gaussian distribution.

- **Cross-polarization of Rays:**
  For the determination of CIR, the cross polarization (XPR) of each ray must be generated according to,
  $$\chi_{n,m} = 10^{X/10}, \tag{3.15}$$
  where X is the value of XPR in dB indicated in each CDL profile.

Channel Impulse Response in NLOS: The CIR for NLOS channel profiles between BS antenna element s and UE antenna element u is defined in downlink by,

$$H_{u,s}^{NLOS}(t,\tau) = \sum_{n=1}^{N} H_{u,s,n}^{NLOS}(t)\,\delta(\tau-\tau_n), \tag{3.16}$$

with $\delta(\cdot)$ the Dirac's delta function, τ_n the delay of cluster n defined in (3.13) and N the number of clusters. The parameter t defines the temporal variability of the propagation environment, while the parameter τ measures the multipath propagation delays. $H_{u,s,n}^{NLOS}$ represents the channel coefficient of cluster n given by,

$$H_{u,s,n}^{NLOS}(t) = \sqrt{\frac{P_n}{M}} \sum_{m=1}^{M} \begin{bmatrix} F_{rx,u,\theta}(\theta_{n,m,ZoA},\phi_{n,m,AoA}) \\ F_{rx,u,\phi}(\theta_{n,m,ZoA},\phi_{n,m,AoA}) \end{bmatrix}^T \begin{bmatrix} e^{j\Phi_{n,m}^{\theta\theta}} & \sqrt{\chi_{n,m}^{-1}}e^{j\Phi_{n,m}^{\theta\phi}} \\ \sqrt{\chi_{n,m}^{-1}}e^{j\Phi_{n,m}^{\phi\theta}} & e^{j\Phi_{n,m}^{\phi\phi}} \end{bmatrix}$$
$$\begin{bmatrix} F_{tx,s,\theta}(\theta_{n,m,ZoD},\phi_{n,m,AoD}) \\ F_{tx,s,\phi}(\theta_{n,m,ZoD},\phi_{n,m,AoD}) \end{bmatrix} e^{\frac{j2\pi\left(\hat{n}_{rx,n,m}^T \hat{d}_{rx,u}\right)}{\lambda}} e^{\frac{j2\pi\left(\hat{n}_{tx,n,m}^T \hat{d}_{tx,u}\right)}{\lambda}} e^{\frac{j2\pi\left(\hat{n}_{rx,n,m}^T \hat{\nu}\right)}{\lambda}t}, \tag{3.17}$$

with M the number of rays within the cluster n which equals to 20. $F_{rx,u,\theta}$ and $F_{rx,u,\phi}$ are the far field patterns of UE antenna element u in GCS while $F_{tx,s,\theta}$ and $F_{tx,s,\phi}$ represent the far field patterns of BS antenna element s. The calculation of the field patterns really depends on the gain radiation patterns and the polarization slant angle. $\Phi_{n,m}^{\theta\theta}$, $\Phi_{n,m}^{\theta\phi}$, $\Phi_{n,m}^{\phi\theta}$ and $\Phi_{n,m}^{\phi\phi}$ define initial random phases for ray m in cluster n. They are uniformly drawn within $[-\pi,\pi]$ for four different polarisation combinations $\theta\theta$ (zenith-zenith), $\theta\phi$ (zenith-azimuth), $\phi\theta$ (azimuth-zenith) and $\phi\phi$ (azimuth-azimuth). $\hat{n}_{rx,n,m}$ is the spherical unit vector with azimuth and elevation arrival angles defined by,

$$\hat{n}_{rx,n,m} = \begin{bmatrix} sin(\theta_{n,m,ZoA})\,cos(\phi_{n,m,AoA}) \\ sin(\theta_{n,m,ZoA})\,sin(\phi_{n,m,AoA}) \\ cos(\theta_{n,m,ZoA}) \end{bmatrix}, \tag{3.18}$$

and $\hat{n}_{tx,n,m}$ is the spherical unit vector with azimuth and zenith departure angles defined by,

$$\hat{n}_{tx,n,m} = \begin{bmatrix} sin(\theta_{n,m,ZoD})\,cos(\phi_{n,m,AoD}) \\ sin(\theta_{n,m,ZoD})\,sin(\phi_{n,m,AoD}) \\ cos(\theta_{n,m,ZoD}) \end{bmatrix}. \tag{3.19}$$

λ is the wavelength, $\hat{d}_{rx,u}$ and $\hat{d}_{tx,s}$ represent the location vectors in Cartesian coordinate system of UE antenna element u and BS antenna element s, respectively. $\hat{\nu}$ is the UE

velocity vector with the speed ν, travel azimuth angle ϕ_ν, travel elevation angle θ_ν, and its expression is given by,

$$\hat{\nu} = \nu \begin{bmatrix} sin\left(\theta_\nu\right) cos\left(\phi_\nu\right) \\ sin\left(\theta_\nu\right) sin\left(\phi_\nu\right) \\ cos\left(\theta_\nu\right) \end{bmatrix}. \tag{3.20}$$

Channel Impulse Response in LOS: The CIR in LOS channel models between BS antenna element s and UE antenna element u in downlink is given by adding the LOS component $H_{u,s,1}^{LOS}\left(t\right)$ to the NLOS CIR shown in (3.16) and scaling both components according to the Rice factor K_R as follows,

$$H_{u,s}^{LOS}\left(t,\tau\right) = \sqrt{\frac{1}{1+K_R}} H_{u,s}^{NLOS}\left(t,\tau\right) + \sqrt{\frac{K_R}{1+K_R}} H_{u,s,1}^{LOS}\left(t\right)\delta\left(\tau-\tau_1\right). \tag{3.21}$$

The expression of the LOS component is highlighted hereby,

$$H_{u,s,1}^{LOS}\left(t\right) = \begin{bmatrix} F_{rx,u,\theta}\left(\theta_{LOS,ZoA},\phi_{LOS,AoA}\right) \\ F_{rx,u,\phi}\left(\theta_{LOS,ZoA},\phi_{LOS,AoA}\right) \end{bmatrix}^T \begin{bmatrix} 1 & 0 \\ 0 & -1 \end{bmatrix} \begin{bmatrix} F_{tx,s,\theta}\left(\theta_{LOS,ZoD},\phi_{LOS,AoD}\right) \\ F_{tx,s,\phi}\left(\theta_{LOS,ZoD},\phi_{LOS,AoD}\right) \end{bmatrix}$$
$$e^{-j2\pi\frac{d_{3D}}{\lambda}} e^{\frac{j2\pi\left(\hat{n}_{rx,LOS}^T \hat{d}_{rx,u}\right)}{\lambda}} e^{\frac{j2\pi\left(\hat{n}_{tx,LOS}^T \hat{d}_{tx,u}\right)}{\lambda}} e^{\frac{j2\pi\left(\hat{n}_{rx,LOS}^T \hat{\nu}\right)}{\lambda}} t. \tag{3.22}$$

3.4 Other Propagation Phenomena

3.4.1 Oxygen Absorption

Certain mmWave frequencies naturally interfere with oxygen molecules, especially at 60 GHz.

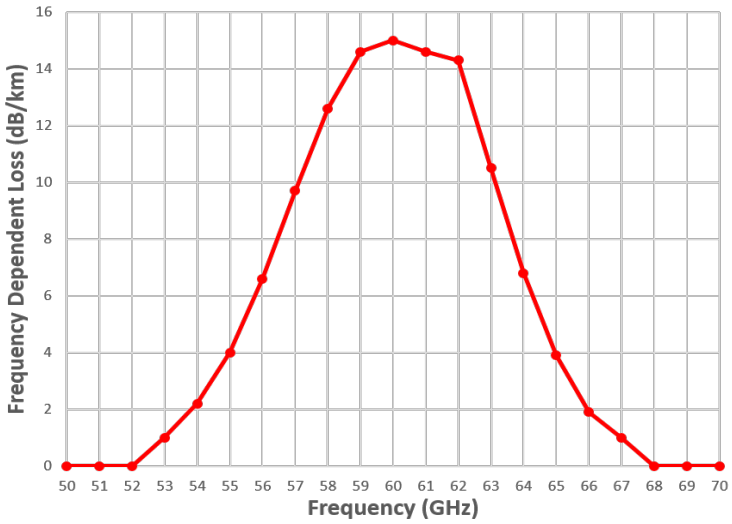

Figure 3.7: Oxygen absorption loss

The oxygen absorption loss is modelled in dB units according to each propagation path or cluster n at frequency f as follows [66],

$$OL_n\left(f\right) = \frac{\alpha\left(f\right)}{1000}\left(d_{3D} + c\cdot\left(\tau_n + \tau_{min}\right)\right), \tag{3.23}$$

where $\alpha(f)$ represents the frequency dependent oxygen loss in dB/km as given in Fig. 3.7, from which a maximum value of 15 dB/km at 60 GHz can be noted. τ_n represents the delay of cluster n and τ_{min} the minimum delay of all clusters of the selected channel model.

3.4.2 Rain Attenuation

One of the major limitations of reliable communication systems operating at mmWave frequencies is the signal attenuation due to raindrops. For the rain attenuation prediction, different models [95] are proposed in the literature. Fig. 3.8 shows several rain attenuation in dB/km versus frequency for different values of rainfall rate according to the ITU-R model.

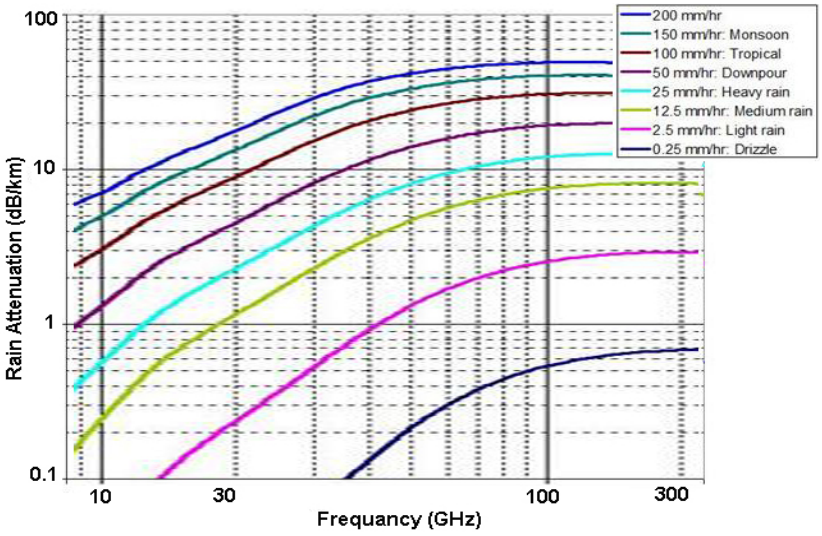

Figure 3.8: Rain attenuation for different rainfall rates [96]

It can be noticed that the rain attenuation is low and can be tolerated for drizzle and light raindrops, especially for the communication distance lower than 1 km which is convenient for mmWave systems deployment. However, the attenuation values become critical due to heavy, downpour, tropical and monsoon rains. In fact, in the 3GPP channel modelling, this limitation is not included as well as the foliage penetration loss.

3.4.3 Foliage Penetration Loss

Although not included in the 3GPP channel modelling, foliage penetration losses for mmWave frequencies can be considered a limiting factor in certain propagation scenarios. Fig. 3.9 gives an illustration of the signal propagation with the presence of densely foliated tree between the Tx and Rx. Different prediction models are proposed in the literature, all depending on the foliage depth $d_{foliage}$ and the frequency f. Some of these theoretical models are summarized in Table 3.9. The foliage penetration loss can be seen as an excess attenuation that must be taken into account in the link budget in addition to the pathloss [101].

In Fig. 3.10, the penetration loss is depicted with respect to the frequency for a foliage depth of 5, 10, 20 and 40 m from the empirical Weissberger model [97].

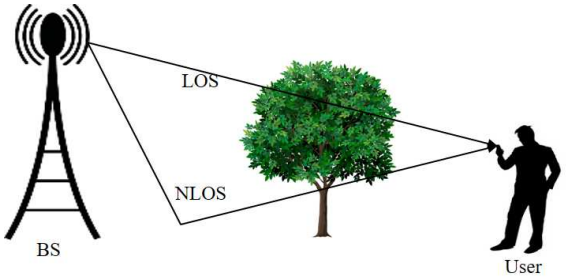

Figure 3.9: Illustration of foliage penetration.

Table 3.9: Foliage penetration loss models.

Reference	**Loss Model (dB)** L	**Frequency** f
Weissberger [97]	$L = \begin{cases} 0.45 f^{0.284} d_{foliage} & 0\,m \le d_{foliage} \le 14\,m \\ 1.33 f^{0.284} d_{foliage}^{0.588} & 14\,m \le d_{foliage} \le 400\,m \end{cases}$, with f in GHz.	0.23 GHz $\le f \le$ 95 GHz
ITU-R Model [98]	$L = 0.2 f^{0.3} d_{foliage}^{0.6}$, $d_{foliage} \le 400\,m$ and f in MHz.	$f \le 1$ GHz
COST-235 [99]	$L = \begin{cases} 26.6 f^{-0.2} d_{foliage}^{0.5} & out-of-leaf \\ 15.6 f^{-0.009} d_{foliage}^{0.26} & in-leaf \end{cases}$, with $d_{foliage} \le 200\,m$ and f in MHz.	9.6 GHz $\le f \le$ 57.6 GHz
Fitted ITU-R [100]	$L = \begin{cases} 0.37 f^{0.18} d_{foliage}^{0.59} & out-of-leaf \\ 0.39 f^{0.39} d_{foliage}^{0.265} & in-leaf \end{cases}$, with $d_{foliage} \le 400\,m$ and f in MHz.	$f \le 1$ GHz

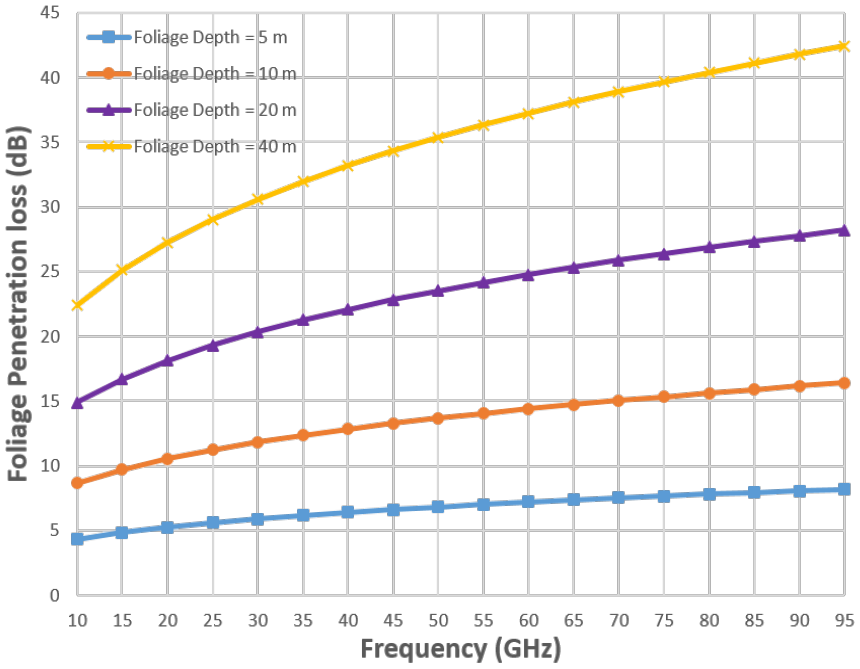

Figure 3.10: Foliage penetration loss

It can be noticed that, for example at 60 GHz, the loss is about 15 dB for 10 m foliage depth, which is almost two times higher than the loss at 10 GHz.

3.5 Conclusion on Channel Modelling

In this chapter, the study on channel models is carried out, including the propagation characteristics in the mmWave context. To meet the requirements of 5G, several candidate multipath channel models have been proposed from collaborative projects, standardization bodies and work carried out by certain institutions. Among all these proposals, in this thesis, the 3GPP channel model was used in the simulations for the following reasons.

In fact, the proposed 3GPP model is flexible, reliable and widely known due to the fact that 3GPP represents the default standardization body for generations of mobile cellular technology. In this context, the simulation results can be easily compared with other authors. This is not the case using very little known channel models like QuaDRiGa and NYU SSCM. In addition, the use of the NYU SSCM model is limited to particular frequencies which are 28, 38, 60 and 73 GHz.

Furthermore, the 3GPP channel model has been defined from the models of collaborative projects such METIS, MiWEBA, mmMAGIC and other contributors, with additional components. This makes this model more complete and suitable for an almost realistic study for frequencies ranging from 0.5 to 100 GHz.

Chapter 4

Dynamic Blockage Phenomenon in Millimeter-Wave Bands

4.1 Introduction

Although mmWave frequencies offer opportunities in terms of huge bandwidth for wireless communication, they are victims of severe attenuation with high sensitivity to blockage leading to communication failure. Blockage is one of the main characteristics of the mmWave propagation channel which results in a severe attenuation of the signal strength. It can be caused by static objects surrounding the propagation environment, such as buildings and outdoor or indoor furniture, or by moving objects such as humans and vehicles.

In fact, the blockage due to human (or to a vehicle) called *dynamic blockage* constituted the main problem of the studies carried out in the context of this PhD thesis. In several experimental studies, measurement results have shown that human body has a significant impact on the signal strength in mmWave bands. The IEEE 802.11ad 60 GHz channel modelling claims that human shadowing is in the range of 18 to 36 dB [104]. Collonge *et al.* [105] have also mentioned an attenuation of 20 dB when the LOS path is shadowed by a person at 60 GHz. Investigations conducted by Lu *et al.* in [106] show that human body attenuates from 20 to 43 dB the signal strength in indoor environment.

In this chapter, the modelling of dynamic blocking phenomenon in the communication system is studied. Methods and techniques to address the blocking problem are reviewed. For the rest, the chapter is organized as follows. In section 4.2, the types of blocking scenarios are described. Section 4.3 is focused on the review of different approaches proposed for the dynamic blockage modelling. In section 4.4, a state-of-the-art of the resolution techniques regarding the blocking phenomenon is presented. And finally, section 4.5 concludes the chapter.

4.2 Categorization of Blockers

In the investigations conducted in the context of human blockage at mmWave frequencies, two types of blocking scenarios have been proposed: the *self-blocking* and *non-self-blocking*.

4.2.1 Self-Blocking Scenario

The self-blocking (SB) is the blocking scenario in which the radio link is obstructed by the user itself particularly by its hand or its body. An illustration of such a scenario is given in Fig. 4.1.

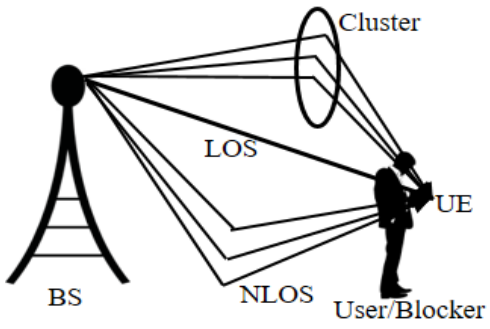

Figure 4.1: Illustration of the SB scenario.

On the basis of this figure, one can note a high probability of blocking of the clusters (or paths) because the spatial dimension of the shadowing is large.

4.2.2 Non-Self-Blocking Scenario

The non-self-blocking (NSB) represents the other type of blocking, which is characterized by the presence of humans or vehicles between the Tx and Rx as illustrated in Fig. 4.2.

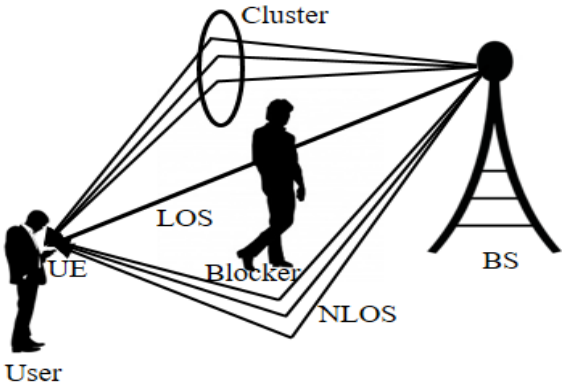

Figure 4.2: Illustration of the NSB scenario.

In this scenario, only a few clusters are likely to be blocked, whereas in the SB scenario, almost all the clusters are obstructed. Therefore, in the NSB scenario, the impact of the blocking phenomenon is worse when it comes to the main propagation cluster which is generally characterized by the LOS path.

4.3 Dynamic Blocking Modelling

In the literature, several theoretical and experimental approaches are proposed to model human blockage in mmWave frequency bands for 5G communications. In this section, a state-of-the-art of techniques for the modelling of SB and NSB scenarios is presented.

4.3.1 3GPP Blockage Models

In the latest 3GPP channel modelling [66], blockage phenomenon due to human or vehicle constitutes an additional component for which two models have been proposed: *model A* and *model B*, each with its own field of application. Indeed, model A is a stochastic blocking model that can be used for prediction purpose through simulation tools, while model B is based on a completely geometric approach for capturing the blocking effect in the realistic environment.

3GPP Model A

As illustrated in Fig. 4.3, model A is a stochastic model in which the blocker is modelled by a blocking region at the Rx.

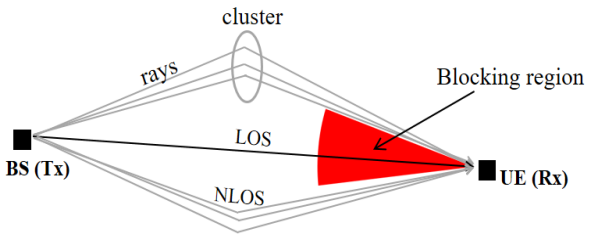

Figure 4.3: Blocking principle of 3GPP model A.

The principle of this approach is to attenuate any cluster whose arrival angle falls into the blocking region. In fact, the blocking region is characterized by an angular spread in elevation defined from $\theta_c - \Delta\theta$ to $\theta_c + \Delta\theta$ and an angular spread in azimuth defined from $\phi_c - \Delta\phi$ to $\phi_c + \Delta\phi$. $\Delta\theta$ and $\Delta\phi$ represent angular spreads with high attenuation centred around θ_c and ϕ_c in elevation and azimuth, respectively. In this way, a cluster is blocked if its arrival angles in elevation θ_{ZoA} and azimuth ϕ_{AoA} are such that $\theta_{ZoA} \in \{\theta_c - \Delta\theta, \theta_c + \Delta\theta\}$ and $\phi_{AoA} \in \{\phi_c - \Delta\phi, \phi_c + \Delta\phi\}$, and the channel gain associated to this cluster is attenuated in dB units by [66],

$$L_{dB} = -20\log_{10}\left(1 - \left(F\left(a_1\right) + F\left(a_2\right)\right)\left(F\left(z_1\right) + F\left(z_2\right)\right)\right), \tag{4.1}$$

where $a_1 = \phi_{AoA} - \left(\phi_c + \frac{\Delta\phi}{2}\right)$, $a_2 = \phi_{AoA} - \left(\phi_c - \frac{\Delta\phi}{2}\right)$, $z_1 = \theta_{AoA} - \left(\theta_c + \frac{\Delta\theta}{2}\right)$ and $z_2 = \theta_{AoA} - \left(\theta_c - \frac{\Delta\theta}{2}\right)$ and $F\left(x\right)$ is defined for $x \in \{a_1, a_2, z_1, z_2\}$ by,

$$F\left(x\right) = s\left(x\right)\frac{1}{\pi}atan\left(\frac{\pi}{2}\sqrt{\frac{\pi}{\lambda_0}r\left(\frac{1}{cos\left(x\right)} - 1\right)}\right), \tag{4.2}$$

with

$$s\left(x\right) = \begin{cases} +1 & \text{if } x \leq 0 \\ -1 & \text{if } x > 0 \end{cases}, x \in \{a_1, z_1\}, \tag{4.3}$$

or

$$s\left(x\right) = \begin{cases} +1 & \text{if } x > 0 \\ -1 & \text{if } x \leq 0 \end{cases}, x \in \{a_2, z_2\}. \tag{4.4}$$

And r in (4.2) represents the distance from the blocker to the receiver (Rx). In Table 4.1, the blocking parameters proposed by 3GPP are summarized, depending on the propagation scenario. The parameters of this model logically show that when the blocker is close to the Rx, the blocking region is large, and inversely. And then, one can deduce that the probability of blockage of clusters is higher in the indoor environment than in outdoor.

Table 4.1: Model A blocking parameters [66].

Scenario	$\Delta\phi$	ϕ_c	$\Delta\theta$	θ_c	r
Indoor	$Uniform([15°, 45°])$	$Uniform([0°, 360°])$	$Uniform([5°, 15°])$	90°	2 m
Outdoor	$Uniform([5°, 15°])$	$Uniform([0°, 360°])$	5°	90°	10 m

3GPP Model B

In model B, the blocker (human or vehicle) is modelled by a rectangular screen which is vertically and perpendicularly oriented with respect to the LOS path between the Tx and Rx as shown in Fig. 4.4.

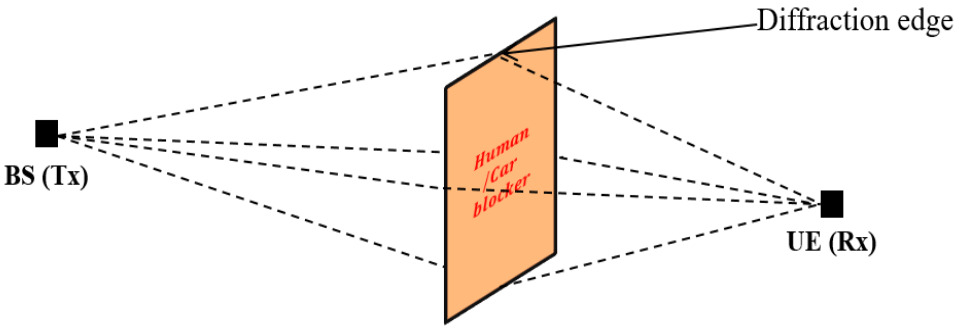

Figure 4.4: Blocker represented by a screen.

Indeed, we can see that any sub-path obstructed by the blocker is diffracted in horizontal and vertical planes by the 4 knife-edges of screen. In this way, the attenuation due to the blocker is determined from the diffraction gain.

Diffraction can be defined as the phenomenon that occurs when the electromagnetic wave meets an obstruction object, for instance a wall with an edge. The Rx thus captures the signal due to radio waves that travel around the obstruction. By considering the knife-like edge obstruction as one side of the screen, Fig. 4.5 gives the scenario of one knife-edge diffraction between the Tx and Rx. h and α represent the obstruction depth and the diffraction angle, respectively. d_{Tx} and d_{Rx} are the Tx and Rx distances from the obstruction screen with knife-edges.

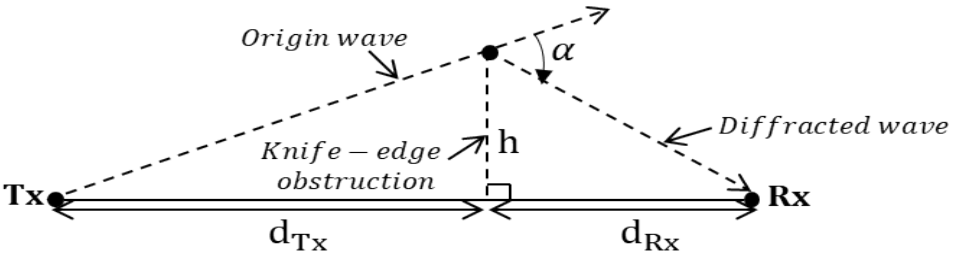

Figure 4.5: Illustration of knife-edge diffraction.

In fact, the depth of obstruction is measured with respect to the direct (LOS) path between the Tx and the Rx. By considering one knife-edge diffraction as diffraction given by an obstructing half-plan as we can see in Fig. 4.5, the used common expression of

diffraction gain is given in [107] by the *Fresnel* integral,

$$F(\nu) = \frac{1+j}{2} \int_{\nu}^{\infty} \exp\left(-j\frac{\pi}{2}t^2\right) dt, \tag{4.5}$$

where $\nu(h) = h\sqrt{\frac{2}{\lambda}\left(\frac{1}{d_{Tx}} + \frac{1}{d_{Rx}}\right)}$ is called the *Fresnel-Kirchoff* parameter.

Several good approximations of $F(\nu)$ have been defined by Lee [107] in decibels units according to ν values. Other techniques have been proposed in the literature for the knife-edge diffraction calculation such Uniform Geometrical Theory of Diffraction (UTD) developed in [18]-[108].

Assuming that the rectangular screen with four knife-edges used for human blocker or vehicle is placed between the Tx and Rx, the modelling given in Fig. 4.4 can be approached by Fig. 4.6 through the separation of top and side views, where

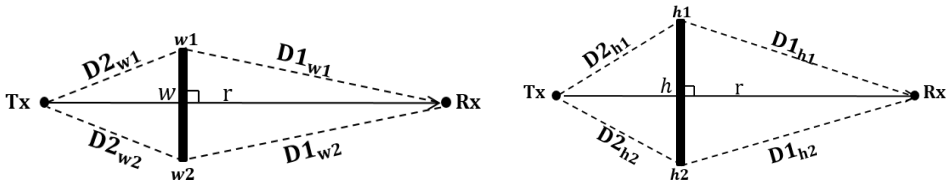

(a) Top view (b) Side view

Figure 4.6: Illustration of human blocker in top and side views.

h and w are the width and the height of the screen, respectively. r represents the distance between Tx and Rx. In Fig. 4.6-(a), $D2_{w1}$+$D1_{w1}$ and $D2_{w2}$+$D1_{w2}$ are the diffracted paths by the edges $w1$ and $w2$ in top view, respectively. And similarly in Fig. 4.6-(b), $D2_{h1}$+$D1_{h1}$ and $D2_{h2}$+$D1_{h2}$ are the diffracted paths by the edges $h1$ and $h2$ in side view, respectively.

Let's consider Fig. 4.6-(a) as two obstructing half-planes of depths w_1 and w_2 such as that $w_1 + w_2 = w$, and waves are diffracted at the edges $w1$ and $w2$ as given in Fig. 4.5. The total received diffracted field by the knife-edge obstruction is the sum of the diffracted fields from the edges of the two obstructing half-planes [110]. In that case, the total diffraction gain by the screen blocker from $w1$ and $w2$ edges is given by $F_w(\nu) = F_{w1}(\nu)+F_{w2}(\nu)$, where $F_{w1}(\nu) = F(\nu)$ in (4.5) for $\nu(w_1) = \pm w_1\sqrt{\frac{2}{\lambda}\left(\frac{1}{d_{Tx}} + \frac{1}{d_{Rx}}\right)}$ and $F_{w2}(\nu) = F(\nu)$ in (4.5) for $\nu(w_2) = \pm w_2\sqrt{\frac{2}{\lambda}\left(\frac{1}{d_{Tx}} + \frac{1}{d_{Rx}}\right)}$ [111]-[112].

As explained in [18]-[111], if the path goes through the screen, only the $(\pm)$ sign is applied as $(+)$ for both edges. Otherwise, the $(+)$ sign is applied for the farthest edge from the path and the $(-)$ is applied for the closest edge to the path. The goal of this approach is only to take into account the shadowing zone.

By adopting the same principle for the side view in Fig.4.6-(b), the diffraction gain is defined by $F_h(\nu) = F_{h1}(\nu) + F_{h2}(\nu)$, where $F_{h1}(\nu) = F(\nu)$ in (4.5) for $\nu(h_1) = \pm h_1\sqrt{\frac{2}{\lambda}\left(\frac{1}{d_{Tx}} + \frac{1}{d_{Rx}}\right)}$ and $F_{h2}(\nu) = F(\nu)$ in (4.5) for $\nu(h_2) = \pm h_2\sqrt{\frac{2}{\lambda}\left(\frac{1}{d_{Tx}} + \frac{1}{d_{Rx}}\right)}$, with

the fact that $h_1 + h_2 = h$.
The diffraction gain from the top, the bottom and the sides of the rectangular screen modelling the human blocker or a vehicle is calculated using *Kirchoff* diffraction equation [113]-[114],

$$F_{Screen} = \frac{j}{2} \int \int_{\nu_1,\nu_2}^{\infty} \exp\left(-j\frac{\pi}{2}\left(t_1^2 + t_2^2\right)\right) dt_1 dt_2, \tag{4.6}$$

with $\nu_1 = \nu(h)$ and $\nu_2 = \nu(w)$ previously defined. Based on the above procedure, we can notice that (4.6) can be rewritten as,

$$\begin{aligned} F_{Screen} &= F_h(\nu) F_w(\nu) \\ &= \left(F_{h1}(\nu) + F_{h2}(\nu)\right)\left(F_{w1}(\nu) + F_{w2}(\nu)\right). \end{aligned} \tag{4.7}$$

By following the approach developed by Medbo and Harrysson in [115], the module of the shadowing component due to the blocker is given by,

$$L = 1 - F_{Screen}. \tag{4.8}$$

And from [115]-[116], an approximation of one knife-edge diffraction from the four edges $w1$, $w2$, $h1$ and $h2$ given by,

$$\begin{cases} F_{h1}(\nu) = F_{h1} &= \frac{arctan\left(\pm\frac{\pi}{2}\sqrt{\frac{\pi}{\lambda}\left(D2_{h1}+D1_{h1}-r\right)}\right)}{\pi} \\ F_{h2}(\nu) = F_{h2} &= \frac{arctan\left(\pm\frac{\pi}{2}\sqrt{\frac{\pi}{\lambda}\left(D2_{h2}+D1_{h2}-r\right)}\right)}{\pi} \\ F_{w1}(\nu) = F_{w1} &= \frac{arctan\left(\pm\frac{\pi}{2}\sqrt{\frac{\pi}{\lambda}\left(D2_{w1}+D1_{w1}-r\right)}\right)}{\pi} \\ F_{w2}(\nu) = F_{w2} &= \frac{arctan\left(\pm\frac{\pi}{2}\sqrt{\frac{\pi}{\lambda}\left(D2_{w2}+D1_{w2}-r\right)}\right)}{\pi} \end{cases}. \tag{4.9}$$

Finally, using (4.8), the attenuation due to the human body in terms of link blocking at the Rx level is given in decibel units through the 3GPP model B by [66],

$$L_{dB} = -20\log_{10}\left(1 - \left(F_{h1} + F_{h2}\right)\left(F_{w1} + F_{w2}\right)\right). \tag{4.10}$$

As mentioned in [116], if the LOS path is not obstructed by the screen, r in (4.9) only represents the distance between the blocker and the Rx, and λ is the wavelength. In Table 4.2, the blocker parameters of model B are given depending on the propagation environment and the type of the blockers.

Table 4.2: Blocker parameters using 3GPP model B [66].

Scenario	Type of blocker	Blocker dimensions	Blocker speed
Indoor; Outdoor	Human	$w = 0.3\,m$ $h = 1.7\,m$	From 0 to 3 km/h
Outdoor	Vehicle	$w = 4.8\,m$ $h = 1.4\,m$	From 0 to 100 km/h

With model B, the blocking principle is applied to the sub-path or ray compared to model A where only the clusters are considered. And the application of (4.10) means that we need to know the lengths of the subpaths that are blocked.

3GPP Self-blocking Modelling

For the SB modelling, the previous model A approach is adopted for which the principle is to attenuate any cluster arriving inside the blocking region as described in Fig. 4.7.

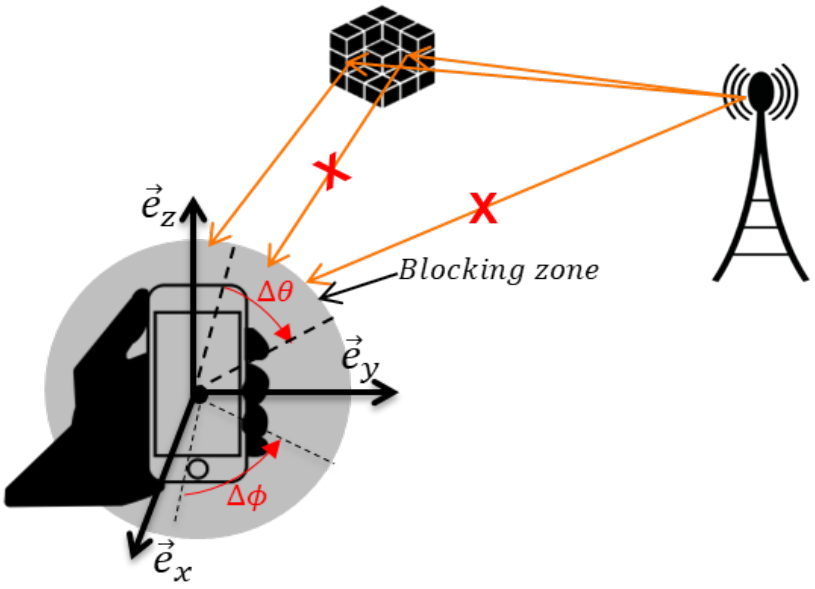

Figure 4.7: Illustration of the SB modelling.

Unlike model A, the angular blocking region parameters shown in Table 4.3 are defined in the UE LCS. This means that the arrival angles of clusters which are generally defined in GCS must be converted into LCS in the application of this model. And then, instead of using the diffraction formula given in (4.1), the blocked clusters are attenuated by 30 dB.

Table 4.3: SB Angular zone parameters [66].

Mode	$\Delta\phi$	ϕ'_c	$\Delta\theta$	θ'_c
Portrait	120°	260°	80°	100°
Landscape	160°	40°	75°	110°

From Table 4.3, it can in fact be noted that the values of the angular regions in the azimuth plane are greater than those defined in the elevation plane in landscape mode. And the inverse trend is logically noted in portrait mode.

4.3.2 Statistical Blockage Modelling by Raghavan *et al.*

Raghavan *et al.* [117] developed a statistical method like the 3GPP model A based on electromagnetic simulations in the 28 GHz frequency band to capture the effect of blockage. The objective of their studies was to statistically analyze the effect of blockage in terms of spatial coverage as well as the attenuation incurred over the angular blocking region. In their approach, the blockers are uniformly distributed in the azimuthal plane around the UE, as shown in Fig. 4.8 in top view. r which is chosen according to a triangular distribution, represents the distance between the blocker and the UE. In fact, r must be greater than a minimum distance, otherwise we are a in the SB configuration.

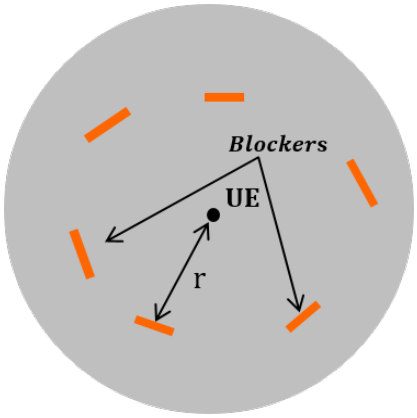

Figure 4.8: Illustration of blockers around the UE.

From their studies conducted in Qualcomm building and outdoors, they came up with average values of the angular blocking region $\Delta\phi$ and $\Delta\theta$, as shown in Fig. 4.9, based on the human height h and width w which are randomly chosen according to a uniform distribution.

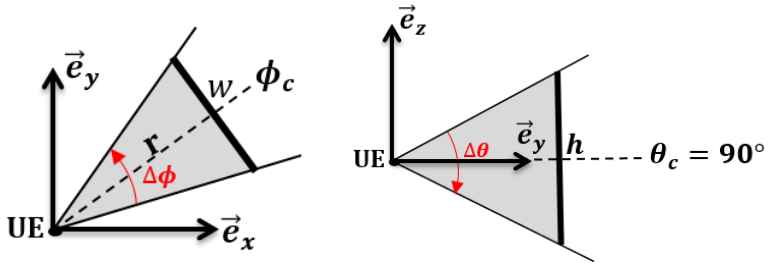

(a) Top view of blocking region (b) Side view of blocking region

Figure 4.9: Blocking region characterization.

The results from their conclusion are given in Table 4.4 for NSB, and in the SB framework, the parameters are similar to those provided by 3GPP in Table 4.3.

Table 4.4: Angular zone parameters for NSB [117].

Blocker	$\Delta\phi$ (°)	ϕ_c (°)	$\Delta\theta$ (°)	θ_c (°)	height h (m)	width w (m)
human	2.5°	$Uniform([0°, 360°])$	15°	90°	$Uniform([1.5, 1.9])$	$Uniform([0.2, 0.4])$
Vehicle	15°	$Uniform([0°, 360°])$	5°	90°	$Uniform([1.0, 1.8])$	$Uniform([4.3, 5.3])$

The working principle of this approach is the same as the 3GPP model A which consists in attenuating each cluster whose arrival angles in azimuth and elevation fall within the blocking zone. Unlike, the 3GPP model A where a diffraction formula is used for the incurred attenuation loss computation, Raghvan *et al.* propose a stochastic model according to Gaussian and Weibull distributions with a mixture of both distributions.

From Table 4.4, we notice that the study results proposed by the authors are quite similar to those given by the 3GPP model A. Nonetheless, the mean angular blocking region values are smaller due to the blockers being further away from the Rx compared to the

3GPP studies [117].

4.3.3 IEEE 802.11ad 60 GHz Model

Another completely stochastic model was adopted by Jacob *et al.* [118] based on ray tracing simulations in combination with an electromagnetic diffraction in the framework of the IEEE 802.11ad 60 GHz channel modelling. In all simulation scenarios, the human blocker was represented by a cuboid with six knife-edges as illustrated in Fig. 4.10, comprising 2 double knife edges (green and blue) for the human body and 2 single knife edges (red) for the human head diffraction.

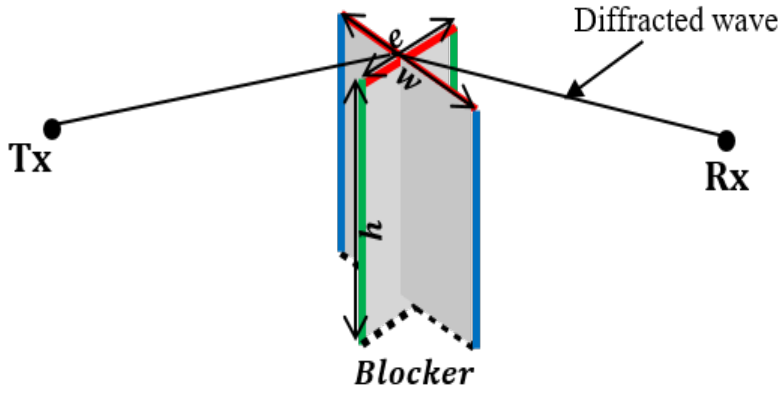

Figure 4.10: Blockage scenario from the IEEE 802.11ad model.

According to the authors, there is no diffraction under the feet of the blocker due to the ground, and then the proposed blocker model is the extension of rectangular screen double knife edge diffraction (DKED) which underestimates the blockage loss.

Based on the measurement results for which the blocker movement was characterized by a uniform walk algorithm of the cuboid, the model is defined to capture the cluster blockage event, i.e the cluster is blocked or not with a certain probability, and the number of simultaneously blocked clusters is modelled by binomial distribution.

Regarding the human blockage loss, the histograms based on results from ray tracing simulations and the random walk algorithm show that the attenuation due to human blockage can be statistically modelled by a truncated Gaussian distribution in dB units.

4.3.4 Other Blockage Models

One of the main channel modelling resulting from the METIS project [18] is the proposal of the blockage component where the blocker is modelled by a rectangular screen like in the map-based 3GPP model B. With this model, the blockage loss is determined through the principle of DKED with four edges given in (4.10).

A modified version of METIS blockage model is proposed by MacCartney *et al.* [109] at 73 GHz in an indoor environment. In their studies, they considered a simple version of DKED with only the side edges for the diffraction principle, and they assumed that the screen height is infinitely vertical. Based on the point-to-point link with a 5 m

Tx-Rx separation distance, they proposed an analytical expression for the computation of the blockage loss that takes into account the expression of antenna gain radiation patterns.

In addition to the KED model, the other most widely spread in the blocking phenomenon modelling is the geometrical theory diffraction (GTD) for which the human blocker is modelled by a perfectly conducting cylinder [119]. The attenuation caused by the blocker is given by an analytical formula which mainly depends on the distance between the Rx antenna and the point of tangency of the cylinder, the wavelength, the cylinder radius.

In [120], Qi *et al.* investigated the blockage loss due to the presence of human through some measurements carried out in an office environment at 11, 16, 28 and 36 GHz. The measurement results showed that the time-based Gaussian shape defined by [121],

$$L(t) = -A_s exp\left(-2\left((t-t_0)\frac{2}{T_s}\right)^2\right), \tag{4.11}$$

really fits the blockage loss when a person walks across the LOS path. In (4.11), A_s is the maximal loss in decibels, t_0 is the instant of the start of the blocking, and T_s is the LOS path blockage duration.

Authors of [122] proposed two simple methods for modelling the blockage events at 73.5 GHz: a simple two-state Markov model with a four-state piecewise linear model based on the time evolution as illustrated in Fig. 4.11.

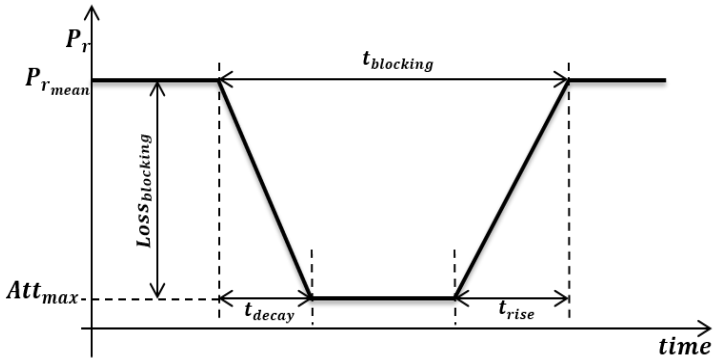

Figure 4.11: Dynamic blockage scenario.

P_r defines the received signal power and $P_{r_{mean}}$ is the average power. Att_{max} represents the maximum attenuation that can be measured. $t_{blocking}$, t_{decay} and t_{rise} are the blockage duration, the decay time and the rise time, respectively. It must be noted that $t_{blocking}$, t_{decay} and t_{rise} depend on the blocker velocity.

The same approach was used by Peter *et al.* [123] to predict the human blockage loss at 60 GHz in a conference room where a maximum attenuation is 25 dB when the LOS path is blocked.

In [124], Bai and Heath proposed a mathematical model for the SB modelling. According to their studies, the user body which represents the blocker is modelled by a blocking cone like the 3GPP SB model, and each path whose arriving angle is inside the cone is attenuated by a constant of 30 dB. They also proposed an analytical expression of signal-to-interference-plus-noise ratio (SINR) expression including the blocking effect.

4.3.5 Conclusion on Blockage Modelling

The objective of this section was to review different strategies proposed in the open literature to model the blocking phenomenon in mmWave communication systems. In general, the blocker is modelled by a rectangular screen and the KED theory is used to predict the blockage loss. On other horizons, the blocker is modeled by a cylinder and the GTD model is applied for the calculation of the attenuation. Based on these map-based models in addition to electromagnetic measurements and ray-tracing simulations, several statistical methods have been proposed to model the blockage events.

In Tables 4.5 and 4.6, a summary of SB and NSB models are given, respectively. In fact, the study on the blocking phenomenon really depends on the antenna model. In other words, the more directional the antenna, the higher the blocking attenuation. However, in the situation where several blockers are located between the Tx and Rx, the total loss is given by adding in dB units the different contributions from each blocker.

Table 4.5: Summary of SB models.

Reference	**Modelling**	**Loss**	**Frequency**	**Antenna Type**
3GPP [66]	Blocking region	30 dB	0.5-100 GHz	Horn [126]
Raghavan *et al.* [117]	Blocking region	$\mathcal{N}(\mu = 15.3\,\text{dB}, \sigma = 3.8\,\text{dB})$	28 GHz	Patch
Bai and Heath [124]	Blocking region	30 dB	28 GHz	Horn
Rajagopal *et al.* [125]	Measurements	40 dB	40 GHz	Horn

As part of this thesis, we focused on the proposed 3GPP modelling, in particular the NSB model A. In fact, the model A can be seen as the computational version of model B which is convenient to experiments in realistic environment. Furthermore, it is also defined for frequencies ranging from 0.5 to 100 GHz compared to other models which are proposed for a particular frequency. And finally, this statistical blocking model is simple to implement and flexible.

Table 4.6: Summary of NSB models.

Reference	**Modelling**	**Loss**	**Frequency**	**Antenna Type**
3GPP Model A [66]	Blocking region	Diffraction Formula	0.5 - 100 GHz	Omni
3GPP Model B [66]	Rectangular Screen	Diffraction Formula	0.5 - 100 GHz	Omni
Raghavan *et al.* [117]	Blocking region	$\mathcal{N}(\mu = 8.54\,\text{dB}, \sigma = 2.5\,\text{dB})$	28 GHz	Patch
IEEE 802.11ad [118]	Probability	$\mathcal{N}(\mu = 18.4\,\text{dB}, \sigma = 8.8\,\text{dB})$	60 GHz	$\lambda/2$-Dipoles
MacCartney *et al.* [109]	Rectangular Screen	20 - 40 dB	73 GHz	Horn

4.4 Blockage Resolution Techniques

Due to the severe propagation loss of electromagnetic waves in mmWave bands, high-gain antenna systems with directional beams are widely deployed to improve the SNR at the Rx. However, concentrating all energy towards the main propagation path through directional communication eliminates the diversity offered by the multipath and represents

a real risk of sudden interruption of communication in the event of obstacles in the beam pointing direction as previously described. To maintain the communication link on-the-move, several techniques have been proposed in the literature, all based on antenna systems and the network architecture.

4.4.1 Equal-Gain Diversity Scheme by Park and Pan

Instead of forming a single beam which concentrates all the energy on the single propagation path with the maximum channel gain, Park and Pan [135] proposed an equal-gain (EG) spatial diversity technique based on the use of more than one beam for the IEEE 802.11ad 60 GHz technology in an indoor environment. The approach consists in using N (2 or 3) strongest among the available propagation paths and forming N simultaneous beams toward each other as described in Fig. 4.12.

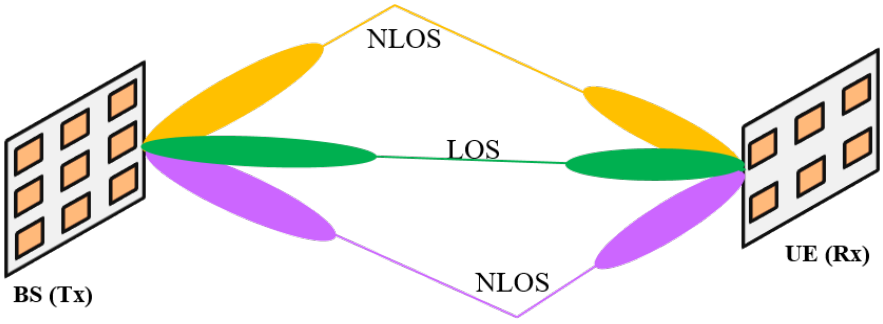

Figure 4.12: Communication based on multiple beams.

The N strongest paths are determined during the beam training process that occurs before the beginning of the communication, and the power gain on each path is set to be equal. The idea behind this technique is to maintain the communication link by relying on the other paths when the main propagation path is blocked.

Although the EG scheme is proven effective to mitigate human-induced attenuation via simulations and experiments, it is expensive and the complexity of the antenna system is very high. In fact, a considerable size of phased antenna array is required to form two or three directional beams. And then, in the context of mmWave communication, the material constraints of such a system are enormous as explained in chapter 1.

4.4.2 Beam Switching Scheme by Xiao

Also called the maximum selection, this approach proposed by Xiao [136] is the revisited version of the previous EG spatial diversity technique. According to the author, the transmit power is wasted in the EG spatial technique when the propagation path with the maximum channel gain is not blocked. Thus, instead of forming multiple beams, each towards a strong path with the same equal power, the communication link can be established on a path with a single beam comprising all the energy like in Fig. 4.13, and the link is switched to the second path with the highest channel gain using another beam when the first is blocked.

Then, when the blocker moves away, the communication is switched again to the first beam. In this mechanism, a procedure of tracking of channel gains during the communication is performed. This means that the effect of blockage is also tracked via the channel

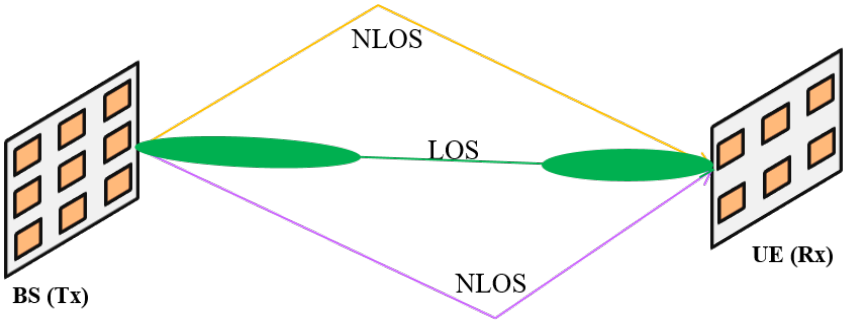

Figure 4.13: Communication based on single beam.

gain.

Compared to the EG approach, the same beam training process for the determination of the N strongest paths is adopted. However the method proposed by Xiao outperforms the EG in terms of received power due to the fact that in non-blocked situation the power is wasted on poor paths with the EG, and in blocked situation, all the energy is concentrated by the beam switching technique on the second path, while the EG uses a part of the transmit power. In addition, the beam switching technique saves computation complexity.

4.4.3 Advanced Beam Switching Techniques

In [137], An *et al.* proposed two algorithms for the selection of alternative path in the context of the beam switching to address the problem of human blockage in an indoor environment of the IEEE 60 GHz standard. The idea is to select during the beam training process two potential paths for data communication: the LOS path as the main communication link and the optimal NLOS link as the backup link in the event of the LOS being blocked. In fact, a path or link is defined by a pair of beams, i.e one Tx beam and one Rx beam for the communication.

The first proposed algorithm is called *SNR-BS* which consists of selecting the NLOS link i with the highest weight factor $\gamma_{i_{SNR}}$ defined by [137],

$$\gamma_{i_{SNR}} = 1 - \left| \frac{\rho_i - \rho_0}{\rho_0} \right|, \tag{4.12}$$

with ρ_i the NLOS path i received SNR and ρ_0 the LOS path received SNR. This algorithm is the most widely used in the beam switching techniques like the MS scheme proposed by Xiao.

The second method called *DSNR-BS* is the extended SNR-BS with the inclusion of directional information. Like the first one, the same approach is adopted for the DSNR-BS mechanism except that the choice of NLOS path is also based on AoA and AoD in order to consider the spatial aspect. The goal is to reduce the probability of blockage regarding the backup NLOS link if it is close to the LOS one. In that case, the NLOS path i is selected with the highest $\gamma_{i_{DSNR}}$ as redefined hereby,

$$\gamma_{i_{DSNR}} = \left(1 - \left| \frac{\rho_i - \rho_0}{\rho_0} \right|\right) sin\left(\frac{\Delta\beta_{t_i}}{2}\right) sin\left(\frac{\Delta\beta_{r_i}}{2}\right), \tag{4.13}$$

with $\Delta\beta_{t_i}$ and $\Delta\beta_{r_i}$ the differences of AoD and AoA between the NLOS path i and the LOS link as given in Fig. 4.14.

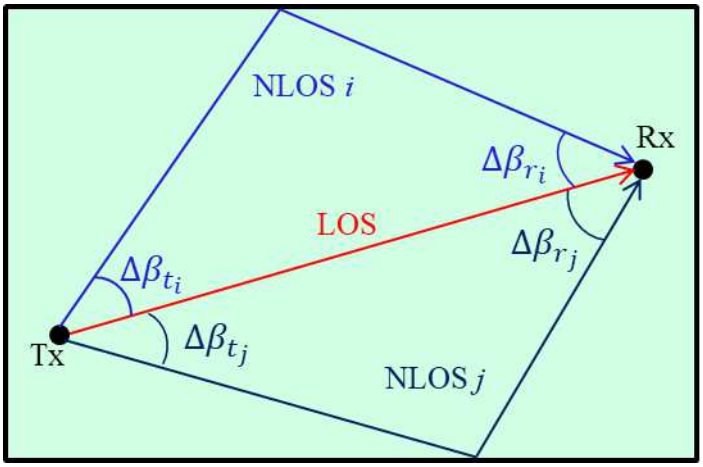

Figure 4.14: Illustration of NLOS paths with respect to LOS.

The advantage of such a method is the reduction in the probability of blocking concerning the backup link when the main path is not available. However, the limitation is the fact that a low SNR value can be obtained associated to this alternative link.

The same idea for the selection of beams including spatial information was also adopted by Gao *et al.* [138] at 60 GHz in indoor communications. Indeed, they proposed a double-link tracking and switching method to cope with the human blockage problem. The double-link is composed of the transmission and backup links which are selected so that their respective beams do not overlap. And then the beams are tracked and switched when one of them is blocked.

4.4.4 Other Blockage Resolution Techniques

The beam switching technique can be very limited in the context of the blockage resolution when the channel is poor in terms of multipath and there is no better cluster to switch to. In this scenario, other techniques are proposed in the literature. Some of them are mentioned here as follows.

Network Densification

The idea of densifying the network by deploying several BSs or access points (APs) with handover algorithms makes it possible to keep the link on-the-move in the blockage situation.

As explained by Raghavan *et al.* [126], the fact that multiple BSs are deployed and cells overlap, could provide different dominant paths from these BSs to a UE via distinct scatterers. In this case, when the current link is detected blocked with the BS, the UE can launch a handover mechanism in order to switch the communication with another BS.

The other idea is the AP diversity instead of handover, i.e several APs are deployed and different communication links are established between the APs and the UE. This is

explained by Zhang *et al.* [139] with the multi-AP architecture proposal to solve the human blockage problem in an indoor propagation environment at 60 GHz. To this end, they proposed policy for the AP selection based on an access controller so that when one of wireless links is blocked, another AP can be selected to complete remaining transmissions.

Studies conducted by Jain *et al.* [140] showed that the higher the density of BSs, the lower the probability of blockage of the communication link. The authors in [141] use a machine learning approach to show the positive effect of linearly increasing BS density versus blocking density to maintain system connectivity.

However, even if Sato and Manabe [142] mentioned that the heights of user terminals and BSs can contribute to the reduction of the number of BSs with a lower probability of blockage, the network densification remains a very expensive technique.

Beam Expansion Technique

One of the most cost effective blockage resolution techniques is the use of large beams in the communication system. For this purpose, a plethora of beam widening algorithms is proposed in the literature. It is clear that a large beam can simply be used when the main path is blocked by an obstacle (human or vehicle), in order to capture energy from other multipath components; but in this case, a large amount of transmitted power is lost, and the cell coverage is ineffective.

4.5 Conclusion on Dynamic Blockage in mmWaves

The sensitivity to the blockage due to the sudden presence of human or vehicle on the communication link constitutes one of the challenges in the use of mmWave frequency bands. Several methods were developed from the diffraction theory, ray tracing simulations and electromagnetic measurements to model the blockage phenomenon in mmWave communication systems. As part of this thesis, we focused on the statistical modelling proposed by 3GPP to analyze the impact of blockers on communication performance. The results of the simulation are presented and commented on in chapter 5 of the manuscript.

As the blockage can be the cause of the abrupt interruption of the communication link, different techniques have been proposed in order to address the problem. These solutions are classified into different ideas among which, we note the idea of beam diversity, the beam switching approach, the theory of network densification, and finally the beam widening approach.

Regarding the beam switching approach, it can be considered as the widely known and simplest solution to solve the blockage problem using a phased antenna array. The main limitation of such a technique in a realistic scenario is the detection of the blocker and how fast the current beam can switch to the backup beam.

However, one can densify the network through the deployment of several BSs or APs, and by using the handover or by exploiting the AP-diversity, the communication can be maintained in a context of blockage. The problem of this approach is the high cost of the network and the complexity at the UE to track the beams from the other BSs.

Although the multipath aspect can be exploited via the beam widening method, the antenna directivity can be compromised, especially in the context of mmWave communications. In the beam diversity approach, multiple beams are created, pointing in the directions of two or three propagation paths with high channel gains. This method can be considered optimal, but using a phased antenna array in this context can be critical due to the high complexity and overhead of the beamforming process, which can eventually degrade the system performance.

By focusing on the same approach and to overcome these shortcomings, the idea of multibeam antennas can be appreciated. Chapter 6 of the document deals with a proposal of theoretical and generic approach of multibeam antenna.

Chapter 5

Simulation Chain Validation and Impact of Blockage on Communication Performance

5.1 Introduction

As part of the PhD thesis, the entire PHY layer communication chain was implemented in the Galacsy simulation tool for link-level evaluation. The objective of this chapter is to highlight some link-level simulation results from the implemented chains described in chapters 2, 3 and 4. And then, these simulation results are compared to certain literatures in terms of BER or BLER.

In fact, this step of the thesis project was required for the purpose of validating the implemented 5G PHY layer chain that can be used to illustrate the results of certain ideas and methods. Therefore, the impact of blocking phenomenon on communication performance is highlighted.

A general summary of this communication chain is given in Fig. 5.1, with the singular value decomposition (SVD) used as the MIMO precoding. Consequently, regarding the validation procedure, several sub-chains are deduced from the global one indicated in Fig. 5.1 according to the configuration given in the reference literature.

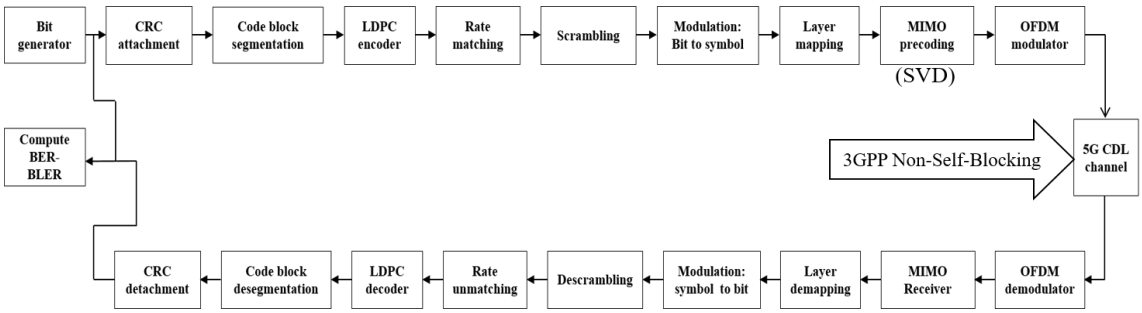

Figure 5.1: Communication block diagram of 5G.

To do so, the following organization of the chapter is adopted. In section 5.2.1, BER performance using an uncoded communication chain including an additive white Gaussian noise (AWGN) channel is presented. Sections 5.2.2 and 5.2.3 are focused on BLER

performance resulting from the single-input single-output (SISO) and MIMO communication chains, respectively. In section 5.3, the implementation method and validation of the 3GPP non-self-blocking (NSB) statistic model are given. And then the impact of the blockage phenomenon on communication performance is analyzed in section 5.4. Finally, the chapter conclusion is drawn in section 5.5.

5.2 Simulation Chain Validation

5.2.1 Uncoded SISO Chain with AWGN Channel

The first step of the validation procedure was based on the use of the SISO communication chain without LDPC channel coding as illustrated in Fig. 5.2.

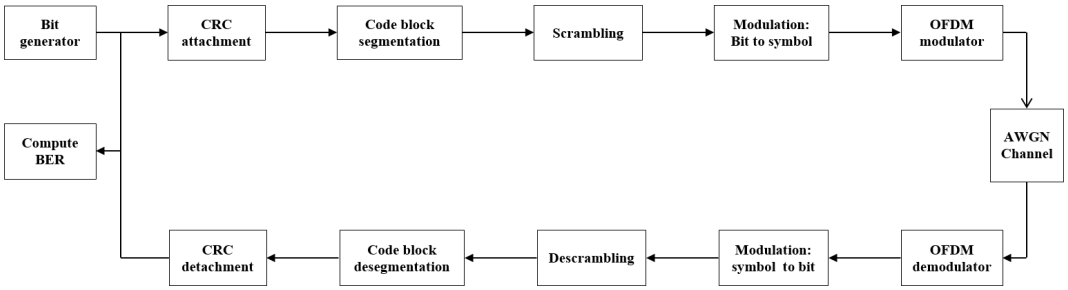

Figure 5.2: Uncoded SISO chain including AWGN channel.

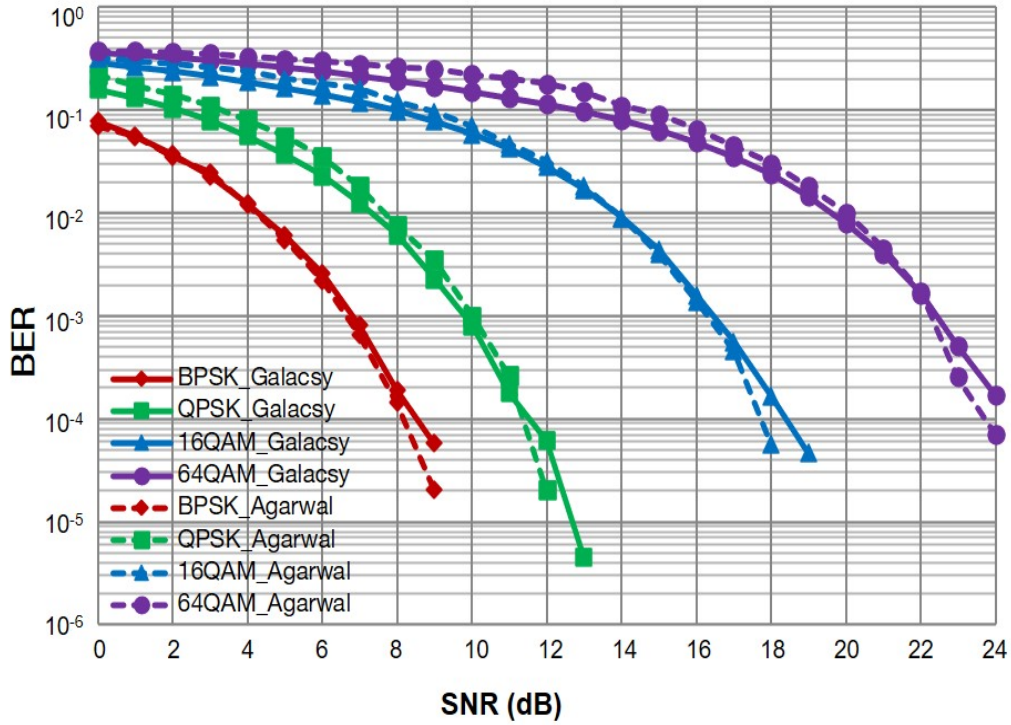

Figure 5.3: BER Performance comparison with Agarwal *et al.* [143].

The validation of the PHY blocks of Fig. 5.2 is shown through the calculation of the BER parameter. In this way, Fig. 5.3 shows the performance comparison with Agarwal

et. al [143] using the modulation schemes such as BPSK, QPSK, 16QAM and 64QAM. From this figure where the BER performance versus SNR is represented, we notice a good agreement between the simulation results of Agarwal *et al.* and those given by our Galacsy simulator for each of the applied modulations. These results validate the implementation of the 5G PHY processing blocks indicated in Fig. 5.2.

Based on this result, the goal of the remainder of the procedure will be to use these blocks in addition to some of the mentioned modulation schemes to validate the implemented 5G channel coding and CDL multipath channels.

5.2.2 Encoded SISO Chain with AWGN Channel

This subsection is devoted to the second stage of the validation procedure which consists in analyzing the communication performance using the 5G LDPC encoding including the comparison with the simulation results of studies conducted by Wu *et al.* [39]. To this end, the communication chain of Fig. 5.4 is used.

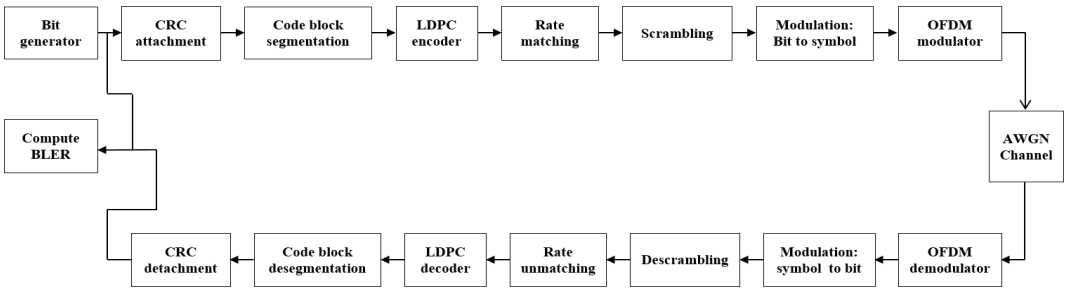

Figure 5.4: LDPC encoded SISO chain including AWGN channel.

The objective here is the validation of the implemented 5G LDPC channel coding and the normalized min-sum (NMS) decoding algorithm used in the communication chain. The performance comparison in terms of BLER versus SNR is given in Fig. 5.5 for the BPSK modulation with the value of $\alpha = 0.7$ designing the NMS parameter. Simulations are carried out for the coding rates $R = 1/5$, $R = 1/4$ and $R = 1/3$ with 15 decoding iterations.

From Fig. 5.5, we notice similar performance between simulation results of Wu *et al.* and those obtained with the implemented chain given in Fig. 5.4 for each coding rate.

The same trend is observed with the BLER performance versus SNR of Galacsy and the result from the work of Wagner [53] where the NMS decoding algorithm is used with a scaling parameter $\alpha = 0.65$ for QPSK modulation scheme and a coding rate $R = 1/5$. Based on these analyses, the 5G LDPC encoding and the NMS decoding algorithm implemented in the Galacsy simulation tool are validated and can be used for other objectives.

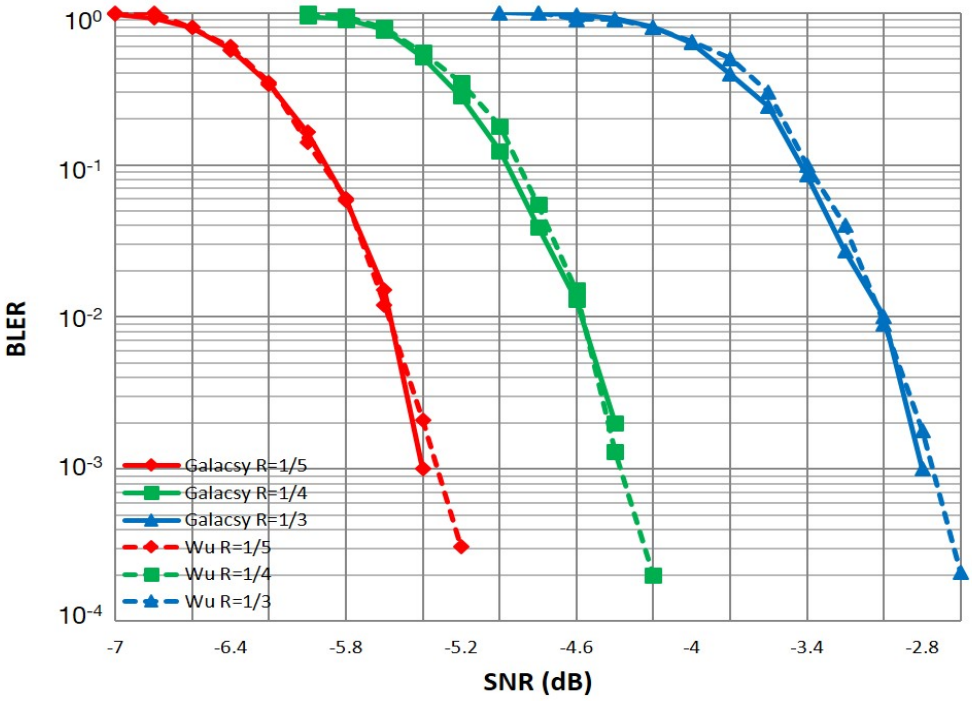

Figure 5.5: BLER Performance comparison with Wu *et al.* [39].

5.2.3 Encoded MIMO Chain with CDL Channel

Likewise, the goal here is the analysis of simulation results for the purpose of validating new blocks such as MIMO precoding and 5G CDL channel models. In this context, the communication chain given in Fig. 5.6 is used for link-level assessment in terms of BLER versus SNR according to studies conducted by Zhao *et al.* [144].

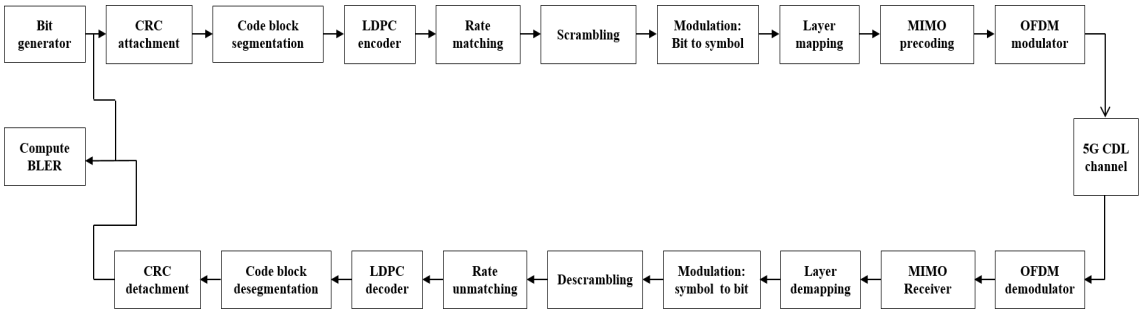

Figure 5.6: LDPC encoded MIMO chain with CDL channel.

In this regard, the MIMO 4x4 configuration with SVD precoding is used in the 26 GHz frequency band. In all simulations, the UE expected four data streams belonging to the same codeword. For the multipath propagation channel, the CDL model A [66] is used with a uniform linear antenna array. In this study, we assumed a perfect channel estimation at the Rx and an MMSE algorithm is used in channel equalization.

The remaining simulation parameters are summarized in Table 5.1 with respect to those used by Zhao *et al.* [144]. The performance comparison with respect to simulation results of Zhao *et al.* is given in Fig. 5.7.

Table 5.1: Simulation parameters

Parameters	**Values**
Bandwidth	34.56 MHz
Subcarrier spacing	120 kHz
Antenna array	omnidirectional elements
Modulation scheme	16QAM
Coding rate	0.64

From this figure, we notice that in low SNR regime, the performance given in [144] slightly outperforms the the performance obtained with the Galacsy tool, with a maximum SNR difference of 3 dB for BLER values 10^0 and 10^{-1}.

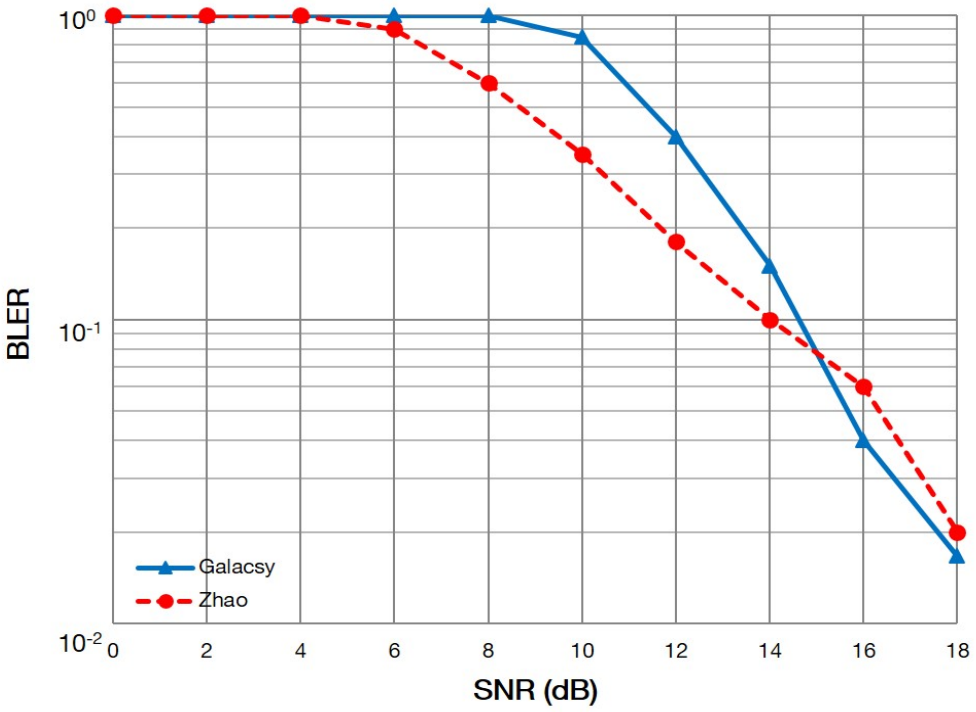

Figure 5.7: BLER Performance comparison with Zhao *et al.* [144].

However, for high values of SNR, especially from 14 dB, the trend is inverted, i.e the simulation results are almost similar with the fact that the performance given by Galacsy slightly takes over. This is maybe due to the influence of delay spread scaling factor $DS_{desired}$ used in the calibration of CDL channel models as explained by studies conducted by Barb and Otesteanu in [145]. In fact, in this work, even if $DS_{desired}$ is fixed at 85 ns, several values were tested in order to approach the performance of [144] because the authors did not mention this information.

Although in this section the calibration and validation of the SVD and CDL A MIMO channel are pointed out, all PHY blocks in the communication chain are also included. The next sections consist in taking into account the blockage phenomenon.

5.3 Blockage Implementation Specification

This section is mainly focused on the procedure for implementing the blockage phenomenon based on the 3GPP model A. The objective is to give some implementation details from the presence of the blocker to the attenuation calculation of blocked channel clusters. An analysis of simulation results is presented.

5.3.1 Identification of Blockage Phenomenon

The first step in the implementation process is to confirm and identify the type of blockage (SB or NSB) in the communication system. In this way, the idea is to define the number of blockers $N_{Blockers}$ in the propagation environment for each type of blockage. If $N_{Blockers}$ is equal to "0", it means that the concerned blocking scenario does not exist, otherwise the blocking phenomenon exists. For the SB scenario, it is obvious that $N_{Blockers}$ must be equal to "1" and in the NSB context, $N_{Blockers}$ can be greater than "1". In the rest of section, we will focus on the NSB scenario.

5.3.2 Blocker Location

The second idea in the implementation algorithm is the location of blockers in the propagation environment. The location is given by the values of azimuth and elevation angles. In this case, the approach is flexible, i.e the values given in the 3GPP TR 38.901 can be used, or other desired values. The chosen values in each plan (elevation and azimuth) are the entries of a vector of size $N_{Blockers}$.

5.3.3 Blocker Dimensions

When blockers are located, their dimensions defined by the angular spreads $\Delta\phi$ in azimuth and $\Delta\theta$ in elevation must be given in vectors of size $N_{Blockers}$ according to the same theory defined in the previous section.

5.3.4 Simulation of Blockage Phenomenon

Depending on the model of CDL table, the arrival angles in azimuth and elevation of clusters are individually considered and the principle of blockage simulation described in chapter 4 is applied for each blocker. And after the blockage simulation, the new CDL table with modified channel gains is used for the link-level simulation.

In Fig. 5.8, the attenuation due to the presence of human blocker based on the 3GPP model A is given in an indoor environment at the 26 GHz frequency band, with $\Delta\phi = 45°$ and $\Delta\theta = 15°$. From this figure, we notice that the attenuation is all the more significant as the direction of propagation path is closer to the center of the blocker characterized here by angle in azimuth $\phi_c = 90°$ and angle in elevation $\theta_c = 90°$. This mechanism is justified by the modelling of human blocker through a rectangular screen for which the diffraction formula is applied.

The diffraction approach highlights the fact that if the cluster is closer to the knife-edges of the screen, the signal power is very lowly attenuated. And if the cluster meets the center of the screen, the signal strength is attenuated to the maximum.

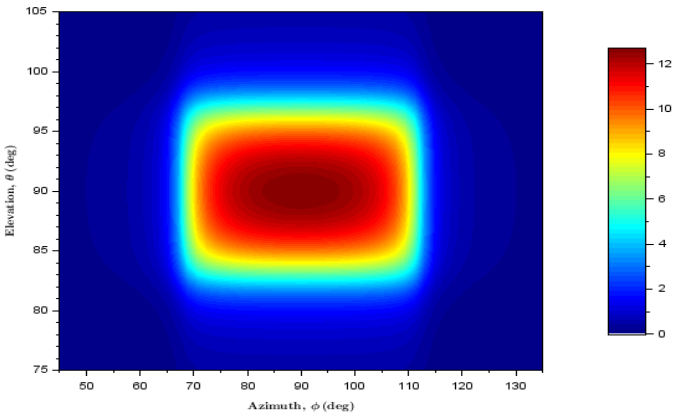

Figure 5.8: Human blockage attenuation in dB units.

Note that due to cosine expression in the diffraction formula, the value of attenuation admits a symmetric axis in each of both plans, azimuth and elevation through ϕ_c and θ_c, respectively. Therefore, the attenuation ranges from 0 to 12.71 dB at 26 GHz for one blocker. These theoretical values are justified and confirmed by measurements conducted by Zhao *et al.* [147] in the indoor environment to quantify the value of human body attenuation at 26 GHz. Results show that the communication link is attenuated by a maximum value of 12.66 dB for the presence of one person between the Tx and the Rx.

5.4 Impact of Blockage on Communication Performance

This section deals with the impact of human blockage on 5G communication systems in mmWave bands. The analysis of communication performance in terms of BLER with and without the influence of human blockage is proposed in the 26 GHz band, thanks to the implementation of the 5G PHY communication chain given in Fig. 5.9 in the Galacsy simulation tool. Based on the BLER performance, a link budget is also established in order to evaluate the impact of blockage on the cell coverage.

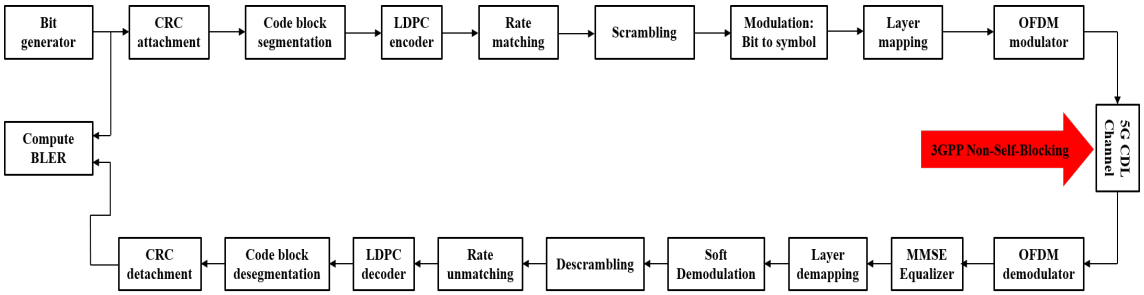

Figure 5.9: 5G PHY layer SISO chain including blockage.

To this end, only one BS considered as the Tx and one UE considered as the Rx are used with the 3GPP LOS channel profile CDL E described in chapter 3. Both scenarios with and without human blockage are considered in indoor environment. The blocking system is applied such that the LOS path fully meets the center of the blocker whose parameters are given in Table 5.2 where r represents the distance between the Rx and the blocker.

Table 5.2: Simulation parameters.

Parameters	Values
Carrier frequency	26 GHz
Bandwidth	400 MHz [60]
Sub-carrier spacing	120 kHz [60]
FFT size	4096
Channel model	3GPP LOS Channel Profile CDL E, $DS_{desired} = 100\,ns$ [66]
Blocking region parameters	$\Delta\phi = 45°$, $\phi_c = -180°$, $\Delta\theta = 15°$, $\theta_c = 80.4°$, $r = 2\,m$
Number of human blockers	1
Channel estimation	Ideal
Antenna model	3GPP sector antenna radiation pattern with gain $G_{max} = 8$ dBi [66]
LDPC decoding algorithm	Normalized Min-Sum (NMS) with normalization factor $\alpha = 0.7$
LDPC decoding iterations	50

We assume that the blockage phenomenon occurs during the whole data transmission between the BS and the UE. The same antenna model is used for transmission and reception, and its boresight almost matches the LOS path of the CDL E profile.

5.4.1 Link-Level Evaluation

As previously mentioned, the advantage of mmWave is focused on 5G eMBB applications for which the target BLER is 10% [146]. Fig. 5.10 highlights the BLER vs SNR performance for both scenarios with and without blockage using MCS 9 (16QAM, code rate = 0.6) and CDL E channel model with one antenna at the Tx and one antenna at the Rx.

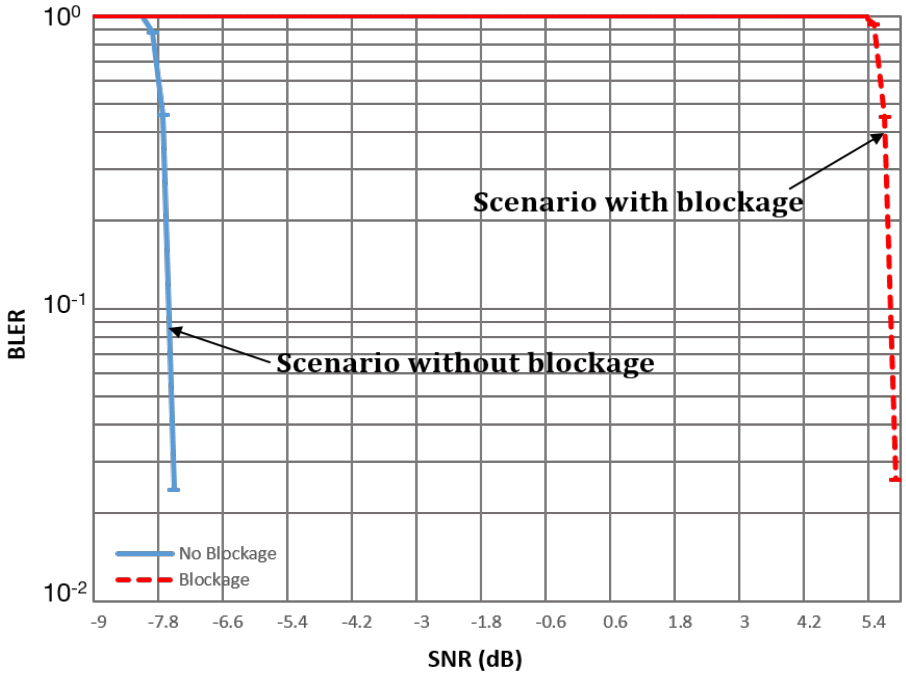

Figure 5.10: BLER vs SNR in SISO.

For BLER=10%, we observe that the link without blocker is better than the link including human blocker with a SNR difference about 13 dB. This result is justified by the blockage (attenuation of 12.71 dB) of the LOS path which is the most dominant path. The same trend is observed by comparing the channel power of CDL E profile without blockage with this one of CDL E including the blockage of the LOS cluster.

5.4.2 Impact of Blockage on the Cell Coverage

In this section, the influence of the blockage phenomenon on the communication range is highlighted. To this end, the maximum distance between the BS and UE is evaluated from the analysis of the Rx power including the pathloss through the establishment by means of the link budget.

Link Budget Principle

Link budget is a step-by-step calculation process including signal powers, antenna gains, and any losses encountered along the communication link. The objective of such a process is to determine the quality of the link given here by parameters such as BER and BLER performance, which correspond to a SNR at the input of the demodulator. The general principle of the link budget is highlighted in dB through,

$$P_{\mathrm{Rx}} = P_{T\mathrm{x}} + G_{T\mathrm{x}} + G_{\mathrm{Rx}} - PL - x - L_{all}, \tag{5.1}$$

where P_{Rx}, $P_{T\mathrm{x}}$, $G_{T\mathrm{x}}$ and G_{Rx} represent the Rx power commonly called *sensitivity*, Tx power, Tx antenna gain and Rx antenna gain, respectively. PL represents the pathloss and x is the shadowing, modelled as a centred log-normal variable $\mathcal{N}\left(0, \sigma^2\right)$. Parameter L_{all} includes losses such as cable attenuation, connector loss and thermal noise.

In communication systems, the link can be interrupted if the Rx sensitivity is below a given target threshold denoted $P_{\mathrm{Rx}_{target}}$,

$$P_{\mathrm{Rx}} < P_{\mathrm{Rx}_{target}}. \tag{5.2}$$

The use of the parameter $P_{\mathrm{Rx}_{target}}$ leads to the application of the maximum pathloss PL_{max} for which a shadowing margin M_{sh} is taken into account. Indeed, the shadowing margin is the margin that ensures a given coverage reliability over a cell. With this margin, the link budget is defined from (5.1) as,

$$P_{\mathrm{Rx}_{target}} = P_{T\mathrm{x}} + G_{T\mathrm{x}} + G_{\mathrm{Rx}} - PL_{max} - M_{sh} - L_{all}, \tag{5.3}$$

and it includes the maximum communication $d_{2D_{max}}$ which is also equal to the maximum radius r_{max} for a circular cell.

Shadowing Margin Calculation

For the calculation of the shadowing margin, the following probability called the outage probability P_{outage} is considered, and it defines the probability that the communication link is broken. This is explained from (5.1), (5.2) and (5.3) by,

$$\begin{aligned} P_{outage} &= \Pr\left(P_{\mathrm{Rx}} < P_{\mathrm{Rx}_{target}}\right) \\ &= \Pr\left(P_{T\mathrm{x}} + G_{T\mathrm{x}} + G_{\mathrm{Rx}} - PL - x - L_{all} < P_{\mathrm{Rx}_{target}}\right) \\ &= \Pr\left(x > PL_{max} - PL + M_{sh}\right). \end{aligned} \tag{5.4}$$

In fact, from the pathloss expression described in chapter 3, one can deduce the expression of PL_{max} as,

$$PL_{max} = \alpha + 10\beta \log_{10}\left(d_{3D_{max}}\right) + 10\gamma \log_{10}\left(f\right). \tag{5.5}$$

With $d_{3D_{max}} = \sqrt{d_{2D_{max}}^2 + \left(h_{BS} - h_{UE}\right)^2}$. In this way, we can show that,

$$PL_{max} - PL = 10\beta \log_{10}\left(\frac{d_{3D_{max}}}{d_{3D}}\right). \tag{5.6}$$

As the shadowing x is Gaussian, (5.4) can be rewritten as,

$$P_{outage} = \frac{1}{2} erfc\left(\frac{M_{sh} - b\ln\left(\frac{d_{3D_{max}}}{d_{3D}}\right)}{\sigma\sqrt{2}}\right), \tag{5.7}$$

with $b = \frac{10\beta}{\ln(10)}$.

The shadowing margin is generally evaluated under a cell coverage probability (e.g. 90%) as explained in [148]. Nevertheless, a simplified way is to consider an outage probability μ_{edge} at the cell edge. In that case, the distance between the Tx and Rx d_{2D} is equal to the maximum distance $d_{2D_{max}}$. And (5.7) becomes,

$$P_{outage} = \frac{1}{2} erfc\left(\frac{M_{sh}}{\sigma\sqrt{2}}\right). \tag{5.8}$$

As $P_{outage} = \mu_{edge}$ in this context, the shadowing margin is naturally given by,

$$M_{sh} = \sigma\sqrt{2} erfc^{-1}\left(2\mu_{edge}\right). \tag{5.9}$$

In fact, to determine the shadowing margin M_{sh} under a coverage probability over the whole cell, assuming a simple circular cell, the expression of the cell outage probability, denoted μ_{cell} given in (5.10) must be considered.

$$\begin{aligned}
\mu_{cell} &= \frac{1}{\pi r_{max}^2} \int_{\theta=0}^{2\pi} \int_{r=0}^{r_{max}} P_{outage}\left(r\right) r \, dr \, d\theta \\
&= \frac{2}{r_{max}^2} \int_{r=0}^{r_{max}} P_{outage}\left(r\right) r \, dr \\
&= \frac{1}{r_{max}^2} \int_{r=0}^{r_{max}} erfc\left(\frac{M_{sh} - b\ln\left(\frac{d_{3D_{max}}}{d_{3D}}\right)}{\sigma\sqrt{2}}\right) r \, dr.
\end{aligned} \tag{5.10}$$

Cell Coverage Analysis

From the performance BLER=10% given in Fig. 5.10, we establish the link budget in order to illustrate the consequence of human blockage phenomenon on the system capacity in terms of cell coverage in mobile communication as given in Table 5.3.
To this end, PL_{max} represents the maximum value of the pathloss allowing to determine the cell range in both scenarios with and without the presence of human blockage on the communication link. In the calculation, we consider a transmit power of 10 dBm [149] and a coverage probability of 95%.

Table 5.3: Link Budget in the 26 GHz band.

Parameters	**Scenario without blockage**	**Scenario with blockage**
Tx Power	10 dBm	10 dBm
Tx Antenna gain	8 dBi	8 dBi
Tx Cable loss	3 dB	3 dB
EIRP	*15 dB*	*15 dB*
Thermal noise density	-174 dBm/Hz	-174 dBm/Hz
Noise bandwidth (400 MHz)	85.80 dB	85.80 dB
Rx Noise figure	9 dB	9 dB
Thermal Noise	79.20 dBm	79.20 dBm
Noise rise	3 dB	3 dB
Rx Antenna gain	8 dBi	8 dBi
Rx Cable loss	0 dB	0 dB
Required SNR for BLER=10%	-7.7 dB	5.7 dB
Rx Sensitivity	*-91.90 dBm*	*-78.50 dBm*
Cell coverage probability	95% dB	95%
Shadowing standard deviation	3 dB	3 dB
Shadowing margin	2.95 dB	2.95 dB
Pathloss max PL_{max}	**103.95 dB**	**95.55 dB**

Based on this cell coverage probability and by assuming that Gaussian shadowing is considered with standard deviation of 3 dB, a shadowing margin of 2.95 dB is deduced. As defined in [66], the pathloss in LOS state propagation environment is defined by,

$$PL_{LOS} \ \ (dB) = 32.4 + 17.3\log_{10}(d_{3D}) + 20\log_{10}(f), \tag{5.11}$$

where $d_{3D} = \sqrt{d_{2D}^2 + (h_{BS} - h_{UE})^2}$, with d_{2D} the distance from the BS to the UE which defines the cell range, h_{BS} and h_{UE} the BS and UE heights, respectively. With the maximum pathloss PL_{max} from the link budget, for $h_{BS} = 3\,m$ and $h_{UE} = 1.5\,m$ in the 26 GHz band, we deduce from (5.11) that the scenario without human presence on the LOS link has a cell range of $d_{2D_{max}} = 316.3\,m$ while the blockage of the LOS link results in a cell range of $d_{2D_{max}} = 53.13\,m$. From this analysis, it can be seen that to guarantee the same quality of service, the communication range must be drastically reduced in the 26 GHz mmWave band.

5.5 Conclusion

In this chapter, the communication performance generally evaluated in terms of BER or BLER versus SNR is analyzed and compared to other authors. The purpose was focused on the validation of 5G PHY layer communication chains studied and implemented in the Galacsy simulation tool. In addition to the processing blocks of the PHY layer, CDL channel models with the 3GPP statistical blocking model have been included in the communication chains. In all scenarios, the simulation results were almost similar to those given by the authors in the literature. Regarding the blockage phenomenon, an implementation procedure and a validation of the attenuation value in the 26 GHz were also highlighted. We also took advantage in this chapter to analyze the influence of the blockage. Simulation results revealed that the communication performance is really impacted when the main propagation path is really attenuated by a human or a vehicle. From the BLER performance, the link budget is established for illustration purposes. We noticed that the communication range can also be highly reduced in the context of the blockage. As the validation of the implemented 5G PHY processing blocks and the channel models is performed, these communication chains can be used to run simulations for further studies.

Chapter 6

Theoretical and Generic Proposal of Multibeam Antenna

6.1 Introduction

Due to the severe propagation loss of electromagnetic waves in mmWave bands, high-gain antenna systems with directional beams are widely deployed in this region of frequencies to improve SNR at the Rx. However, concentrating all energy towards the main propagation path through directional communication eliminates the diversity offered by the multipath, and represents a real risk of sudden interruption of communication in the event of blockage due to the presence of human or vehicle in the beam pointing direction [8]. To traditionally maintain the communication link on-the-move, the directional beam needs to be mechanically or electronically steered. In fact, mechanical beam steering consists in manually turning the antenna to face the direction of interest. This technique of beam steering is effective since the antenna gain is maintained, and there is a flexibility in the steering range [151]. Nevertheless, it is only amenable to static or very slow changing propagation environments due to the limitation in steering speed [152]. To overcome this drawback, electronic steering (or beamforming) antennas are proposed for allowing fast beam pointing. However, the feed network and electronic constraints are complex and costly in mmWave bands [153]-[154]. In addition, a large number of antennas is required to enhance the system directivity.

To cope with the above shortcomings of both electronic and mechanical beam steering, the multibeam antenna (MBA) approach received much attention. The advantage of the MBA is to be able to have the equivalent of a coverage with a wide beam while having a high gain. Actually, in a such a system, several high gain beams that overlap are generated. This makes it possible to communicate with several users simultaneously. Moreover, the MBA system can be considered as a good compromise in the management of user mobility, and especially the phenomenon of blockage in the mmWave context. At first sight, a large beam can simply be used when the main path is blocked by an obstacle, in order to capture energy from the other multipath components; but in this case, a large amount of transmitted power is lost, and the cell coverage is ineffective. Designing an MBA system that simultaneously points in well-chosen directions can solve this issue: if a path is blocked, others are maintained with an efficient distribution of the power. MBAs generally represent an antenna system capable of simultaneously generating a certain number of concurrent and independent directive beams with a high gain to cover a predefined angular range.

This chapter discusses a generic approach proposal for modelling MBA systems for performance prediction characterized by scan loss and half-power beamwidth. The validation with the existing models is carried out. Using the proposed antenna model, the advantage of MBA to alleviate the impact of human blockage in millimeter-wave bands is highlighted. Communication performance is evaluated in terms of BLER through the implementation of the 5G physical communication chain in a simulation tool.

For the rest, the chapter is organized as follows. In section 6.2, a brief description of MBA systems is given. Section 6.3 is devoted to the description of the proposed MBA and the input parameters as well as the study assumptions. In section 6.4, the application and validation of the model are presented. Simulation results from the link level evaluation in the context of blockage are given in section 6.5. And finally, the conclusion of the chapter is drawn in section 6.6.

6.2 Multibeam Antenna Systems

6.2.1 Multibeam Technique

Typically, MBA systems are made up of a finite number of input ports, each connected to an antenna called feed antenna. The excitation of each port allows to control a single beam pointing at a predefined direction. Multiple beams pointing in different directions can be transmitted simultaneously from a shared aperture to cover a certain angular range when several ports are excited. This means that such a system has a prefixed number of beams once it is manufactured.

An illustration of the working technique is given in Fig. 6.1 where $\Delta\theta$ represents the angular sector which is covered by a set of beams, each one pointing in a direction θ_b with respect to the axis. This means that in this context, beams must overlap in order to avoid uncovered space.

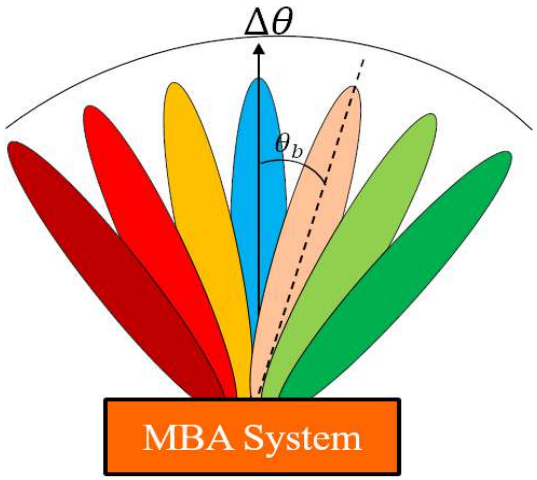

Figure 6.1: Illustration of multibeam technique.

In the same way, if the width of each beam is very small, a significant number of beams is required, hence a high complexity of the communication system. However, if the beams

are very wide, the directivity of the antenna system becomes low, which is not suitable for mmWave communications. Therefore, in the design and realization of MBA systems, a good compromise is necessary between the complexity of the system which depends on the number of beams and the directivity which depends on the beamwidth.

6.2.2 Multibeam Antenna vs Single Beam Antenna

Compared to a single beam antenna (SBA), MBA communication systems prevent communication disruption as part of a user mobility and blockage event. Likewise, the beam training delay can be avoided. In fact, using a SBA system, the communication link can be lost due to the high mobility of the user or the presence of a person (or a vehicle) in the beam direction. To re-establish communication, a beam training process is required. Nevertheless, with MBAs, the communication link can be maintained through the simultaneous application of different beams. In other words, if the communication beam is blocked by a person or lost due to the user mobility, the remaining beams allow the communication to be maintained.

Furthermore, MBAs can also be used to simply send independent data streams as claimed by Quyen and Vu in [156]. Compared to the logical streams that are formed after the channel matrix in the MIMO system, physical streams are created where each stream is associated with a single beam of MBA. In addition, if the beams used in this case do not overlap, no signal processing is necessary to cancel the interference between the transmitted streams. Therefore, multiple users can also be simultaneously served by the base station.

6.2.3 Types of MBA Systems

To realize an MBA system, several typical approaches have been employed. One approach is to use multiple feed antennas placed at different positions in front of a reflectarray (RA). Another technique is to illuminate one side of a lens or transmitarray (TA) by the incident waves emitted by the feed antennas, while the other side is used to focus the radiations in the desired directions. In contrast to RA and TA techniques based on optic principle, MBA design can also be achieved using beamforming circuits such as Butler matrix that can be integrated with an array of antennas into a single substrate. In this section of the chapter, these MBA technologies are briefly reviewed.

Transmitarray-based MBA

Similar to conventional dielectric lens, the TA or phase-shifting surface (PSS) is a structure able to focus electromagnetic radiation from a source antenna in the intended direction with a high gain. As illustrated in Fig. 6.2 reproduced from[150], the TA is composed of an array of unit-cells illuminated by one or more feeds known as focal sources located at the distance F from the TA. By properly positioning the feed antennas behind the planar lens, multiple independent and controllable directive beams can be simultaneously generated as explained in [158]. Each unit-cell of the TA contains two thin surfaces connected through phase-shifters, one working in receive mode and the second in transmit mode. In this way, TAs represent structures able to convert the spherical incident wave from the source antenna to a plane wave by inserting delay lines between the two surfaces of the lens [150] thanks to the proper design of phase-shifters.

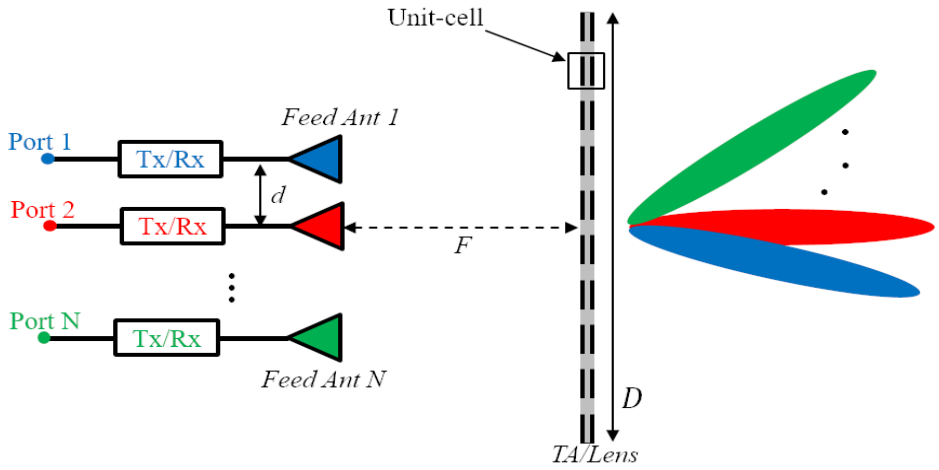

Figure 6.2: Schematic view of the TA-based MBA.

In fact, TA systems are categorized into two groups, i.e fixed and reconfigurable TAs. In the fixed architecture, the unit-cells are physically scaled in order to achieve the required phase distribution. This can be realized by discretizing the surface of the transmitarray into several zone plates [159]. In the case of reconfigurable TA, the phase distribution applied at the unit-cells level is electronically controlled through the active components (PIN diodes, amplifiers, etc.) to steer the plane wave direction [150]-[160]. Even if this latter system is flexible, faster and more accurate than the fixed TA with the low insertion loss, it requires a large number of electronic components, which increases the system cost [157].

Reflectarray-based MBA

Due to the revolutionary breakthrough of printed circuit technology, planar RA antenna systems with low profile, low cost, low weight and high gain have been developed to replace conventional curved reflectors [150]-[163]. An illustration of the working principle of such a technology is given in Fig. 6.3 reproduced from [150].

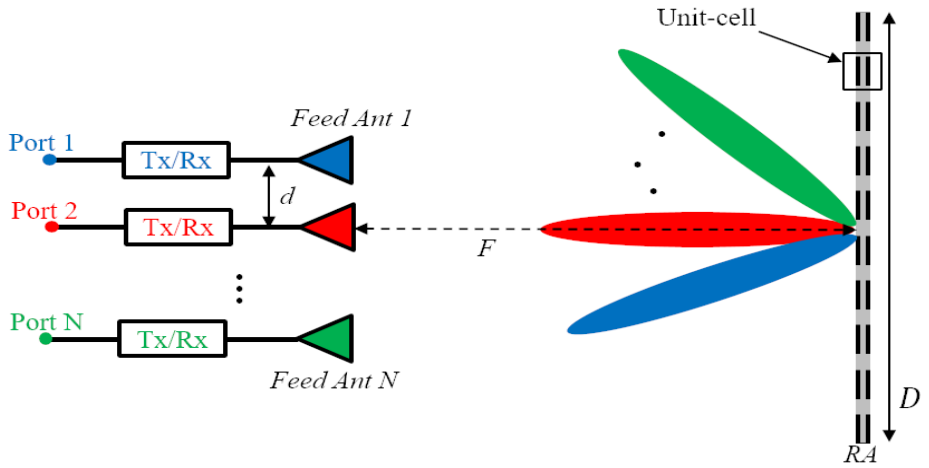

Figure 6.3: Schematic view of the RA-based MBA.

They combine many favorable features of both reflectors and printed arrays. In fact, the RA system is also composed of a set of unit-cells backed by a ground plane so that incident waves from one or more feed antennas are reflected and emitted in the desired beams directions. Unlike TAs, RAs can potentially suffer from the blockage effect of the feed antennas.

MBA based on Beamforming Circuits

In the context of beamforming circuits, the MBA system consists in two parts: *the beamforming network* and *the radiating elements* as illustrated in Fig. 6.4 where the beamforming network is represented by the $N \times N$ Butler or Blass matrix.

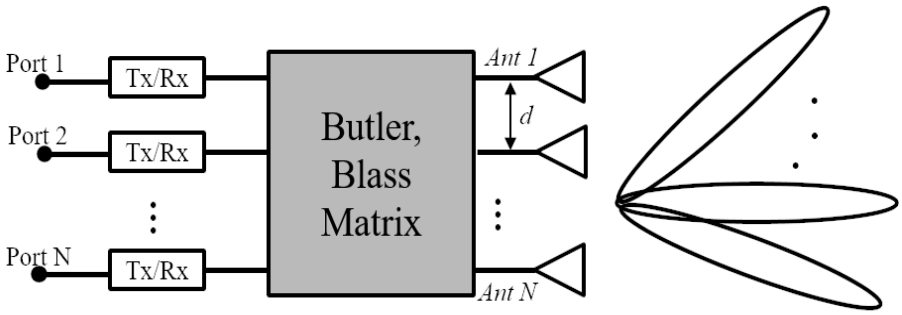

Figure 6.4: MBA architecture using beamforming circuit.

Actually, the Butler matrix is the most well-known beamforming circuit used to control the direction of a beam. To simultaneously generate N beams, the N inputs of the Butler matrix must be activated. A typical Butler matrix is simply composed of fixed phase shifters, crossovers and hybrid couplers [164]. Nowadays, much research efforts have been carried out in developing miniaturized Butler matrices based on substrate-integrated waveguide (SIW) technology especially in mmWave bands, due to the planar, low-cost and low-loss properties of SIWs [150].

Regarding the Blass matrix, it consists in two sets, referred as rows and columns, that are interconnected at each crossover by a directional coupler [165]. The input signals are propagated along the corresponding feed lines which are terminated on a matched load to avoid signal reflections. At each crossover, a portion of the signal is coupled into the corresponding column, thus exciting the concerned radiating element [166].

6.2.4 Characterization of MBA Performance

In general, the MBA performance is characterized by the scan range which leads to the definition of scan loss (SL). The scan range simply defines the angular sector that can be covered by the MBA system as illustrated in section 6.2.1. In the same way, the scan angle represents the beam direction with respect to the antenna broadside, i.e the direction of maximum radiation. In fact, the SL can be defined as the decrease in gain of beam according to the scan angle. This is due to the fact that the effective area of the radiating aperture decreases when the scan angle increases. Other parameters such as aperture efficiency, sidelobe level (SLL), beamwidth can also be used for the MBA performance analysis.

6.3 Multibeam Antenna Modelling

Antenna modelling is one of the main features of global wireless channel modelling. Basically, the idea behind this modelling is to come up with mathematical expressions that represent the radiation patterns of MBA systems. To this end, in this section, different mathematical models proposed in the literature are first reviewed. Additionally, the limitations of these models are highlighted regarding the MBA requirements. To cope with these limiting factors, a generic and complete model is finally proposed.

6.3.1 Review of Standard Models

In the modelling of channels by standardization bodies, several models of the antenna radiation pattern are defined in the technical specifications. In the modelling principle, the essential properties of the radiation of antennas in the real world are taken into account. Therefore, in order to consider the propagation in the mmWave context where directive antennas are used, the Gaussian profile in linear scale or parabolic profile in dB units is generally used in 3D as [19],

$$G(\theta,\phi) = G_0 \exp\left(-\alpha(\theta-\theta_0)^2\right)\exp\left(-\beta(\phi-\phi_0)^2\right), \tag{6.1}$$

where G_0 is the antenna gain in the beam direction (θ_0, ϕ_0). θ and ϕ define the angles in elevation and azimuth planes, respectively. α and β represent the scaling factors which depend on the elevation and azimuth beamwidths, respectively.

Assuming that the radiation patterns in elevation and azimuth are not dependent, the parameter α can be expressed as,

$$\alpha = \frac{2.773}{\theta^2_{-3dB}}, \tag{6.2}$$

with θ_{-3dB} the elevation half-power beamwidth (HPBW). Similarly, β is defined by,

$$\beta = \frac{2.773}{\phi^2_{-3dB}}, \tag{6.3}$$

where ϕ_{-3dB} the azimuth HPBW. From (6.1), (6.2) and (6.3), $G(\theta,\phi)$ can be rewritten in dB units through,

$$G(\theta,\phi)_{dB} = G_{0_{dB}} - \left\{12\left(\frac{\theta-\theta_0}{\theta_{-3dB}}\right)^2 + 12\left(\frac{\phi-\phi_0}{\phi_{-3dB}}\right)^2\right\}. \tag{6.4}$$

As claimed in [19]-[170], the Gaussian profile is a simple mathematical model which suits to the main lobe function. Then, a constant value defining an average SLL can simply be applied.

The Gaussian models proposed by standardization bodies are summarized in Table 6.1. In fact, the gain G_0 is a function of the wavelength λ, the antenna efficiency η and the antenna aperture A_a for the model proposed in the MiWEBA project. With the IEEE 802.15 model, G_0 is a function of θ_{-3dB}.

Table 6.1: Gaussian based models

Reference	Vertical cut of $G(\theta,\phi)_{dB}$	Horizontal cut of $G(\theta,\phi)_{dB}$	HPBW	G_0
3GPP [66]	$-min\left\{12\left(\frac{\theta-90^\circ}{\theta_{-3dB}}\right)^2, 30\right\}$	$-min\left\{12\left(\frac{\phi}{\phi_{-3dB}}\right)^2, 30\right\}$	$\theta_{-3dB}=65^\circ$ $\phi_{-3dB}=65^\circ$	8 dBi
ITU-R [171]	$-min\left\{12\left(\frac{\theta-\theta_0}{\theta_{-3dB}}\right)^2, 20\right\}$, $82.5^\circ \leq \theta_0 \leq 97.5^\circ$	$-min\left\{12\left(\frac{\phi}{\phi_{-3dB}}\right)^2, 20\right\}$	$\theta_{-3dB}=15^\circ$ $\phi_{-3dB}=70^\circ$	17 dBi
MiWEBA [19]	$-min\left\{12\left(\frac{\theta-90^\circ}{\theta_{-3dB}}\right)^2, 20\right\}$	$-min\left\{12\left(\frac{\phi}{\phi_{-3dB}}\right)^2, 20\right\}$	Not fixed	$f(\lambda,\eta,A_a)$
IEEE 802.15 [170]	$-12\left(\frac{\theta-90^\circ}{\theta_{-3dB}}\right)^2$	0	$\theta_{-3dB} \leq 80^\circ$	$f(\theta_{-3dB})$

6.3.2 Limitations of Standard Models

The radiation models proposed by standards and other collaborative projects in channel modelling have certain limitations regarding the requirements of the MBA system.

Apart from the model proposed in the MiWEBA project, the HPBW values are fixed for all radiation patterns. Actually, when the beam starts to move away from the antenna broadside (or antenna axis), the beamwidth tends to widen depending on the pointing direction.

Furthermore, all the proposed models are also static, in particular in the azimuth plane where the radiation pattern points towards the x-axis, $\phi_0 = 0$. In the elevation plane, the direction of the radiation pattern is fixed at $\theta_0 = 90^\circ$ except in the ITU-R model for which the pointing direction varies from 82.5° to 97.5°. This means that assuming 0 and 90° represent the antenna broadside direction, another radiation pattern pointing in another direction cannot be generated in the context of MBA.

Moreover, although the ITU-R model can be exploited in the elevation plane, the scan range remains very low, i.e the beams cannot point towards the propagation paths whose directions are outside the range of ±7.5° around 90°. In addition, the model does not include the scan loss due to the antenna gain being kept constant.

6.3.3 Multibeam Antenna Model Proposal

To cope with the limiting factors of the previous models, we proposed a generic and complete approach that almost includes the essential features of MBA systems. The proposed model is flexible due to the fact that the antenna broadside is not fixed. It is also realistic in the sense that the beamwidth degradation and the scan loss as previously mentioned are taken into account. To this purpose, the validation with some existing MBAs is achieved.

Study Assumptions and General Expression

In the development of the MBA model, some assumptions were taken into account. First of all, based on the RA and TA structures, we generally consider the MBA system as a two-dimensional planar aperture antenna illustrated in Fig. 6.5.

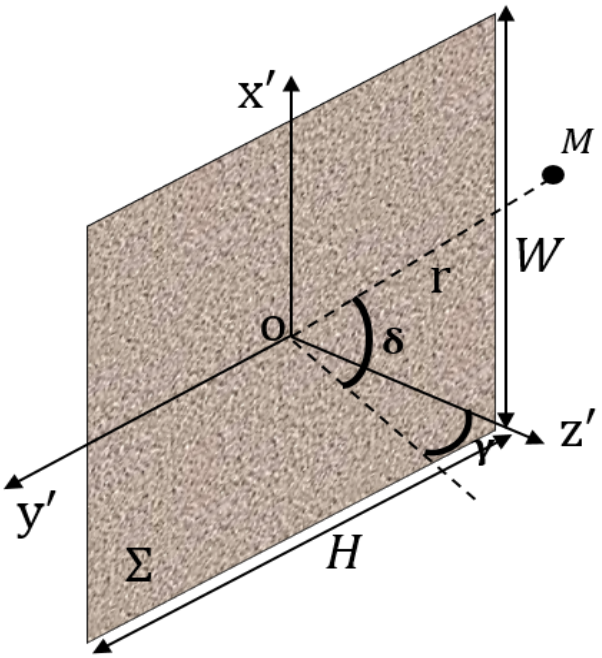

Figure 6.5: Aperture representation with coordinate system.

Like, the previous models, we assume that the radiation in both perpendicular plans x'oz' and y'oz' are not dependent, and the waves on the antenna aperture are in phase due to the phase correction performed by the unit-cells of the RAs and TAs. In this case, only the amplitude distribution of the field is considered, from which the radiation pattern at the antenna broadside is defined. And then, assuming that each of the feed antennas illuminates the center of the radiating surface, the beams or radiation patterns in the directions other than the antenna broadside are deduced using the surface projection.

Consequently, the general expression of the antenna gain pattern for the desired pointing direction (θ_0, ϕ_0) with the respect to the antenna broadside is given by,

$$G(\theta, \phi) = \left(\frac{G_0}{SL(\theta_0, \phi_0)} \right) g(\theta - \theta_0, \phi - \phi_0), \tag{6.5}$$

where θ and ϕ represent the angles of elevation and azimuth, respectively. G_0 is the antenna gain at broadside, $SL(\theta_0, \phi_0) = SL(\theta_0) SL(\phi_0)$ defines the scan loss value in the beam direction (θ_0, ϕ_0) and $g(\theta - \theta_0, \phi - \phi_0)$ is the normalized gain radiation pattern. The scan loss SL is referenced to the antenna broadside.

Antenna Gain at Broadside

To reduce the complexity of the calculation of the antenna directivity, several approximate expressions are proposed in the literature, among which the Kraus formula given by [173],

$$D_0 \approx \frac{41253}{\theta_{HPBW_0} \cdot \phi_{HPBW_0}}, \tag{6.6}$$

is suitable for antenna systems with narrow beams and very low SLLs. θ_{HPBW_0} and ϕ_{HPBW_0} represent the HPBWs at the antenna broadside in elevation and azimuth, respectively.

D_0 is the antenna broadside directivity from which the gain G_0 is naturally defined by,

$$G_0 = \eta D_0, \tag{6.7}$$

with η the antenna efficiency.

Broadside Normalized Radiation Pattern

From Fig. 6.5, the complex amplitude of the field on the aperture surface Σ can be expressed by,

$$E_a\left(x', y'\right) = E\left(x', y'\right) e^{j\phi_E(x', y')}, \tag{6.8}$$

where E and ϕ_E represent the amplitude and the phase of E_a depending on the coordinates x' and y'. The electric field radiated in Fraunhofer region (or far zone) is given by Goudet's formula [177],

$$E\left(r, \delta, \gamma\right) = j\zeta \left[\frac{cos\left(\delta\right) + cos\left(\gamma\right)}{2}\right] \iint_{\Sigma} E\left(x', y'\right) e^{j\phi_E(x', y')} e^{jk_0(x' sin(\delta) + y' cos(\delta) sin(\gamma))} dx' dy', \tag{6.9}$$

with ζ expressed by,

$$\zeta = \frac{e^{-jk_0 r}}{\lambda r}. \tag{6.10}$$

r, δ, γ represent the polar coordinates at the observation point, and k_0 is the wave number.

Assuming on the one hand that waves are in phase on the aperture as justified in section 6.3.3, i.e $\phi_E\left(x', y'\right) = 0$, and on the other hand, the radiation in both perpendicular plans **E** and **H** are not dependent, the electric field in (6.9) can be rewritten as,

$$E\left(r, \delta, \gamma\right) = E^E\left(r, \delta\right) E^H\left(r, \gamma\right), \tag{6.11}$$

where $E^E\left(r, \delta\right)$ and $E^H\left(r, \gamma\right)$ define the fields in plans **E** and **H**, respectively; and they are expressed by,

$$E^H\left(r, \gamma\right) = j\zeta \left[\frac{1 + cos\left(\gamma\right)}{2}\right] \int_H E_y\left(y'\right) e^{jk_0 y' sin(\gamma)} dy', \tag{6.12}$$

and,

$$E^E\left(r, \delta\right) = j\zeta \left[\frac{1 + cos\left(\delta\right)}{2}\right] \int_W E_x\left(x'\right) e^{jk_0 x' sin(\delta)} dx'. \tag{6.13}$$

From (6.11), one can deduce the field radiation pattern $A\left(\theta, \phi\right)$ as follows,

$$A\left(\theta, \phi\right) = A\left(\theta\right) A\left(\phi\right), \tag{6.14}$$

with $A\left(\theta\right)$ the field radiation in **E** plan and the expression is derived from (6.12) by replacing γ by θ and $A\left(\phi\right)$ the field radiation in **H** plan derived from (6.13) by replacing δ by ϕ. $A\left(\theta\right)$ and $A\left(\phi\right)$ are defined by (6.15) and (6.16), respectively.

$$\begin{aligned} A\left(\theta\right) &= \frac{1 + cos\left(\theta\right)}{2} \int_H E_y\left(y'\right) e^{jk_0 y' sin(\theta)} dy' \\ &= \frac{1 + cos\left(\theta\right)}{2} SF\left(\theta, H, \lambda\right). \end{aligned} \tag{6.15}$$

$$A(\phi) = \frac{1+cos(\phi)}{2}\int_W E_x(x')\, e^{jk_0 x' sin(\phi)} dx' = \frac{1+cos(\phi)}{2} SF(\phi, W, \lambda). \quad (6.16)$$

With $SF(\psi, h, \lambda) = \int_h E_w(w')\, e^{jk_0 w' sin\psi} dw'$, one can note that from (6.15) and (6.16), the field radiation pattern is the spatial Fourier transform $SF(\psi, h, \lambda)$ of the field distribution multiplied by the factor $\frac{1+cos(\psi)}{2}$, with $\psi = \theta$ and $h = H$ for $A(\theta)$ and $\psi = \phi$ and $h = W$ for $A(\phi)$.

By considering the narrow-beam approximation since the beginning, radiation characteristics for four field distributions [174] are summarized in Table 6.2. For the determination

Table 6.2: Radiation characteristics depending on the field distribution

Aperture Distribution	Graphical Representation	Function E_w $-\frac{h}{2} \leq w' \leq \frac{h}{2}$	$SF(u)$, $u = \frac{\pi h}{\lambda} sin(\psi)$	HPBW (°)	SLL (dB)
Uniform	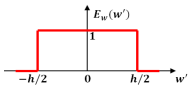	1	$\frac{sin(u)}{u}$	$51\frac{\lambda}{h}$	−13.2
Triangular	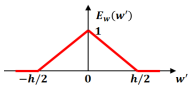	$1 - 2\frac{w'}{h}$	$4\left(\frac{sin(u/2)}{u}\right)^2$	$73.4\frac{\lambda}{h}$	−26.4
Cosine	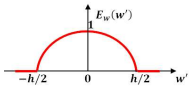	$cos\left(\frac{\pi w'}{h}\right)$	$\frac{(\pi/2)^2 cos(u)}{(\pi/2)^2 - u^2}$	$68.8\frac{\lambda}{h}$	−23.2
Cosine-Squared	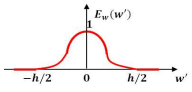	$cos^2\left(\frac{\pi w'}{h}\right)$	$\frac{sin(u)}{(1-(u/\pi)^2)u}$	$83.2\frac{\lambda}{h}$	−31.5

of the normalized radiation pattern at the antenna broadside $g(\theta, \phi)$, the Poynting vector modulus is considered, which leads in dB units to,

$$g(\theta, \phi) = 20\log_{10}(|A(\theta, \phi)|). \quad (6.17)$$

As mentioned before for the centre beam, $A(\theta)$ and $A(\phi)$ are calculated by selecting from Table 6.2 the distribution with a broadside HPBW closest to the realistic MBA used as reference model. In fact, it can be noted that the choice of the distribution in the modelling has a very low impact on the performance of the system, in particular the HPBW.

Nonetheless, in the context of the definition of the angles according to 3GPP in Chapter 3, θ must be replaced by $\frac{\pi}{2} - \theta$.

Multibeam Aspect and Scan Loss

The normalized radiation pattern in the direction (θ_0, ϕ_0) is first obtained by replacing θ and ϕ by $\theta - \theta_0$ and $\phi - \phi_0$ in the previous expressions, especially in (6.17). And then the aperture size H must be replaced by the equivalent size $H_{equiv} = H \cdot cos(\theta_0)$ in elevation and W by $W_{equiv} = W \cdot cos(\phi_0)$ in azimuth due to the projected area reduction which is estimated by a cosine reduction of effective aperture surface for the beam directions θ_0 and ϕ_0 [169]. In this way, the beamwidths corresponding to these scan angles increase and

are characterized through the HPBW in elevation by,

$$\theta_{HPBW}(\theta_0) = \frac{\theta_{HPBW_0}}{cos(\theta_0)}, \tag{6.18}$$

and in azimuth by,

$$\phi_{HPBW}(\phi_0) = \frac{\phi_{HPBW_0}}{cos(\phi_0)}. \tag{6.19}$$

As the beams are scanned in both perpendicular plans independently, the scan loss in the beam direction in elevation θ_0 can be approximated in dB units by,

$$SL(\theta_0) = -20\log_{10}(|cos(\theta_0)|). \tag{6.20}$$

Likewise, if the scan is performed in the azimuth plane, the scan loss is defined by,

$$SL(\phi_0) = -20\log_{10}(|cos(\phi_0)|). \tag{6.21}$$

With the above expressions, it can be noted that the SL does not depend on the frequency and dimensions of the antenna unlike HPBWs.

6.4 Application and Validation of the Model

The purpose of this section is to highlight the application of the proposed method for the generation of beams, and the performance comparison in terms of beamwidth and scan loss with some existing MBA systems in the context of validation. To this end, parameters such as frequency, aperture dimensions, antenna efficiency and field amplitude distribution on the antenna aperture are required.

6.4.1 Application Procedure

According to the principle described in section 6.3.3, the beam in a given direction θ_0 in elevation and ϕ_0 in azimuth is characterized by a gain $G_0(\theta_0, \phi_0)$ and the corresponding normalized radiation pattern $g(\theta - \theta_0, \phi - \phi_0)$. Actually, based on (6.5), $G_0(\theta_0, \phi_0)$ is given by,

$$G_0(\theta_0, \phi_0) = \frac{G_0}{SL(\theta_0, \phi_0)}. \tag{6.22}$$

Using the parameters of the TA prototype of Fig. 6.6 realized by Pham *et al.* [178], a collection of beam patterns for various pointing directions is given in Fig. 6.7 in which, the tilted beams are normalized to the maximum gain value G_0 defined at the antenna broadside. In fact, Pham's bifocal TA is composed of a squared surface of dimension $D = 50\,mm$ with 20×20 unit-cells at 60 GHz. The measurement results revealed a HPBW of 8.2° in both planes in the boresight. From these results, the closest HPBW is 8.32° calculated according to Table 6.2, which leads to assume that the distribution of the field on the TA aperture could be considered as cosine-squared. Thus, the centre normalized radiation pattern is given in elevation by,

$$g(\theta) = \left| \frac{1 + cos(\theta)}{2} \frac{sin(u)}{\left(1 - (u/\pi)^2\right) u} \right|^2, \tag{6.23}$$

and in azimuth by,

$$g(\phi) = \left| \frac{1 + cos(\phi)}{2} \frac{sin(v)}{\left(1 - (v/\pi)^2\right) v} \right|^2, \tag{6.24}$$

with the angle coordinates $u = \frac{\pi D}{\lambda} sin(\theta)$ and $v = \frac{\pi D}{\lambda} sin(\phi)$. The beams given in Fig. 6.7 are finally generated using (6.23) and (6.24) for 100° (from −50° to +50°) scan range.

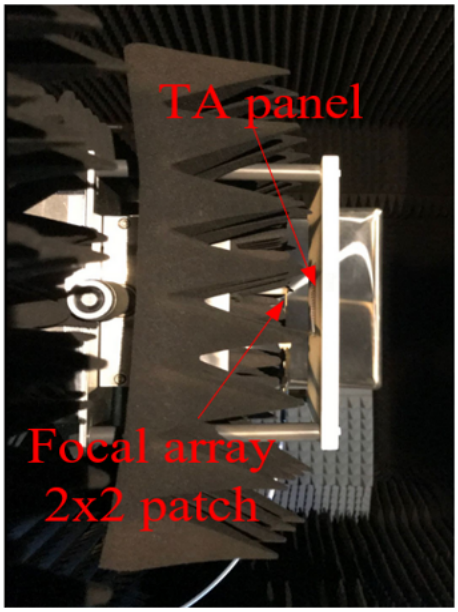

Figure 6.6: Pham *et al.* TA prototype at 60 GHz [178].

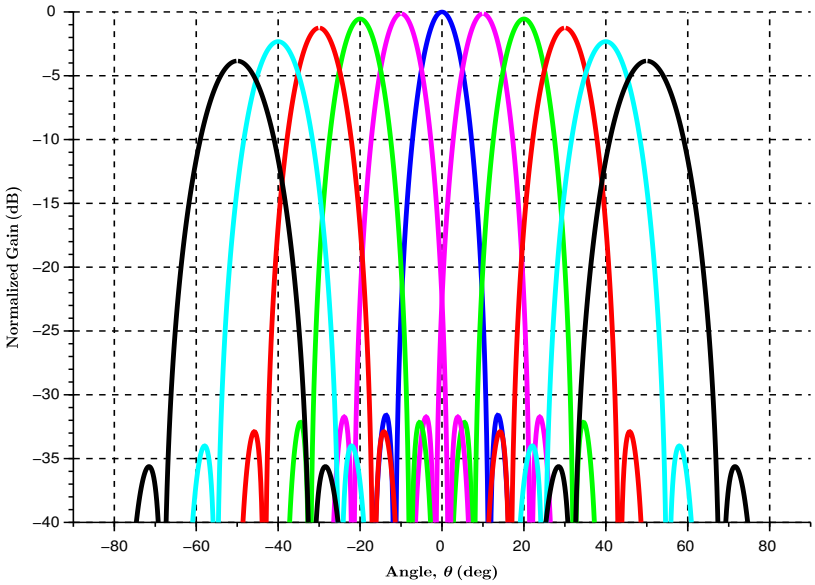

Figure 6.7: Normalized beam patterns in elevation at 60 GHz.

The application of the proposed model is described by the algorithm summarized in Fig. 6.8.

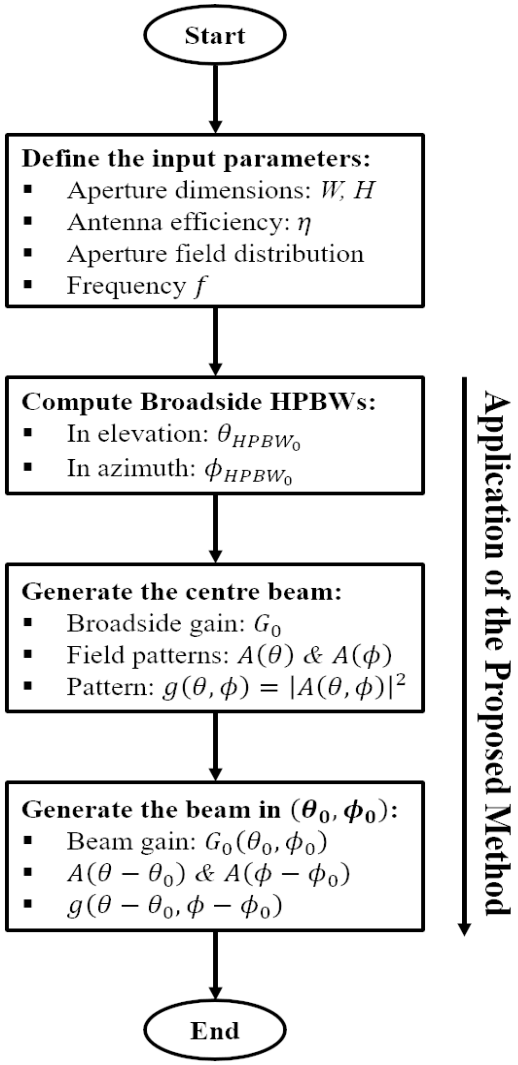

Figure 6.8: Application of the proposed model.

6.4.2 Validation of the Model

In the validation procedure of the proposed antenna model, several existing MBAs realized in different frequency bands were used. In this report, performance comparisons at X-, Ku-, Ka- and V-bands are highlighted. As previously mentioned, the characterization parameters such as beamwidth and scan loss are only taken into account in our study.

Performance Validation with TA-based MBAs

Here, the performance comparison is performed with the MBA physically realized in X-, Ka- and V-bands by Clemente *et al.* [181], Di Palma *et al.* [157] and Pham *et al.* [178], respectively.

Validation at X-band:

The prototype of the electronically reconfigurable TA realized by Clemente *et al.* is shown in Fig. 6.9. The prototype is composed of a squared surface of dimension 300 mm at 9.8 GHz and a boresight HPBW of 6.1° is achieved.

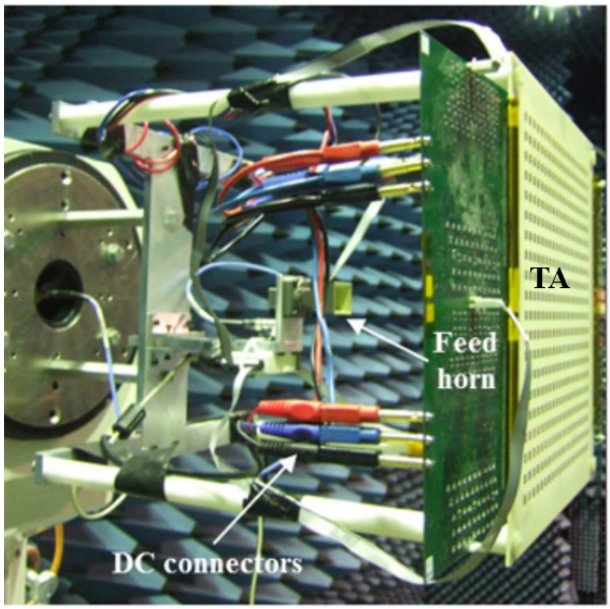

Figure 6.9: Clemente *et al.* TA prototype at 9.8 GHz [181].

For comparison with the prototype realized by Clemente *et al.*, the cosine aperture distribution was assumed.

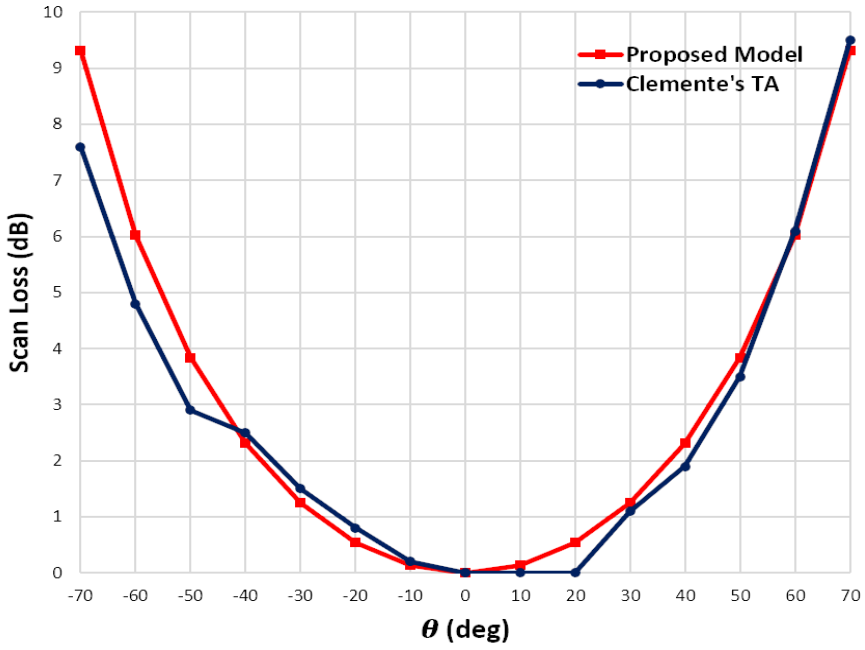

Figure 6.10: Scan loss performance at 9.8 GHz.

Fig. 6.10 shows the scan losses with respect to the directions of the beams. A quite good agreement can be noticed between the proposed model which can be seen as a prediction model and the measurement results performed by Clemente *et al.* for a scan range of ±70° off broadside.

In Fig. 6.11, the beamwidth comparison is highlighted for the same scan range. Similar performance is achieved for beams pointing at ±50° around the boresight (or broadside). However, outside the ±50° angular region, the discrepancies become significant. This can be due to the loss of hardware components, in particular for high scan angles.

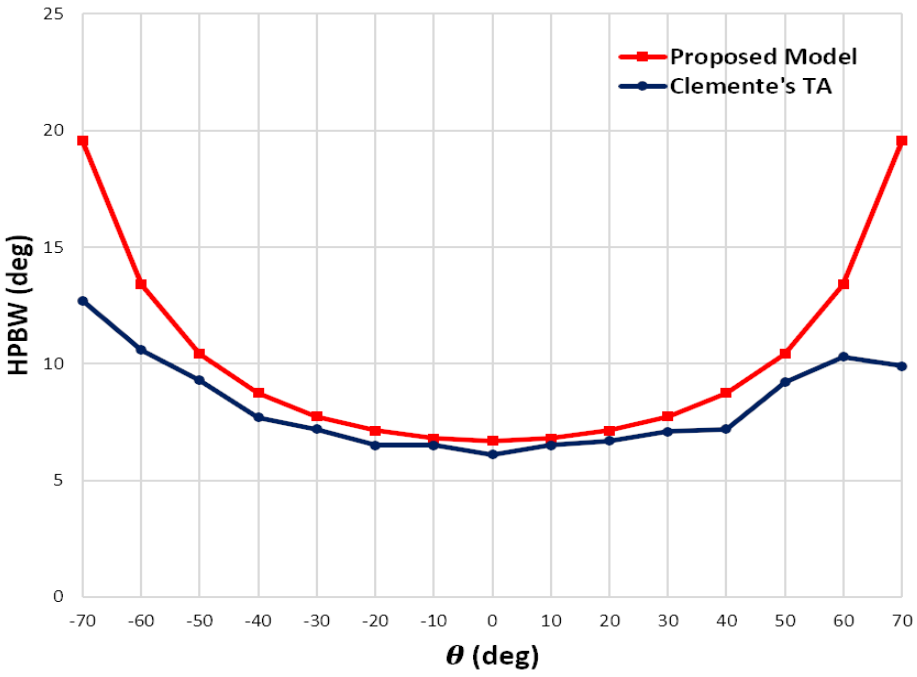

Figure 6.11: HPBW performance at 9.8 GHz.

Validation at Ka- and V-bands:

For the performance validation in these frequency bands, the prototypes shown in Figs. 6.6 and 6.12, and realized at 60 GHz and at 29 GHz by Pham *et al.* [178] and Di Palma *et al.* [157] are used.

For comparison with Di Palma's electronically reconfigurable TA, which is composed of a squared surface of dimension ≈ 100 mm and a boresight HPBW=7.5°, the cosine aperture distribution is also applied. With these parameters, a performance comparison is performed as follows. Fig. 6.13 shows the scan loss with respect to the directions of the beams. Similar performance can be noted between the proposed model and the measurement results performed by Di Palma *et al.* for a scan range of ±60° off broadside. Comparing the proposed model with Pham's bifocal TA measurements, scan losses are also similar for a scan range of ±40° around the antenna broadside and a difference of about 1.5 dB at ±45°. Outside the ±45° angular sector, the discrepancies become significant. This may be justified by the spill-over radiation and hardware component loss that are not taken into account in the proposed prediction model. In fact, the spill-over is the power radiated by the feed antenna which does not illuminate any element of the array of

unit-cells [168].

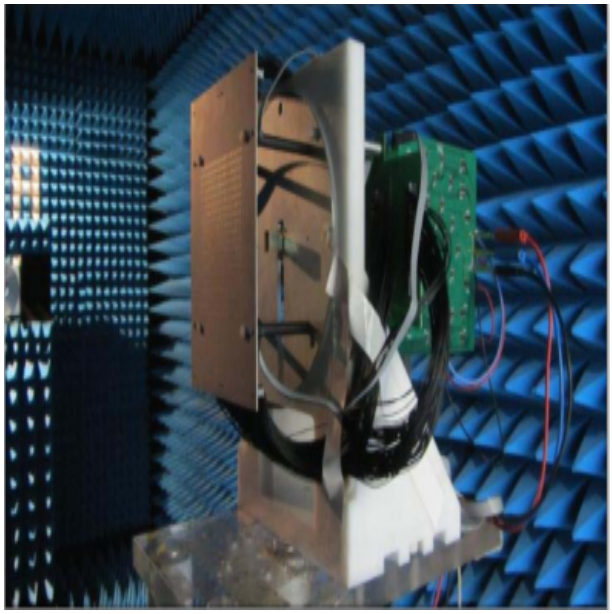

Figure 6.12: Di Palma *et al.* TA prototype at 29 GHz [157].

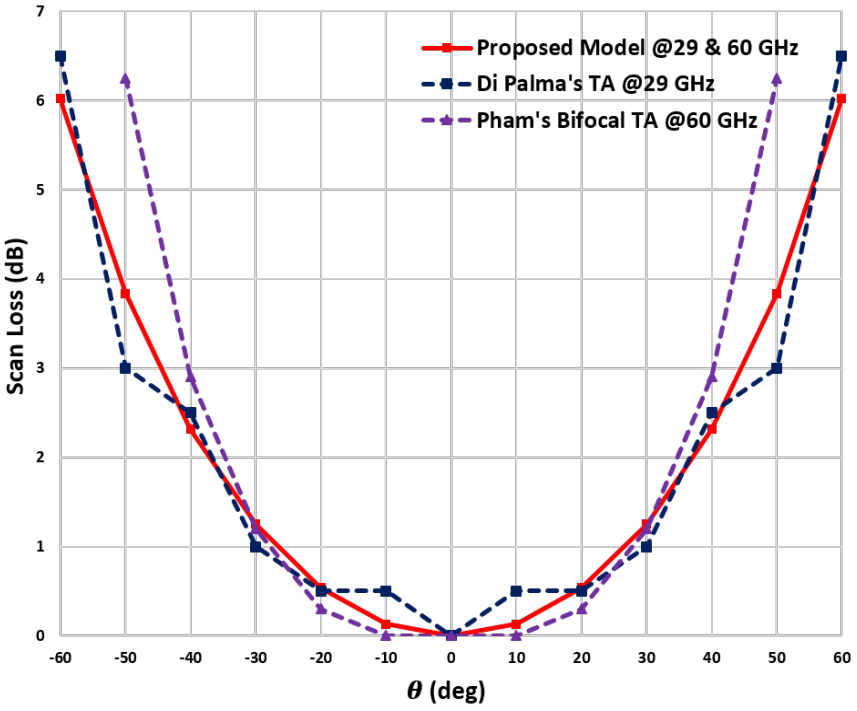

Figure 6.13: Scan loss performance at 29 and 60 GHz.

In Fig. 6.14, the beamwidth comparison is given. Indeed, the beamwidths degrade in the same way, in particular for directions varying from $-60°$ to $+60°$ at 29 GHz. However, at 60 GHz, some differences can be noted from $\pm 35°$ with the Pham's prototype due to the same reasons mentioned above.

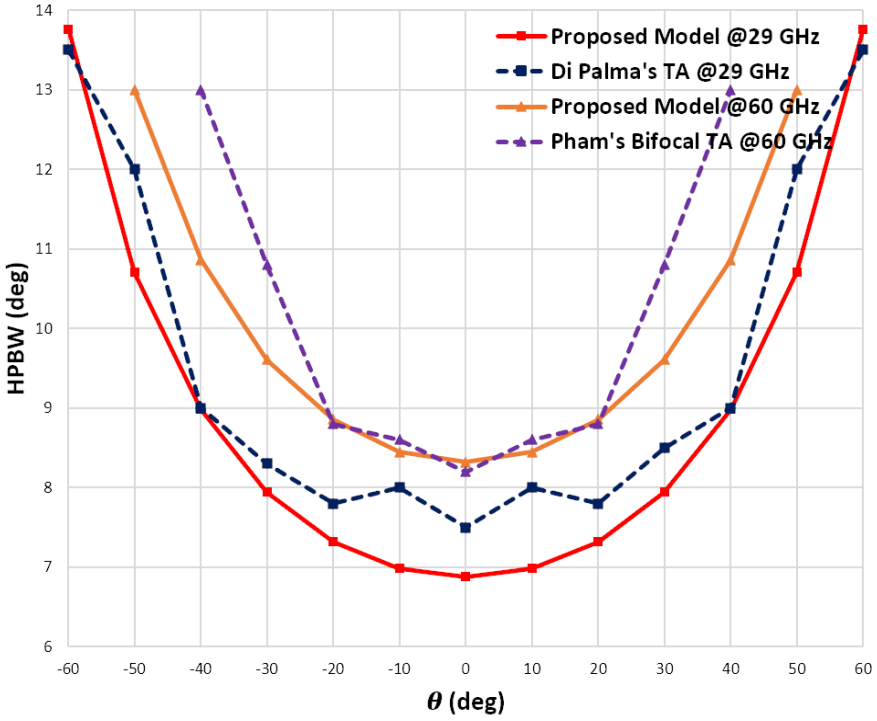

Figure 6.14: Beamwidth performance at 29 and 60 GHz.

Performance Validation with RA-based MBA

In this section, a validation of the proposed model with the RA-based MBA realized by Yang *et al.* [182] is performed. The prototype of this MBA at 11.1 and 14.3 GHz is given in Fig. 6.15.

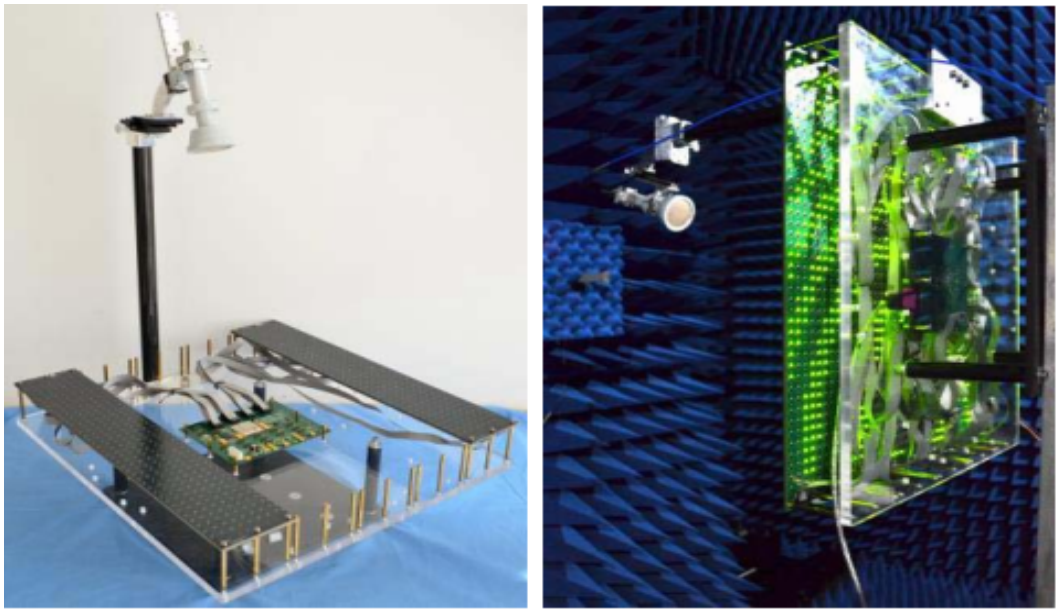

Figure 6.15: Yang *et al.* RA prototype at 11.1 and 14.3 GHz [182].

In fact, the proposed RA is composed of 40×40 unit-cells for an aperture of dimensions $480\,mm \times 480\,mm$, and a broadside HPBW of 2.79° is achieved. Based on this result, a cosine-squared aperture distribution of the electric field is used.

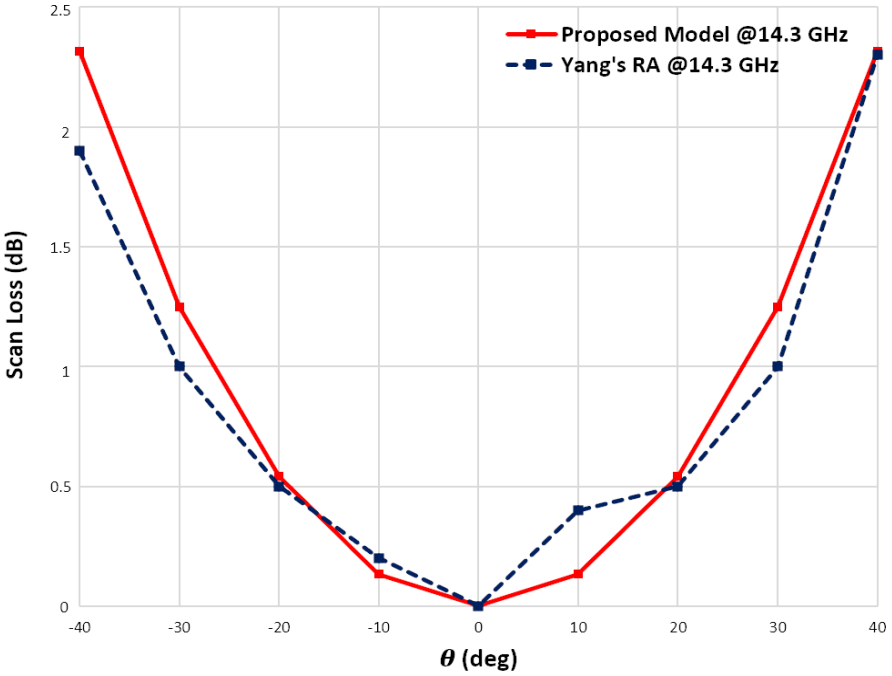

Figure 6.16: Scan loss performance at 14.3 GHz.

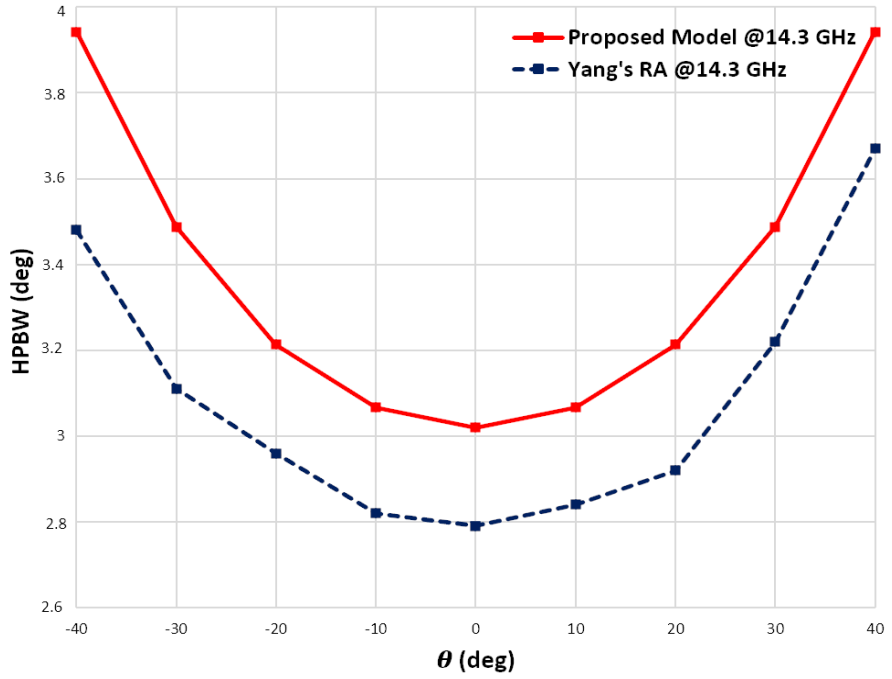

Figure 6.17: Beamwidth performance at 14.3 GHz.

The scan loss comparison at 14.3 GHz with the proposed model is illustrated in Fig. 6.16 where a quite good agreement can be noted from $-40°$ to $+40°$. Likewise, as depicted in Fig. 6.17, the beamwidths also degrades in the same way for the same scan range.

The same trend can also be noticed between our computational model and the measurements conducted by Yang *et al.* using their reconfigurable RA realized in the 11.1 GHz frequency band. Indeed, similar performance in terms of scan loss is performed from $-30°$ to $+30°$, and outside this scan range the discrepancies become considerable with a maximum difference of ≈ 3 dB at $\pm 60°$. According to the authors, these differences are caused by the edge diffraction and fabrication errors in addition to the spill-over radiation, which result in a total maximum loss of 3.48 dB.

6.5 MBA and Blockage Impact Mitigation

In this section, the link level evaluation is performed in order to highlight the advantage of the MBA system using the proposed model in the context of blockage. To this end, Fig. 5.9 of chapter 5 has been used in different simulation contexts in the 60 GHz frequency band. We also remind that the blocker is modelled by a blocking region as mentioned in previous chapters.

6.5.1 Simulation Parameters

The simulation parameters are summarized in Table 6.3. In the scenarios, the proposed MBA is only used at the base station (Tx) with the broadside gain of 20.3 dBi from the parameters of the 60 GHz bifocal TA of Pham *et al.* [178]. An omnidirectional antenna with a 0 dBi gain is used at the user equipment (Rx) level for simplicity.

Table 6.3: Simulation parameters

Parameters	**Values**
Carrier Frequency	60 GHz
Bandwidth	400 MHz
Subcarrier Spacing	120 kHz
Fast Fourier Transform (FFT) Size	4096
Multipath Channel Model	3GPP CDL-C
Human Blockage Model	3GPP NSB
Number of blockers	1
Channel Coding	5G LDPC
Modulation Scheme	64QAM
Code Rate	0.65

For the blocking phenomenon, the non-self-blocking (see chapter 4) which is characterized by the presence of humans or vehicles moving around the user is used. With the highest values of blocking region parameters, i.e $\Delta\theta = 15°$, $\Delta\phi = 45°$ for the angular spaces in azimuth and elevation, respectively, as well as the distance from the blocker to the Rx $r = 2\,m$ [66], an attenuation of 16.1 dB at 60 GHz is deduced.

As explained in chapter 4, the use of multiple beams is advantageous when there are several propagation paths which are not strongly attenuated. Additionally, the performance of the communication could be further improved if the directions of these paths are not far from the antenna broadside. Since we are dealing with the 3GPP CDL channel model, it can be noted that among the proposed models, only the NLOS CDL-C profile

(see chapter 3) is suitable in this context. Although a mmWave link is mainly based on an LOS channel, the use of the CDL-C model in NLOS cannot be ruled out because it has also been defined for mmWave frequencies up to 100 GHz. Furthermore, the studies carried out by Genç *et al.* [4] on the basis of ray tracing simulations showed that the 60 GHz communication link can be maintained by the reflected paths in the absence of the LOS path.

6.5.2 Scenarios of Simulation

Three main scenarios of simulation have been considered: *Scenario 1*, *Scenario 2* and *Scenario 3*. An illustration of these simulation scenarios is given in Fig. 6.18.

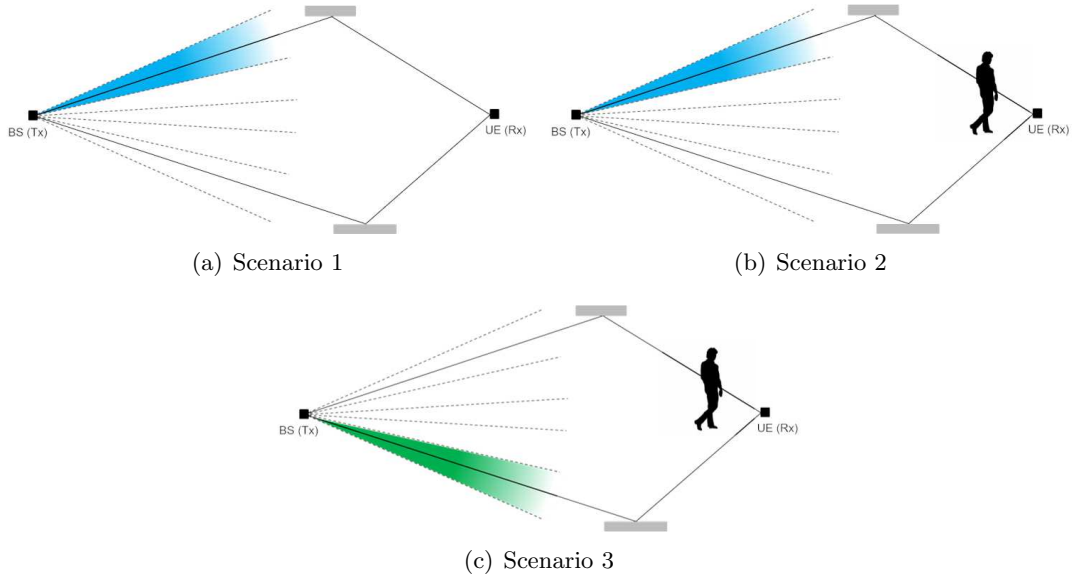

(a) Scenario 1

(b) Scenario 2

(c) Scenario 3

Figure 6.18: Scenarios for link level evaluation.

In fact, in the first scenario, there is no blocker between the Tx and Rx, and a single communication beam is used and steered towards the main propagation path, i.e the path with the first highest channel gain.

The second scenario is exactly scenario 1 with the presence of a human blocker located in the direction of the communication beam.

The third scenario can be seen as the solution to scenario 2 with the application of the multibeam aspect. Since blockage occurred in the direction of the first beam, an additional beam is activated, and points towards the propagation path with the second highest channel gain. In this context, only the signal received through the second beam is processed at the Rx. Nevertheless, MIMO processing could be applied to the signals received from both beams despite the fact that the first one is considerably attenuated by the blocker.

6.5.3 Simulation Results

Multipath Channel Analysis and SNR

Since each path whose angle of arrival is inside the blocking zone is attenuated by 16.1 dB, the idea here is to compare both the non-blocking channel and the blocking channel.

To this purpose, we focused on the computation of SNR_k at the Rx in the context of OFDM modulation where the received signal Y_k on the subcarrier k is defined by,

$$Y_k = H_k S_k + n_k, \tag{6.25}$$

with S_k and H_k representing the transmitted complex symbol and the channel attenuation coefficient, respectively. n_k is a zero mean Gaussian random complex entry with variance σ_N^2. From (6.25), SNR_k can be deduced as,

$$SNR_k = \frac{|H_k|^2 \sigma_S^2}{\sigma_N^2}, \tag{6.26}$$

where σ_S^2 represents the signal power at the Tx. We also define the average $\overline{SNR}$ from (6.26) for the non-blocking channel by,

$$\overline{SNR} = \frac{\sigma_S^2}{\sigma_N^2 N_{SCs}} \sum_{k=1}^{N_{SCs}} |H_k|^2, \tag{6.27}$$

and by,

$$\overline{SNR}_{blocking} = \frac{\sigma_S^2}{\sigma_N^2 N_{SCs}} \sum_{k=1}^{N_{SCs}} \left| H_k^{blocking} \right|^2, \tag{6.28}$$

in the context of blocking channel. N_{SCs} represents the number of subcarriers. By considering the fact that the channel difference is characterized by Δ_{SNR} through,

$$\Delta_{SNR} = \frac{\overline{SNR}}{\overline{SNR}_{blocking}}$$

$$= \frac{\sum_{k=1}^{N_{SCs}} |H_k|^2}{\sum_{k=1}^{N_{SCs}} \left| H_k^{blocking} \right|^2}, \tag{6.29}$$

we show that $\Delta_{SNR} = 16.1$ dB. This means that the non-blocking channel outperforms the blocking channel with a value of SNR equal to 16.1 dB using the simulation parameters.

Link Level Evaluation

In Fig. 6.19, a comparison of the performance in terms of BLER versus SNR of the three scenarios is highlighted for a fixed throughput of 1.5 Gbits/s. This data rate is given by the MCS 15 [54], i.e 64QAM modulation with a code rate of 0.65 for a bandwidth of 400 MHz [60]. Simulation results reveal that to ensure the same 5G eMBB quality of service (QoS), scenario 2 with human blocking in the single beam direction requires a 16 dB increase in SNR with respect to scenario 1 in which there is no human blockage as justified in section 6.5.3. However, we only notice a difference of 2.8 dB between scenario 1 and scenario 3.

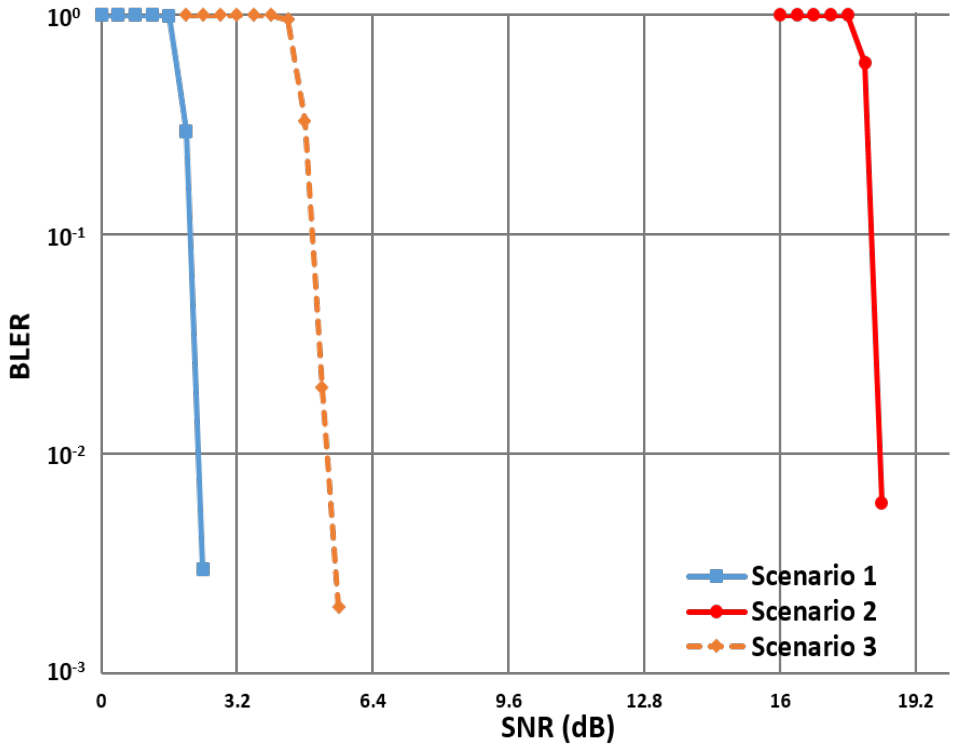

Figure 6.19: Performance under the same throughput.

Indeed, in scenario 3, using an additional beam that points towards the second propagation path when the first beam is blocked, almost guarantees the same QoS with the same SNR values and avoids the link interruption between the Tx and the Rx in some cases where the human attenuation is very high.

With these results, the blockage problem has been analyzed through the SNR variations for a fixed target throughput. Otherwise, similar performance can be achieved in the three scenarios with the same SNR values as shown in Fig. 6.20, with a variation of throughputs as follows. Compared to ideal scenario 1, the communication data rates in scenario 2 should be drastically reduced from 1.5 Gbits/s to 227.9 Mbits/s due to the blockage of the single beam direction. This mitigates the advantage of using mmWaves bands where high data rates are required. In this scenario, MCS 2 is used, i.e QPSK modulation with a code rate of 0.3. Nevertheless, in scenario 3 with the use of an additional second beam at the Tx, an improvement in throughput close to scenario 1 is observed, going from 227.9 Mbits/s to 1.15 Gbits/s in the situation of blockage where MCS 2 is changed for MCS 13 (64QAM with a code rate of 0.55). In other words, the blockage induces a loss of about 85% of the throughput, whereas with the MBA this loss is only 23%.

To sum up, it can be noted that the activation of a secondary beam has made it possible to considerably improve the communication performance in terms of SNR and throughputs in the event of a blocking phenomenon. Actually, this can be justified by the relative powers of the two main propagation paths of the CDL-C channel model. More specifically, adding the 16 dB of human shadowing to the attenuation of the first main path which is 0 dB, the secondary main path with an attenuation of -1.2 dB and which is not blocked becomes better than the first one. In addition, both paths are not far from the broadside

direction which is given by $\phi_0 = 0$ in azimuth and $\theta_0 = 90°$ in elevation.

However, by doing the same analysis with the CDL-E LOS channel model (see chapter 3) where there is only the LOS path with better relative power, the application of multiple beams is very limited if this LOS path is blocked. In fact, apart from the LOS, the rest of the propagation paths are strongly attenuated. Then, they are far from the antenna broadside, which also degrades the gain of the beams in these directions.

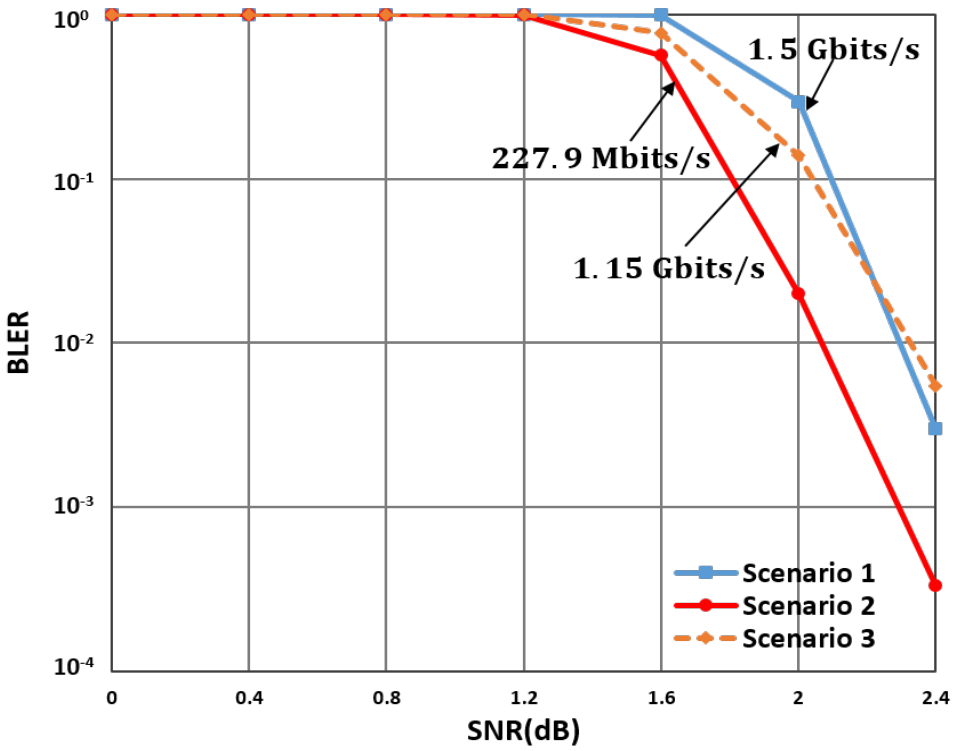

Figure 6.20: Performance with three different throughputs.

6.6 Conclusion

In this chapter, a theoretical and generic approach is proposed for modelling multibeam antenna systems for performance prediction characterized by scan loss and half-power beamwidth. The validation of the proposed model with the existing MBAs in several frequency bands has also been carried out. Simulation results revealed a quite good agreement with existing MBAs in terms of scan loss and beamwidth. However, the discrepancies become significant for the scan angle from $\pm 45°$ off the antenna broadside in certain cases due the increase in the spill-over radiation, fabrication errors and edge diffraction that are not taken into account in our theoretical model. The model is also flexible and can be used in the mmWave channel modelling for simulation purposes instead of using the 8 dBi static 3GPP model defined for mmWave bands up to 100 GHz. It is also realistic and complete compared to the models proposed by ITU-R [171] and DuFort [172] for which the gain reduction for a certain scan range is tolerated.

For future work, we will extend the proposed MBA approach to the integration of the the increase in the sidelobe level which is considerable for high scan angles. In the same

way, as the model only focuses on the antenna aperture dimensions, the impact of the number of the unit-cells (also called transmitters) and the spacing distance on the system performance (gain, beamwidth, sidelobe level,...) could also be the subject of a next study. This can theoretically highlight the fact that TA (or eventually RA) MBAs could be used to reap the performance gains of massive MIMO especially in mmWave frequency bands, with a reduction of cost and complexity [183].

Although MBAs are low in complexity, designing such a system for the generation of multiple directional and high gain beams that overlap to cover a large sector may require a large antenna space. In this context, the system complexity can be evaluated especially on the UE side.

General Conclusion and Perspectives

Conclusions

Mobile communication systems have recently undergone a significant evolution including several uses and applications with performance requirements. With this in mind, regarding 5G, the requirements are mainly based on high data rates for eMBB applications (virtual reality, UHD video, ...), high network capacity to support a large number of connected devices and low latency for ultra-responsive connections (autonomous cars, remote surgery, etc.). To meet these various requirements, multiple technologies have been proposed in the context of 5G, in particular the use of mmWave frequency bands due to the availability of huge amount of unused bandwidth. To overcome the high attenuation of signal in these frequency bands, the trend is to use directional antennas with narrow beams. However, due to the high sensitivity to obstacles, making the communication directional can lead to limitations such as the blocking phenomenon of the radio link due to the presence of human or vehicle between the Tx and Rx.

In this thesis work, we focused on the improvement of the transmission of 5G services in mmWave frequency bands in the context of blocking phenomenon. Blockage is included in the propagation channels at mmWave frequencies and is characterized by the attenuation of signal strength. Two types of blocking phenomena have been identified: the self-blocking caused by the user itself, and the non-self blocking which is characterized by the presence of obstacles the Tx and Rx. This thesis mainly deals with the impact of non-self-blocking phenomenon on 5G communication performance. Furthermore, since multibeam antenna (MBA) systems represent one of the promising and flexible solutions to cope with this limitation, we also proposed a generic and theoretical approach for modelling such an antenna system that can be integrated in simulation tools.

Impact of Human Blockage on 5G Communication Performance

The impact of blockage has been analyzed in terms of block error rate (BLER) versus SNR in the 26 GHz frequency band. To this end, the contributions of the thesis are:

- In-depth study and analysis of 5G physical layer processing blocks (see Chapter 2);
- State-of-the-art of multipath channel models in mmWave frequency bands (see Chapter 3);
- In-depth study of blocking phenomenon and its modelling in communication systems (see Chapter 4);

- Implementation and validation of the 5G physical layer communication chain in the Galacsy C++ simulator (see Chapter 5);
- Integration of the 3GPP statistical blocking model in the communication chain;
- Evaluations of communication performance using a single blocker.

To illustrate the effect of blockage, we compared communication performance in both scenario with blockage and scenario without blockage. For the parameters used in the simulation, results revealed that for the same 5G eMBB quality of service, the 26 GHz communication system with the presence of human in the LOS cluster requires a 13 dB increase in SNR compared to the similar scenario without blockage. From the performance of BLER=10% and using the 3GPP pathloss model in the link budget, we conclude that the blocking phenomenon can drastically reduce the communication range, in particular by 83% in the study conducted in Chapter 5.

Multibeam Antenna Modelling and Blockage Impact Mitigation

The second part the thesis work was related to the proposal of MBA system modelling (see Chapter 6). The motivations of this second aspect of the PhD thesis are summarized as follows.

- The antenna model proposed by 3GPP [66] for channel modelling is static, i.e the direction of radiation pattern is fixed in both azimuth and elevation planes. In this case, changing the direction in order to avoid the blocker direction becomes infeasible. Although the use of antenna array for the beam steering can be applied, the beam training process with a certain delay is required when the first beam is blocked. This means that the communication link should be restarted after it is interrupted.
- The proposed antenna model of ITU-R [171] is also limited in that it can only be steered in the elevation plane for an angular range of 15° out off the broadside direction. In addition, the scan loss according to the direction of radiation pattern is not taken into account.

In fact, MBA systems have already been introduced for the satellite communication. The first main objective of this work was to propose a generic model of the radiation pattern of such an antenna system. And the second main objective is the application of the proposed model in order to highlight the mitigation of sudden human blocking phenomenon. To this purpose, the following steps have been performed.

- Mathematical proposal of the antenna gain radiation pattern.
- Validation of the proposed antenna model in terms of scan loss and beamwidth degradation depending on the beam direction, using the existing MBAs.
- Integration of the model in the 5G communication chain.
- Link-level assessment using the 3GPP model of multipath channel.

The contributions through the proposal of this theoretical and generic MBA model are:

- Performance prediction in the design of a MBA system;

- Analysis of the hardware complexity according to the high or low number of beams to cover a predefined angular sector;
- Proposal of a realistic model with the integration of the scan loss regardless of the tilt angle;
- Flexibility of the model in azimuth and elevation plane compared to the 3GPP static model, i.e the beam direction can be changed up to $\pm 45^{\circ}$ out off the antenna broadside with a scan loss of 3 dB;
- Integration of the model in a simulation tool.

Using the proposed model with the parameters considered in Chapter 6 at 60 GHz, simulation results reveal that when the single beam is attenuated by 16 dB by a blocker, the communication performance can be improved by 13.2 dB using a second beam that points towards a second path. Furthermore, keeping the same SNR values, it can be seen that the blockage induces a loss of about 85% of the throughput, whereas with the MBA this loss can be lower than 23%.

Moreover, this study has been conducted using an NLOS channel which is composed of two main propagation paths which can be exploited to highlight the advantage of MBA in the blockage context. However, when the channel is usually composed of a single main propagation path and the remaining paths have very low gains, in particular regarding mmWave frequency bands, the application of MBA becomes limited. In this scenario, other solutions can be investigated.

Perspectives

Although in this PhD thesis different contributions have been achieved, further studies could complete this topic. In fact, the following aspects could be investigated.

- The proposed theoretical antenna model can be extended to the increase in the sidelobe level which is significant for high scan angles.
- We also deal with the 3GPP non-self-blocking model which has been proposed for omnidirectional antenna. In this case, the use of such a blocking model is limited in the mmWave context where communications are directional. Therefore, an extension of this model to the integration of the antenna radiation pattern could be investigated. In fact, studies conducted by MacCartney *et al.* [109] at 73 GHz could be exploited.
- Investigations of time scales of blockage event can be conducted in order to analyse the impact of blockage duration on the offered 5G eMBB services. Parameters like the blocker speed and the fact it is static must be taken into account.

Bibliography

[1] T. S. Rappaport, S. Sun, R. Mayzus, H. Zhao, Y. Azar, K. Wang, G. N. Wong, J. K. Schulz, M. Samimi, and F. Gutierrez, "Millimeter Wave Mobile Communications for 5G Cellular: It Will Work!" *IEEE Access*, vol. 1, pp. 335–349, May 2013.

[2] A. Ghosh, "5G Experimental System at High mmWave Band (70 GHz)," Toronto, Canada, September 2017.

[3] WORTECS, "Radio Communication Prototype," Tech. Rep., August 2019, H2020-ICT-2016-2, etworking research beyond 5G.

[4] G. Zülküf, U. H. Rizvi, E. Onur, and I. Niemegeers, "Robust 60 GHz Indoor Connectivity: Is It Possible with Reflections?" Taipei, Taiwan, May 2010.

[5] C. A. L. Diakhate, "Propagation channel modeling at centimeter-and-millimeter-wave frequencies in 5g urban micro-cell context," Ph.D. dissertation, Telecom ParisTech, Université Paris–Saclay, March 2019.

[6] Y. M. Tsang and A. S. Y. Poon, "Detecting Human Blockage and Device Movement in mmWave Communication System," Houston, TX, USA, December 2011.

[7] V. Va, H. Vikalo, and R. W. Heath Jr, "Beam Tracking for Mobile Millimeter Wave Communication Systems," Washington, DC, USA, December 2016.

[8] S. Dogan, M. Karabacak, and H. Arslan, "Optimization of Antenna Beamwidth under Blockage Impact in Millimeter-Wave Bands," in *2018 IEEE 29th Annual International Symposium on Personal, Indoor, and Mobile Radio Communications (PIMRC)*, Bologna, Italy, September 2018.

[9] ITU-R, "IMT Vision–Framework and overall objectives of the future development of IMT for 2020 and beyond," Tech. Rep., September 2015, Recommendation ITU-R M.2083-0.

[10] W. Tong and P. Zhu, "5G: A technology vision," March 2014, Huawei.

[11] S. Parkvall, E. Dahlman, A. Furuskar, and M. Frenne, "NR: The New 5G Radio Access Technology," *IEEE Communications Standards Magazine*, vol. 1, no. 4, pp. 24–30, December 2017.

[12] Marie, "KT Demonstrates World's First 5G Performing at 25 Gbps," February 2016, Business Korea. [Online]. Available: http://www.businesskorea.co.kr/news/articleView.html?idxno=13896

[13] A. Zaharov-Reutt, "Telstra and Ericsson conduct FIRST live 5G trial in Australia," September 2016, IT Wire. [Online]. Available: https://itwire.com/telecoms-and-nbn/telstra-and-ericsson-conduct-first-live-5g-trial-in-australia.html

[14] J. G. Andrews, S. Buzzi, W. Choi, S. V. Hanly, A. Lozano, A. C. K. Soong, and J. C. Zhang, "What Will 5G Be?" *IEEE Journal on Selected Areas in Communications*, vol. 32, no. 6, pp. 24–30, June 2014.

[15] Nokia, "Looking ahead to 5G," June 2014, Building a virtual zero latency gigabit experience.

[16] One5G, "Deliverable D1.2including D6.2 Final Report - Outcomes, Exploitation and Dissemination," Tech. Rep., June 2019, E2E-aware Optimizations and advancements for Network Edge of 5G New Radio (ONE5G).

[17] mmMAGIC, "Measurement Results and Final mmMAGIC Channel Models," Tech. Rep., May 2017, H2020-ICT-671650-mmMAGIC/D2.2.

[18] METIS, "METIS Channel Models," Tech. Rep., February 2015, ICT-317669-METIS/D1.4.

[19] MiWEBA, "Channel Modeling and Characterization," Tech. Rep., June 2014, EU ContractNo. FP7-ICT-608637.

[20] X. Gao, O. Edfors, F. Rusek, and F. Tufvesson, "Massive MIMO Performance Evaluation Based on Measured Propagation Data," *IEEE Transsactions on Wireless Communications*, July 2015.

[21] J. Litva and T. Lo Kwork-Yeung, *Digital Beamforming in Wireless Communications*. Artech House Publishers, 1996.

[22] C. G. Tsinos, S. Maleki, S. Chatzinotas, and B. Ottersten, "On the Energy-Efficiency of Hybrid Analog–Digital Transceivers for Single- and Multi-Carrier Large Antenna Array Systems," *IEEE Journal on Selected Areas in Communications*, September 2017.

[23] J. Kim, J. Jeong, and S. Jeon, "Improvement of Noise Performance in Phased-Array Receivers," *ETRI Journal*, vol. 33, no. 2, pp. 176—-183, April 2011.

[24] U. Gustavsson, C. Sanchéz-Perez, T. Eriksson, F. Athley, G. Durisi, P. Landin, K. Hausmair, C. Fager, and L. Svensson, "On the Impact of Hardware Impairments on Massive MIMO," in *2014 IEEE Globecom Workshops (GC Wkshps)*. Austin, TX, USA: IEEE, December 2014.

[25] M. Vu and A. Paulraj, "MIMO Wireless Linear Precoding," *IEEE Signal Processing Magazine*, December 2006.

[26] B. Romanous, N. Bitar, A. Imran, and H. Refai, "Network Densification: Challenges and Opportunities in enabling 5G," *IEEE Communications Magazine*, vol. 52, no. 2, pp. 82—-89, February 2014.

[27] Z. Pi and F. Khan, "An Introduction to Millimeter-Wave Mobile Broadband Systems," *IEEE Communications Magazine*, vol. 49, no. 6, pp. 101—-107, June 2011.

[28] Arcep, "Les Enjeux de la 5G," Tech. Rep., Mars 2017.

[29] J. Walfisch and H. L. Bertoni, "A Theoretical Model of UHF Propagation in Urban Environments," *IEEE Transactions on Antennas and Propagation*, vol. 36, no. 12, pp. 1788–1796, December 1988.

[30] N. Benvenuto and M. Zorzi, *Principles of Communications Networks and Systems*. Wiley, 2011.

[31] 3GPP, "Technical Specification Group Radio Access Network; NR; Multiplexing and channel coding," Tech. Rep., September 2018, 3GPP TS 38.212 V15.3.0.

[32] ——, "Technical Specification Group Radio Access Network; NR; Physical channels and modulation," Tech. Rep., September 2018, 3GPP TS 38.211 V15.3.0.

[33] Y. Bouguen, E. Hardouin, and F.-X. Wolff, *LTE et les réseaux 4G*. EYROLLES, October 2012.

[34] T. Schmidt, "CRC Generating and Checking," Tech. Rep., 2000, Microchip Technology Inc. [Online]. Available: https://ww1.microchip.com/downloads/en/AppNotes/00730a.pdf

[35] M. Baldi and F. Chiaraluce, "On the Design of Punctured Low Density Parity Check Codes for Variable Rate Systems," *Journal of Communications Software and Systems*, vol. 1, no. 3, pp. 88–100, December 2005.

[36] D. Oh and K. K. Parhi, "Min-Sum Decoder Architectures With Reduced Word Length for LDPC Codes," *IEEE Transactions on Circuits and Systems I: Regular Papers*, vol. 57, no. 1, pp. 105–115, February 2009.

[37] T. T. B. Nguyen, T. N. Tan, and H. Lee, "Efficient QC-LDPC Encoder for 5G New Radio," *Multidisciplinary Digital Publishing Institute (MDPI)*, June 2019.

[38] H. Li, B. Bai, X. Mu, J. Zhang, and H. Xu, "Algebra-Assisted Construction of Quasi-Cyclic LDPC Codes for 5G New Radio," *IEEE Access*, vol. 6, pp. 50 229–50 244, September 2018.

[39] X. Wu, M. Jiang, and C. Zhao, "Decoding Optimization for 5G LDPC Codes by Machine Learning," *IEEE Access*, vol. 6, pp. 2169–3536, September 2018.

[40] D. Hui, S. Sandberg, Y. Blankenship, M. Andersson, and L. Grosjean, "Channel Coding in 5G New Radio: A Tutorial Overview and Performance Comparison with 4G LTE," *IEEE Vehicular Technology Magazine*, vol. 13, no. 4, pp. 60–69, December 2018.

[41] T. Richardson and S. Kudekar, "Design of Low-Density Parity Check Codes for 5G New Radio," *IEEE Communications Magazine*, vol. 56, no. 3, pp. 28–34, March 2018.

[42] R. Jose and A. Pe, "Analysis of hard decision and soft decision decoding algorithms of LDPC codes in AWGN," in *2015 IEEE International Advance Computing Conference (IACC)*. Banglore, India: IEEE, June 2015.

[43] M. R. Islam, D. S. Shafiullah, M. M. A. Faisal, and I. Rahman, "Optimized Min-Sum Decoding Algorithm for Low Density Parity Check Codes," *International Journal of Advanced Computer Science and Applications (IJACSA)*, vol. 2, no. 12, 2011.

[44] J. Zhao, F. Zarkeshvari, and A. H. Banihashemi, "On implementation of min-sum algorithm and its modifications for decoding low-density Parity-check (LDPC) codes," *IEEE Transactions on Communications*, vol. 53, no. 4, pp. 549–554, April 2005.

[45] A. Shokrollahi, *LDPC Codes: An Introduction*, Digital Fountain, Inc., April 2003.

[46] J.-B. Doré, "Optimisation conjointe de codes LDPC et de leurs architectures de décodage et mise en oeuvre sur FPGA," Ph.D. dissertation, INSA de Rennes, October 2017.

[47] A. J. Viterbi, "An Intuitive Justification and a Simplified Implementation of the MAP Decoder for Convolutional Codes," *IEEE Journal on Selected Areas in Communications*, vol. 16, no. 2, pp. 260–264, February 1998.

[48] A. Ayyar, M. Lentmaier, K. Giridhar, and G. Fettweis, "Robust Initial LLRs for Iterative Decoders in Presence of Non-Gaussian Noise," in *2009 IEEE International Symposium on Information Theory*. Seoul, South Korea: IEEE, August 2009.

[49] G. Cisek and T. P. Zieliński, "Prototyping Software Transceiver for the 5G New Radio Physical Uplink Shared Channel," in *2019 Signal Processing Symposium (SPSympo)*. Krakow, Poland: IEEE, September 2019.

[50] J. Chen and M. P. C. Fossorier, "Near optimum universal belief propagation based decoding of low-density parity check codes," *IEEE Transactions on Communications*, vol. 50, no. 3, pp. 406–414, March 2002.

[51] ——, "Density Evolution for Two Improved BP-Based Decoding Algorithms of LDPC Codes," *IEEE Communications Letters*, vol. 6, no. 5, pp. 208–210, May 2002.

[52] Adjudeanu,Irina, *Codes correcteurs d'erreurs LDPC structurés*, FACULTE DES SCIENCES ET DE GENIE UNIVERSITÉ LAVAL QUÉBEC, 2010.

[53] Wagner,Sebastian, *NR LDPC Decoder*, TCL, October 2019.

[54] 3GPP, "Technical Specification Group Radio Access Network; NR; Physical layer procedures for data," Tech. Rep., June 2019, 3GPP TS 38.214 V15.6.0.

[55] Hamidi-Sepehr,Fatemeh and Nimbalker,Ajit, "Analysis of 5G LDPC Codes Rate-Matching Design," in *2018 IEEE 87th Vehicular Technology Conference (VTC Spring)*. Porto, Portugal: IEEE, June 2018.

[56] J. H. Bae, A. Abotabl, H.-P. Lin, K.-B. Song, and J. Lee, "An overview of channel coding for 5G NR cellular communications," *APSIPA Transactions on Signal and Information Processing*, vol. 8, June 2019.

[57] P. Malhotra and G. Saini, "Optimizing Channel Estimation for SCFDMA," *International Journal of Advance research , Ideas and Innovations in Technology (IJARIIT)*, vol. 2, no. 6, pp. 1–5, November 2016.

[58] V. Savaux, "Contribution à l'estimation de canal multi-trajets dans un contexte de modulation OFDM," Ph.D. dissertation, Supelec, 2013.

[59] A. T. HO, "Application des techniques multiporteuses de type OFDM pour les futurs systèmes de télécommunications par satellite," Ph.D. dissertation, Université de Toulouse, March 2009.

[60] 3GPP, "Technical Specification Group Radio Access Network; NR; Base Station (BS) radio transmission and reception," Tech. Rep., September 2018, 3GPP TS 38.104 V15.3.0.

[61] P. W. Wolniansky, G. J. Foschini, G. D. Golden, and R. Valenzuela, "V-BLAST: An architecture for Realizing Very High Data Rates over the Rich-Scattering Wireless Channel," in *1998 URSI International Symposium on Signals, Systems, and Electronics. Conference Proceedings (Cat. No.98EX167)*. Pisa, Italy: IEEE, Octobre 1998.

[62] Z. Nadir, N. Elfadhil, and F. Touati, "Pathloss Determination Using Okumura-Hata Model And Spline Interpolation For Missing Data For Oman," in *Proceedings of the World Congress on Engineering 2008 Vol I*, London, U.K, July 2008.

[63] Y. Singh, "Comparison of Okumura, Hata and COST-231 Models on the Basis of Path Loss and Signal Strength," *International Journal of Computer Applications*, vol. 59, no. 11, pp. 0975–8887, December 2012.

[64] E. Damosso and L. M. Correia, *Digital Mobile Radio Towards Future Generation Systems: Final Report*. Abebooks, 1999, COST Action 231 (Project), European Commission,DGXIII, "Telecommunications, Information Market, and Exploitation of Research".

[65] K. Haneda, J. Zhang, L. Tian, G. Liu, Y. Zheng, H. Asplund, J. Li, Y. Wang, D. Steer, C. Li, T. Balercia, S. Lee, Y. Kim, A. Ghosh, T. Thomas, T. Nakamura, Y. Kakishima, T. Imai, H. Papadopoulas, T. S. Rappaport, G. R. J. MacCartney, M. K. Samimi, S. Sun, O. Koymen, S. Hur, J. Park, C. Zhang, E. Mellios, A. F. Molisch, S. S. Ghassemzadeh, , and A. Ghosh, "5G 3GPP-Like Channel Models for Outdoor Urban Microcellular and Macrocellular Environments," in *2016 IEEE 83rd Vehicular Technology Conference (VTC Spring)*, Nanjing, China, May 2016.

[66] 3GPP, "Technical Specification Group Radio Access Network; Study on channel model for frequencies from 0.5 to 100 GHz," Tech. Rep., June 2018, 3GPP TR 38.901 V15.0.0.

[67] A. Karttunen, J. Järveläinen, S. L. H. Nguyen, and K. Haneda, "Modeling the Multipath Cross-Polarization Ratio for Above-6 GHz Radio Links," *IEEE Communications Magazine (Submitted)*. [Online]. Available: https://arxiv.org/abs/1804.00847

[68] S. Sun, G. R. MacCartney, and T. S. Rappaport, "Millimeter-Wave Distance-Dependent Large-Scale Propagation Measurements and Path Loss Models for Outdoor and Indoor 5G Systems," in *2016 10th European Conference on Antennas and Propagation (EuCAP)*, Davos, Switzerland, April 2016.

[69] A. F. Molisch, H. Asplund, R. Heddergott, M. Steinbauer, and T. Zwick, "The COST259 Directional Channel Model–Part I:Overview and Methodology," *IEEE Transactions on Wireless Communications*, vol. 5, no. 12, pp. 3421–3433, December 2006.

[70] J. A. Gubner, B. N. Bhaskar, and J. Hao, "Multipath-cluster channel models," in *2012 IEEE International Conference on Ultra-Wideband*, Syracuse, NY, USA, September 2012.

[71] A. A. M. Saleh and R. A. Valenzuela, "A Statistical Model for Indoor Multipath Propagation," *IEEE Journal on Selected Areas in Communications*, vol. SAC-5, no. 2, pp. 128–137, February 1987.

[72] P. Patrice, "Towards Reconfigurable and Cognitive Radiocommunications," Tech. Rep., Mars 2006, Comité National Fraçais de Radioélectricité Scientifique-Union Radio Scientique Internaationale.

[73] Q. Spencer, M. Rice, B. Jeffs, and M. Jensen, "Indoor wideband time/angle of arrival multipath propagation results," in *1997 IEEE 47th Vehicular Technology Conference Technology in Motion*, Phoenix, AZ, USA, May 1997.

[74] ITU-R, "Guidelines for evaluation of radio transmission technologies for IMT-2000," Tech. Rep., 1997, ITU-R M.1225.

[75] R. M. Buehrer, S. Arunaclialam, K. H. Wu, and A. Tonello, "Spatial Channel Model and Measurements for IMT-2000 Systems," in *IEEE VTS 53rd Vehicular Technology Conference, Spring 2001. Proceedings (Cat. No.01CH37202)*, Rhodes, Greece, May 2001.

[76] J. Kim and W. Chung, "A spatio-temporal channel model for position location techniques via AOA and TDOA," in *IEEE VTS 53rd Vehicular Technology Conference, Spring 2001. Proceedings (Cat. No.01CH37202)*, Rhodes, Greece, May 2001.

[77] K. I. Pedersen, P. E. Mogensen, and B. H. Fleury, "Spatial Channel Characteristics in Outdoor Environments and their Impact on BS Antenna System Performance," in *VTC'98. 48th IEEE Vehicular Technology Conference. Pathway to Global Wireless Revolution (Cat. No.98CH36151)*, Ottawa, ON, Canada, May 1998.

[78] 3GPP, "Technical Specification Group Radio Access Network;Spatial channel model for Multiple Input Multiple Output (MIMO) simulations," Tech. Rep., September 2012, 3GPP TR 25.996 V16.0.0.

[79] D. S. Baum, J. Hansen, J. Salo, G. D. Galdo, M. Milojevic, and P. Kyösti, "An interim channel model for beyond-3G systems: extending the 3GPP spatial channel model (SCM)," in *2005 IEEE 61st Vehicular Technology Conference*, Stockholm, Sweden, June 2005.

[80] WINNER, "Final Report on Link Level and System Level Channel Models," Tech. Rep., November 2005, IST-2003-507581 WINNER D5.4 v. 1.4.

[81] ——, "WINNER II Channel Models," Tech. Rep., September 2007, IST-4-027756 WINNER II D1.1.2 V1.0.

[82] ——, "WINNER+ Final Channel Models," Tech. Rep., June 2010, CELTIC/CP5-026 D53.doc.

[83] H. Asplund, A. A. Glazunov, A. F. Molisch, K. I. Pedersen, and M. Steinbauer, "The COST 259 Directional Channel Model–Part II: Macrocells," *IEEE Transactions on Wireless Communications*, vol. 5, no. 12, pp. 3434–3450, December 2006.

[84] N. Czink and C. Oestges, "The COST 273 MIMO Channel Model: Three Kinds of Clusters," in *2008 IEEE 10th International Symposium on Spread Spectrum Techniques and Applications*, Bologna, Italy, August 2008.

[85] L. Liu, F. Quitin, K. Haneda, F. Tufvesson, P. De Doncker, and C. Vainikainen, Pertti Oestges, "The COST 2100 MIMO channel model," Tech. Rep., 2012.

[86] M. Zhu, "Geometry-based radio channel characterization and modeling: Parameterization, implementation andvalidation," Ph.D. dissertation, Lund University, August 2014.

[87] L. Liu, C. Oestges, J. Poutanen, K. Haneda, P. Vainikainen, F. Quitin, F. Tufvesson, and P. De Doncker, "The COST 2100 MIMO channel model," *IEEE Wireless Communications*, vol. 19, no. 6, pp. 92–99, December 2012.

[88] l. O. Martínez, P. Eggers, and E. De Carvalho, "Geometry-based stochastic channel models for 5G: Extending key features for massive MIMO," in *2016 IEEE 27th Annual International Symposium on Personal, Indoor, and Mobile Radio Communications (PIMRC)*, Valencia, Spain, September 2016.

[89] IEEE, "Channel Models for 60 GHz WLAN Systems," Tech. Rep., May 2010, IEEE P802.11 Wireless LANs.

[90] S. Jaeckel, L. Raschkowski, K. Börner, and L. Thiele, "QuaDRiGa: A 3-D Multi-Cell Channel Model With Time Evolution for Enabling Virtual Field Trials," *IEEE Transactions on Antennas and Propagation*, vol. 62, no. 6, pp. 3242–3256, June 2014.

[91] T. S. Rappaport, G. R. MacCartney, M. K. Samimi, and S. Sun, "Wideband Millimeter-Wave Propagation Measurements and Channel Models for Future Wireless Communication System Design," *IEEE Transactions on Communications*, vol. 63, no. 9, pp. 3029–3056, September 2015.

[92] 3GPP, "Technical Specification Group Radio Access Network;Study on 3D channel model for LTE (Release 12)," Tech. Rep., June 2015, 3GPP TR 36.873 V12.2.0.

[93] J.-M. Conrat and P. Pajusco, "A Versatile Propagation Channel Simulator for MIMO Link Level Simulation," *EURASIP Journal on Wireless Communications and Networking*, 2007.

[94] W. Keusgen, R. J. Weiler, M. Peter, M. Wisotzki, and B. Göktepe, "Propagation Measurements and Simulations for Millimeter-Wave Mobile Access in a Busy Urban Environment," in *2014 39th International Conference on Infrared, Millimeter, and Terahertz waves (IRMMW-THz)*, Tucson, AZ, USA, September 2014.

[95] Z. Qingling, "Rain Attenuation in Millimeter Wave Ranges," in *2006 7th International Symposium on Antennas, Propagation and EM Theory*, Guilin, China, April 2007.

[96] T. Ismail, E. Leitgeb, and T. Plank, "Free Space Optic and mmWave Communications: Technologies, Challenges and Applications," *IEICE TRANSACTIONS on Communications*, vol. E99-B, no. 6, pp. 1–12, June 2016.

[97] M. A. Weissberger, "An initial critical summary of models for predicting the attenuation of radio waves by trees," Tech. Rep., 1982, DTIC Document.

[98] CCIR, "Influences of terrain irregularities and vegetation on troposphere propagation," Tech. Rep., 1986, CCIR.

[99] A. Nordbotten, "Radiowave propagation effects on next generation fixed services telecommunication systems," Tech. Rep., 1996, TELEKTRONIKK.

[100] M. O. Al-Nuaimi and R. Stephens, "Measurements and prediction model optimisation for signal attenuation in vegetation media at centimetre wave frequencies," *IEEE Proceedings-Microwaves, Antennas and Propagation*, vol. 145, no. 3, pp. 201–206, 1998.

[101] H. M. Rahim, C. Y. Leow, T. A. Rahman, A. Arsad, and M. A. Malek, "Foliage Attenuation Measurement At Millimeter Wave Frequencies In Tropical Vegetation," in *2017 IEEE 13th Malaysia International Conference on Communications (MICC)*, Johor Bahru, Malaysia, November 2017.

[102] A. I. Sulyman, A. Alwarafy, G. R. MacCartney, T. S. Rappaport, and A. Alsanie, "Directional Radio Propagation Path Loss Models for Millimeter-Wave Wireless Networks in the 28-, 60-, and 73-GHz Bands," *IEEE Transactions on Wireless Communications*, vol. 145, no. 3, pp. 6939–6947, October 2016.

[103] S. Hur, S. Baek, B. Kim, Y. Chang, A. F. Molisch, T. S. Rappaport, K. Haned, and J. Park, "Proposal on Millimeter-Wave Channel Modeling for 5G Cellular System," *IEEE Journal of Selected Topics in Signal Processing*, vol. 10, no. 3, pp. 454–469, April 2016.

[104] M. Jacob, C. Mbianke, and T. Kürner, "Human Body Blockage - Guidelines for TGad MAC development," Tech. Rep., November 2009, IEEE 802.11-09/1169r0.

[105] S. Collonge, G. Zaharia, and G. Zein, "Influence of the human activity on wide-band characteristics of the 60 GHz indoor radio channel," *IEEE Transactions on Wireless Communications*, vol. 3, no. 6, pp. 2396–2406, November 2014.

[106] J. S. Lu, D. Steinbach, P. Cabrol, and P. Pietraski, "Modeling Human Blockers in Millimeter Wave Radio Links," *ZTE Communications*, vol. 10, no. 4, pp. 23–28, December 2012.

[107] D. Parsons, *The Mobile Radio Propagation Channel*. Pentech Press, 1992.

[108] M. Jacob, S. Priebe, T. Kleine-Ostmann, T. Schrader, and T. Kurner, "Diffraction in mm and Sub-mm Wave Indoor Propagation Channels," *IEEE Transactions on Microwave Theory and Techniques*, vol. 60, no. 3, pp. 833–844, March 2012.

[109] G. R. MacCartney, S. Deng, S. Sun, and T. S. Rappaport, "Millimeter-Wave Human Blockage at 73 GHz with a Simple Double Knife-Edge Diffraction Model and Extension for Directional Antennas," in *2016 IEEE 84th Vehicular Technology Conference (VTC-Fall)*. Montreal, QC, Canada: IEEE, September 2016.

[110] J. Kunisch and J. Pamp, "Ultra-wideband double vertical knife-edge model for obstruction of a ray by a person," in *2008 IEEE International Conference on Ultra-Wideband*. Hannover, Germany: IEEE, September 2008.

[111] G. R. MacCartney and T. S. Rappaport, "A Flexible Millimeter-Wave Channel Sounder With Absolute Timing," *IEEE Journal on Selected Areas in Communications*, vol. 35, no. 6, pp. 1402–1418, June 2017.

[112] S. V. Hum, "Diffraction," Radio and Microwave Wireless Systems.

[113] M. Cheffena, "Physical-statistical channel model for signal effect by moving human bodies," *EURASIP Journal on Wireless Communications and Networking 2012*, no. 1, December 2012.

[114] F. P. Fontan, B. Montenegro, F. Lacoste, V. Fabbro, L. Castanet, B. Sanmartin, and P. Valtr, "Modelling of the Land Mobile Satellite Channel using a Virtual City Approach," in *The Second European Conference on Antennas and Propagation, EuCAP 2007*. Edinburgh, UK: IEEE, Frebruary 2008.

[115] J. Medbo and F. Harrysson, "Channel Modeling for the Stationary UE Scenario," in *2013 7th European Conference on Antennas and Propagation (EuCAP)*. Gothenburg, Sweden: IEEE, June 2013.

[116] J. Medbo, J.-E. Berg, and F. Harrysson, "Temporal radio channel variations with stationary terminal," in *IEEE 60th Vehicular Technology Conference, 2004. VTC2004-Fall. 2004)*. Gothenburg, Sweden: IEEE, September 2004.

[117] V. Raghavan, L. Akhoondzadeh-Asl, V. Podshivalov, J. Hulten, M. A. Tassoudji, O. H. Koymen, A. Sampath, and J. Li, "Statistical Blockage Modeling and Robustness of Beamforming in Millimeter-Wave Systems," *IEEE Transactions on Microwave Theory and Techniques*, vol. 67, no. 7, July 2019.

[118] M. Jacob, S. Priebe, A. Maltsev, A. Lomayev, V. Erceg, and T. Kürner, "A ray tracing based stochastic human blockage model for the IEEE 802.11ad 60 GHz channel model," in *Proceedings of the 5th European Conference on Antennas and Propagation (EUCAP)*. Rome, Italy: IEEE, April 2011.

[119] G. L. James, *Geometrical theory of diffraction for electromagnetic diffraction*, 3rd ed., London: The Institution of Engineering and Technology, 1979.

[120] W. Qi, J. Huang, J. Sun, Y. Tan, C.-X. Wang, and X. Ge, "Measurements and Modeling of Human Blockage Effects for Multiple Millimeter Wave Bands," in *2017 13th International Wireless Communications and Mobile Computing Conference (IWCMC)*, Valencia, Spain, June 2017.

[121] P. Pagani and P. Pajusco, "Characterization and Modeling of Temporal Variations on an Ultrawideband Radio Link," *IEEE Transactions on Antennas and Propagation*, vol. 54, no. 11, pp. 3198–3206, November 2006.

[122] G. R. MacCartney, T. S. Rappaport, and S. Rangan, "Rapid Fading Due to Human Blockage in PedestrianCrowds at 5G Millimeter-Wave Frequencies," in *GLOBECOM 2017-2017 IEEE Global Communications Conference*. Singapore: IEEE, December 2017.

[123] M. Peter, M. Wisotzki, M. Raceala-Motoc, W. Keusgen, R. Felbecker, M. Jacob, S. Priebe, and T. Kürner, "Analyzing Human Body Shadowing at 60 GHz: Systematic Wideband MIMO Measurements and Modeling Approaches," in *2012 6th European Conference on Antennas and Propagation (EUCAP)*. Prague, Czech Republic: IEEE, March 2012.

[124] T. Bai and R. W. J. Heath, "Analysis of self-body blocking effects in millimeter wave cellular networks," in *2014 48th Asilomar Conference on Signals, Systems and Computers*. Pacific Grove, CA, USA: IEEE, November 2014.

[125] S. Rajagopal, S. Abu-Surra, and M. Malmirchegini, "Channel Feasibility for Outdoor Non-Line-of-Sight mmWave Mobile Communication," in *2012 IEEE Vehicular Technology Conference (VTC Fall)*, Quebec City, QC, Canada, September 2012.

[126] V. Raghavan, T. Bai, A. Sampath, O. H. Koymen, and J. Li, "Modeling and Combating Blockage in Millimeter Wave Systems," in *2018 IEEE 19th International Workshop on Signal Processing Advances in Wireless Communications (SPAWC)*. Kalamata, Greece: IEEE, June 2018.

[127] C. Siyi, C. Liqiang, N. Chongning, L. Anxin, and C. Lan, "Investigation and evaluations on new features for NR channel," in *2017 IEEE 5th International Symposium on Electromagnetic Compatibility (EMC-Beijing)*. Beijing, China: IEEE, October 2017.

[128] C. Gustafson and F. Tufvesson, "Characterization of 60 GHz shadowing by human bodies and simple phantoms," in *2012 6th European Conference on Antennas and Propagation (EUCAP)*. Prague, Czech Republic: IEEE, March 2012.

[129] J. Timmermann, C. Imhof, D. Lebherz, and J. Lange, "Application of Knife-Edge Diffraction Theory to Optimize Radio Frequency Compatibility On-board a Satellite," in *The Seventh International Conference on Advances in Satellite and Space Communications*. Barcelona, Spain: SPACOMM, April 2015.

[130] G. R. MacCartney, T. S. Rappaport, S. Deng, and S. Sun, "Millimeter-Wave Human Blockage at 73 GHz and Millimeter-Wave Diffraction at 10, 20 and 26 GHz," NYU WIRELESS WebEx.

[131] M. Jacob, "The 60 GHz Indoor Radio Channel -Overcoming the Challenges of Human Blockage," Ph.D. dissertation, Technical University of Braunschweig, 2014.

[132] Y. Zhu, Z. Zhang, C. Marzi, Zhinus Nelson, U. Madhow, B. Y. Zhao, and H. Zheng, "Demystifying 60GHz outdoor picocells," in *MobiCom'14 Proceedings of the 20th annual international conference on Mobile computing and networking*. Maui, Hawaii, USA: ACM DIGITAL LIBRARY, September 2014.

[133] ITU, "Propagation par Diffraction PAR DIFFRACTION," RECOMMANDATION UIT-R P.526-6.

[134] A. Anglès-Vázquez, E. Carreño, and L. S. Ahumada, "Modeling the Effect of Pedestrian Traffic in 60-GHz Wireless Links," *IEEE Antennas and Propagation Society, year=2017*, vol. 16, March.

[135] M. Park and H. K. Pan, "A Spatial Diversity Technique for IEEE 802.11ad WLAN in 60 GHz Band," *IEEE Communications Letters*, vol. 16, no. 8, August 2012.

[136] Z. Xiao, "Suboptimal Spatial Diversity Scheme for 60 GHz Millimeter-Wave WLAN," *IEEE Communications Letters*, vol. 17, no. 9, September 2013.

[137] X. An, C.-S. Sum, R. V. Prasad, J. Wang, Z. Lan, J. Wang, R. Hekmat, H. Harada, and I. Niemegeers, "Beam Switching Support to Resolve Link-Blockage Problem in 60 GHz WPANs," in *2009 IEEE 20th International Symposium on Personal, Indoor and Mobile Radio Communications*, Tokyo, Japan, September 2009.

[138] B. Gao, Z. Xiao, C. Zhang, L. SuLi, D. Jin, and L. Zeng, "Double-link Beam Tracking Against Human Blockage and Device Mobility for 60-GHz WLAN," in *2014 IEEE Wireless Communications and Networking Conference (WCNC)*, Istanbul, Turkey, April 2012.

[139] X. Zhang, S. Zhou, X. Wang, Z. Niu, X. Lin, D. Zhu, and M. Lei, "Improving Network Throughput in 60 GHz WLAN svia Multi-AP Diversity," in *2012 IEEE International Conference on Communications (ICC)*. Ottawa, ON, Canada: IEEE, June 2012.

[140] I. K. Jain, R. Kumar, and S. Panwar, "Limited by Capacity or Blockage? A Millimeter Wave Blockage Analysis," August 2018.

[141] M. A. Amalorpava Mary Rajee, Samuel, "Machine Intelligence Technique for Blockage Effects in Next-Generation Heterogeneous Networks," *Radioengineering*, vol. 29, no. 3, September 2020.

[142] K. Sato and T. Manabe, "Estimation of Propagation-Path Visibility for Indoor Wireless LAN Systems under Shadowing Condition by Human Bodies," in *VTC '98. 48th IEEE Vehicular Technology Conference. Pathway to Global Wireless Revolution (Cat. No.98CH36151)*, Ottawa, ON, Canada, May 1998.

[143] A. Agarwal, B. S. Kumar, and K. Agarwal, "BER Performance Analysis of Image Transmission Using OFDM Technique in Different Channel Conditions Using Various Modulation Techniques," *Computational Intelligence in Data Mining*, vol. 711, pp. 1–8, July 2018.

[144] X. Zhao, E. Lukashova, F. Kaltenberger, and S. Wagner, "Practical Hybrid Beamforming Schemes in Massive MIMO 5G NR Systems," in *WSA 2019; 23rd International ITG Workshop on Smart Antennas*. Vienna, Austria: VDE, April 2019.

[145] G. Barb and M. Otesteanu, "On the Influence of Delay Spread in TDL and CDL Channel Models for Downlink 5G MIMO Systems," in *2019 IEEE 10th Annual Ubiquitous Computing, Electronics & Mobile Communication Conference (UEMCON)*. New York, NY, USA: IEEE, October 2019.

[146] E. Chu, J. Yoon, and B. C. Jung, "A Novel Link-to-System Mapping Technique Based on Machine Learning for 5G/IoT Wireless Networks," *Sensors, Scalable and Efficient Networking and Communication Architectures in IoT Domain*, March 2019.

[147] X. Zhao, Q. Wang, S. Li, S. Geng, M. Wang, S. Sun, and Z. Wen, "Attenuation by Human Bodies at 26- and 39.5-GHz Millimeter Wavebands," *IEEE Antennas and Wireless Propagation Letters*, vol. 16, pp. 1229–1232, November 2016.

[148] A. Durrenbach, B. Fourestié, M. Rault, and S. Renou, "Global Shadowing Margins for 3G Networks," in *The 57th IEEE Semiannual Vehicular Technology Conference, 2003. VTC 2003-Spring.* Jeju, Korea (South): IEEE, April 2003.

[149] Y. Yu, P. G. M. Baltus, and A. H. M. van Roermund, "Phased Arrays and Architecture Selection," *Springer, Analog Circuits and Signal Processing*, vol. 1.

[150] W. Hong, Z. H. Jiang, C. Yu, J. Zhou, P. Chen, Z. Yu, H. Zhang, B. Yang, X. Pang, M. Jiang, Y. Cheng, M. K. T. Al-Nuaimi, Y. Zhang, J. Chen, and S. He, "Multibeam Antenna Technologies for 5G Wireless Communications," *IEEE Transactions on Antennas and Propagation*, vol. 65, no. 12, pp. 6231–6249, December 2017.

[151] I. Uchendu and J. Kelly, "Survey of Beam Steering Techniques Available for Millimeter Wave Applications," *Progress In Electromagnetics Research B*, vol. 68, pp. 35–54, May 2016.

[152] E. B. Lima, S. A. Matos, J. R. Costa, C. A. Fernandes, and N. J. G. Fonseca, "Circular Polarization Wide-Angle Beam Steering at Ka-Band by In-Plane Translation of a Plate Lens Antenna," *IEEE Transactions on Antennas and Propagation*, vol. 63, no. 12, pp. 5443–5455, December 2015.

[153] A. B. Smolders, A. Reniers, U. Johannsen, and M. Herben, "Measurement and calibration challenges of microwave and millimeter-wave phased-arrays," in *2013 International Workshop on Antenna Technology (iWAT)*. Karlsruhe, Germany: IEEE, March 2013.

[154] R. T. Prabu, M. Benisha, V. Bai, and V. Yokesh, "Millimeter wave for 5G mobile communication application," in *2016 2nd International Conference on Advances in Electrical, Electronics, Information, Communication and Bio-Informatics (AEEICB)*. Chennai, India: IEEE, February 2016.

[155] G.-B. Wu, S.-W. Qu, and S. Yang, "Wide-Angle Beam-Scanning Reflectarray With Mechanical Steering," *IEEE Transactions on Antennas and Propagation*, vol. 66, no. 1, pp. 172–181, January 2018.

[156] T. C. Quyen and T. A. Vu, "The Application of a Multibeam Antenna for 4G," in *The 2012 International Conference on Advanced Technologies for Communications*, Ha Noi, Vietnam, October 2012.

[157] L. Di Palma, A. Clemente, L. Dussopt, R. Sauleau, P. Potier, and P. Pouliguen, "Circularly-Polarized Reconfigurable Transmitarray in Ka-Band With Beam Scanning and Polarization Switching Capabilities," *IEEE Transactions on Antennas and Propagation*, vol. 65, no. 2, pp. 529–540, January 2018.

[158] P. V. Amadori and C. Masouros, "Low RF-Complexity Millimeter-Wave Beamspace-MIMO Systems by Beam Selection," *IEEE Transactions on Communications*, vol. 63, no. 6, pp. 2212–2223, June 2015.

[159] G. Liu, H.-j. Wang, J.-s. Jiang, F. Xue, and M. Yi, "A High-Efficiency Transmitarray Antenna Using Double Split Ring Slot Elements," *IEEE Antennas and Wireless Propagation Letters*, vol. 14, pp. 1415–1418, March 2015.

[160] F. Diaby, "Reconfigurable transmitarrays for beamsteering and beamforming at millimeterwaves," Ph.D. dissertation, Communauté Université Grenoble Alpes, December 2018.

[161] E. B. Lima, S. A. Matos, J. R. Costa, C. A. Fernandes, and N. J. G. Fonseca, "Bifocal Design and Aperture Phase Optimizations of Reflectarray Antennas for Wide-Angle Beam Scanning Performance," *IEEE Transactions on Antennas and Propagation*, vol. 63, no. 12, pp. 5443–5455, December 2015.

[162] Matos,Sérgio A. and Lima,Eduardo B. and Costa,Jorge R. and Fernandes,Carlos A. and Fonseca,Nelson J. G., "Design of a 40 dBi Planar Bifocal Lens for Mechanical Beam Steering at Ka-Band," in *2016 10th European Conference on Antennas and Propagation (EuCAP)*. Davos, Switzerland: IEEE, April 2016.

[163] P. Nayeri, F. Yang, and A. Z. Elsherbeni, "Bifocal Design and Aperture Phase Optimizations of Reflectarray Antennas for Wide-Angle Beam Scanning Performance," *IEEE Transactions on Antennas and Propagation*, vol. 61, no. 9, pp. 4588–4597, September 2013.

[164] L. Josefsson and P. Persson, *Conformal Array Antenna Theory and Design.* Wiley, 2006.

[165] J. Blass, "Multidirectional Antenna—A new Approach to Stacked Beams," in *1958 IRE International Convention Record.* New York, NY, USA: IEEE, March 1966.

[166] F. Casini, R. V. Gatti, L. Marcaccioli, and R. Sorrentino, "A Novel Design Method for Blass Matrix Beam-Forming Networks," *IEEE Transactions on Antennas and Propagation*, vol. 50, no. 2, pp. 225–232, February 2002.

[167] K. T. Pham, G. Liu, D. G. Ovejero, and R. Sauleau, "Dual-Band Transmitarray with Low Scan Loss for Satcom Applications," *IEEE Transactions on Antennas and Propagation*, October 2020.

[168] A. A. Awaleh, "Design and Characterization of Flat Lens Antenna using Aperture-Couple Microstrip Patches," Master's thesis, Universiti Tun Hussein Onn Malaysia, December 2015.

[169] S. K. Karki, "Beam-Steerable E-Band Lens Antenna for 5G Backhaul Link," Master's thesis, Aalto University, October 2016.

[170] I. Toyoda and T. Seki, "Antenna Model and Its Application to System Design in the Millimeter-wave Wireless Personal Area Networks Standard," Tech. Rep., 2011, NTT Network Innovation Laboratories, Yokosuka-shi, 239-0847 Japan.

[171] IUT-R, "Guidelines for evaluation of radio interface technologies for IMT-Advanced," Tech. Rep., December 2009, Report ITU-R M.2135-1.

[172] E. C. DuFort, "Optimum networks for simultaneous multiple beam antennas," *IEEE Transactions on Antennas and Propagation*, vol. 40, no. 1, pp. 1–7, January 1992.

[173] C.-T. Tai and C. Pereira, "An approximate formula for calculating the directivity of an antenna," *IEEE Transactions on Antennas and Propagation*, vol. 24, no. 2, pp. 235–236, March 1976.

[174] C. A. Balanis, *Antenna Theory: Analysis and Design.* Wiley, January 2005.

[175] I. F. da Costa, H. R. D. Filgueiras, J. Kelly, S. A. Cerqueira, and P. Xiao, "Mechanical beam steering circular patch antenna," in *12th European Conference on Antennas and Propagation (EuCAP 2018).* London, UK: IEEE, April 2018.

[176] F. Diaby, A. Clemente, L. Dussopt, R. Sauleau, K. Pham, and E. Fourn, "Design of a 3-Facet Linearly-Polarized Transmitarray Antenna at Ka-band," in *2018 IEEE International Symposium on Antennas and Propagation and USNC/URSI National Radio Science Meeting.* Boston, MA, USA: IEEE, July 2018.

[177] L. Eyraud, G. Grange, and H. Ohanessian, *Théorie et Techniques des Antennes.* Librairie Vuibert, PARIS, 1973.

[178] T. Pham, K. Pham, F. Gallée, and R. Sauleau, "A Wide-Angle Beam-Steering Bifocal Transmitarray Antenna for 5G Channel Sounding at V-band," *IEEE Transactions on Antennas and Propagation (submitted).*

[179] M. Jiang, Z. N. Chen, Y. Zhang, W. Hong, and X. Xuan, "Metamaterial-Based Thin Planar Lens Antenna for Spatial Beamforming and Multibeam Massive MIMO," *IEEE Transactions on Antennas and Propagation*, vol. 65, no. 2, pp. 464–472, March 2017.

[180] ——, "Metamaterial-Based Thin Planar Lens Antenna for Spatial Beamforming and Multibeam Massive MIMO," *IEEE Transactions on Antennas and Propagation*, vol. 65, no. 2, pp. 464–472, March 2017.

[181] A. Clemente, L. Dussopt, R. Sauleau, P. Potier, and P. Pouliguen, "Wideband 400-Element Electronically Reconfigurable Transmitarray in X Band," *IEEE Transactions on Antennas and Propagation*, vol. 61, no. 10, pp. 5017–5027, March 2017.

[182] H. Yang, F. Yang, X. Cao, S. Xu, J. Gao, X. Chen, M. Li, and T. Li, "A 1600-Element Dual-Frequency Electronically Reconfigurable Reflectarray at X/Ku-Band," *IEEE Transactions on Antennas and Propagation*, vol. 65, no. 6, pp. 3024–3032, June 2017.

[183] Y. Zeng, R. Zhang, and Z. N. Chen, "Electromagnetic Lens-Focusing Antenna Enabled Massive MIMO: Performance Improvement and Cost Reduction," *IEEE Journal on Selected Areas in Communications*, vol. 32, no. 6, pp. 1194–1206, June 2014.

[184] S. R. Rengarajan, "Scanning and Defocusing Characteristics of Microstrip Reflectarrays," *IEEE Antennas and Wireless Propagation Letters*, vol. 9, pp. 163–166, March 2010.

[185] S. A. Matos, E. B. Lima, J. S. Silva, J. R. Costa, C. A. Fernandes, N. J. G. Fonseca, and J. R. Mosig, "High Gain Dual-Band Beam-Steering Transmit Array for Satcom Terminals at Ka-Band," *IEEE Transactions on Antennas and Propagation*, vol. 65, no. 7, pp. 3528–3539, July 2017.

[186] N. Gagnon, A. Petosa, and D. A. McNamara, "Research and Development on Phase-Shifting Surfaces (PSSs)," *IEEE Antennas and Propagation Magazine*, vol. 55, no. 2, pp. 29–48, April 2013.

[187] A. H. Abdelrahman, P. Nayeri, A. Z. Elsherbeni, and F. Yang, "Bandwidth Improvement Methods of Transmitarray Antennas," *IEEE Transactions on Antennas and Propagation*, vol. 63, no. 7, pp. 2946–2954, July 2015.

DOCTORAT BRETAGNE LOIRE / MATHSTIC

IMT Atlantique
Bretagne-Pays de la Loire
École Mines-Télécom

Titre : **Scénarios d'usages et Evolutions de la 5G dans les Nouvelles Bandes Millimétriques**

Mots clés : *Bandes millimétriques, 5G, blocage, bilan de liaison, antenne multifaisceaux, taux de blocs erronés*

Résumé : La cinquième génération de réseaux de téléphonie mobile, appelée 5G, offre une gamme exceptionnelle de services, soumis à des contraintes de débits, de faible latence et exigeant une grande capacité du réseau pour supporter un nombre important d'objets communicants. Pour faire face à ces différentes contraintes, l'usage des hautes fréquences, également appelées bandes millimétriques constitue une réelle opportunité en raison de la disponibilité d'importantes bandes passantes. Afin d'exploiter le potentiel de ces fréquences et surtout éviter la forte atténuation du signal transmis, la tendance est d'utiliser des antennes directives. Cependant, focaliser toute l'énergie transmise dans une seule direction peut conduire à une rupture brusque du lien de communication, due à la présence d'une personne ou d'un véhicule entre l'émetteur et le récepteur. Dans ce contexte on parle de blocage qui se traduit par la forte atténuation de la puissance du signal. Les travaux de cette thèse ont consisté dans un premier temps à évaluer l'impact du blocage sur les performances du système en termes de taux d'erreurs transmises, grâce au développement d'un outil de simulation de la couche physique 5G. Ensuite, l'effet du blocage est analysé sur la portée de la communication à travers un bilan de liaison. Toutefois, comme les antennes multifaisceaux représentent une solution prometteuse à la gestion du phénomène de blocage, ces techniques sont analysées et simulées grâce à une modélisation théorique et générique du diagramme de rayonnement des antennes Comparé aux modèles d'antennes proposés par les standards dans la modélisation du canal, ce modèle est plus flexible, réaliste et adapté à la communication dans les bandes millimétriques.

Title: **5G Scenarios and Evolutions in the New Millimeter-Wave Bands**

Keywords: *Millimeter-waves, 5G, blockage, link budget, multibeam antenna, block error rate*

Abstract: The 5th generation (5G) of mobile communication systems is intended to offer a wide range of applications subject to various constraints in terms of throughputs, low latency communications and high network capacity to support a large number of connected devices. To face these challenging requirements, the use of millimeter-wave (mmWave) frequency bands has become one of the 5G key technologies due to the availability of huge amount of bandwidth. -In order to overcome the attenuation of electromagnetic waves in these frequency bands, directional antennas with narrow beams are recommended. -However, concentrating all energy towards the main propagation path through directional communication eliminates the diversity offered by the multipath and represents a real risk of a sudden interruption of communication in the event of obstacles (human or vehicle) in the beam pointing direction. This thesis deals with the impact of human blockage on 5G communication systems. The analysis of communication performance in terms of block error rate (BLER) with and without the influence of human blockage is proposed, thanks to the implementation of the 5G physical layer in a simulation tool. Based on BLER performance, a link budget is also established in order to evaluate the impact of blockage on the cell coverage. Furthermore, as multibeam antenna (MBA) systems represent a promising candidate to mitigate the effect of blocking, a generic and theoretical approach is proposed to model such an antenna that can be used for performance prediction. The validation with the existing MBAs in different frequency bands is carried out. The proposed antenna model is flexible, completer and more realistic for mmWave systems than the antenna models suggested in the standards.